May 2021

Short-Term Variability of Atmospheric Tides in Earth's Mesosphere and Lower Thermosphere Region

Komal Kumari
Clemson University, kkumari@g.clemson.edu

SHORT-TERM VARIABILITY OF ATMOSPHERIC TIDES IN EARTH'S MESOSPHERE AND LOWER THERMOSPHERE REGION

A Dissertation
Presented to
the Graduate School of
Clemson University

In Partial Fulfillment
of the Requirements for the Degree
Doctor of Philosophy
Physics

---

by
Komal Kumari
May 2021

Accepted by:
Dr. Jens Oberheide, Committee Chair
Dr. Gerald Lehmacher
Dr. Xian Lu
Dr. Murray Daw

ABSTRACT

In the early 2000's, advances in satellite observations and the development of whole atmosphere models led to a paradigm shift in our understanding of what drives space climate/weather in near-Earth space. In addition to solar and magnetospheric driving influences from above, it was realized that meteorological events (such as changes in convection, tropical cyclones, sudden stratospheric warmings, El Niño*,* to name just a few) are important drivers of space climate/weather due to the generation and upward propagation of atmospheric waves (tides, planetary waves (PW), and gravity waves (GW)) from lower atmospheric sources. Atmospheric tides are key to understanding the global-scale connection between tropospheric/stratospheric weather/climate and space weather/climate in the mesosphere and lower thermosphere (MLT) region and further above in the ionosphere-thermosphere (IT) region, including dynamo processes. Much progress has been made in delineating and understanding the "tidal climate" of the MLT region, i.e., tidal variability on seasonal or longer timescales. Tidal variability on shorter timescales, however, is much less understood, mainly due to the observational constraints imposed by satellite local solar time sampling.

This thesis presents a study of the causes of the "tidal weather" or short-term (day-to-day to intraseasonal, i.e., <90-day) tidal variability from satellite observations in the MLT region in connection to lower atmospheric driving. The tidal baseline data used is based on the "tidal deconvolution" approach performed on 18 years of daily tidal temperature tides observed by the SABER instrument onboard the TIMED satellite. In

addition, SD-WACCMX tidal simulations are used to get further insights into the results obtained from the SABER observations. This allows one to resolve non-linear tidal-PW interactions that cause tidal variability on a <30-day timescale, and variability on a 30-90-day timescale that occurs as a response to the recurring Madden-Julian Oscillation (MJO) in tropical convection. This research mainly focuses on two prominent diurnal (D, ~24 hours period) tides which are the westward-propagating (W) zonal wave number 1 (DW1) and the eastward-propagating (E) nonmigrating diurnal tide zonal wave number 3 (DE3) tides, originating from tropospheric radiative and latent heating distributions.

The results in this thesis contribute toward a better understanding of the physical causes of day-to-day to intraseasonal (<90-day) variability in the DW1 and DE3 tides and shed new light on how various propagation and forcing conditions– such as the stratospheric Quasi-Biennial Oscillation (QBO), El Niño and La Niña, MJO and the solar cycle – impact short-term tidal variability. The thesis first discusses the use of an information-theoretic approach from climate science for the statistical characterization of the <30-day short-term tidal variability and proceeds to the regression analysis of multi-year variations in the Sun-Earth system to delineate causes of such characteristics. A key result is that the teleconnection effects due to the QBO in the tropical stratosphere coupled with the solar cycle through the polar vortex disturbances change the <30-day short-term tidal variability. This was not previously known. In the second segment of the thesis, the analysis focuses on the intraseasonal timescale of the tidal variability, where a statistical analysis of SABER observations and SD-WACCMX simulations reveals how the MLT tides respond to the various locations of active-MJO events over the Indian and Pacific

Oceans. This confirmed previously unverified model predictions of a 10-25% tidal modulation by the MJO as a function of MJO-locations up to the MLT region. The tides largely respond to the MJO in the tropospheric tidal forcing, and the tidal advection and GW drag forcing in the MLT region. Filtering by tropospheric/stratospheric background winds is comparatively less important. These findings have broader implications as tides can also couple variability on PW and MJO timescales from the MLT region to the IT through dynamo processes, which is important for a better understanding and prediction of space weather.

DEDICATION

To my beloved grandmother, for her unconditional love and support.

‘

ACKNOWLEDGMENTS

This thesis could not have been completed without the help of my mentors, family and friends. Firstly, I am deeply grateful to the faculty at the department of Physics for giving me the opportunity to work towards my PhD dissertation and for the financial support for this work through grants from NASA.

I would especially like to express my gratitude to my PhD advisor Dr. Jens Oberheide for leading me to work on the exciting projects and for providing me the necessary data and programming resources required for this thesis. Numerous discussions with my advisor and his critical comments and feedbacks played a vital role in what I could contribute towards space physics and aeronomy research with this dissertation.

I am deeply appreciative of the rest of my committee members Dr. Gerald Lehmacher, Dr. Xian Lu, and Dr. Murray Daw as well as the aeronomy group at Clemson for following the progress of my research over the past 6 years and for helping me to strengthen concepts and refine results shown in this thesis with valuable discussions. Most importantly, without intellectual insights and data resources provided by Dr. Xian Lu and Haonan Wu, the work towards Chapter 4 of this thesis could not have been completed.

This journey could not have been completed without love, sacrifice and support from my family. I am grateful to my parents and sisters for sending me strength, prayers and encouragement from 8500 miles away.

Lastly, this thesis could not have been completed without the support of my many friends. I especially thank P.K. Adithya for many valuable discussions on information-theory which was helpful for Chapter 3 analysis. I want to extend my appreciation to my remote friend Rashmi and Sanchari, my fellow physicist friends Lea, Aman, Quan, Bipin, Meenakshi, Sayani, and friends from other sciences Paritra, Kristin, Monsur, Alex and Kyra for helping me maintain a positive and productive atmosphere which kept me going until the end.

TABLE OF CONTENTS

Page

Table of Content (Continued)

Page

LIST OF TABLES

LIST OF FIGURES

List of Figures (Continued)

Figure Page

List of Figures (Continued)

Figure Page

List of Figures (Continued)

Figure Page

List of Figures (Continued)

List of Figures (Continued)

Figure Page

CHAPTER ONE

INTRODUCTION AND MOTIVATION

1.1 Atmospheric Waves: Physics and Dynamics

The beginning of the Space Age was marked in the 1950s and perhaps 2020 can be considered the start of the Space Force Age. A growing number of countries have made significant investments in space-based missions as we have become increasingly dependent on space-based technology (in near-Earth space) to meet the daily needs of society (NRC, 2013). The satellite environment in near-Earth space depends on the complex space-atmospheric interaction region as the maintenance of satellite orbits and trajectories requires the accurate prediction of neutral atmospheric densities over time and space (Leonard et al., 2012). The accurate modeling of neutral atmospheric density requires an understanding of atmospheric waves and dynamics, which modulate the neutral density over time and space. In addition to the direct solar influence, electrically charged particles (plasma) in the upper atmosphere can also be influenced by atmospheric dynamics driven by waves. Satellite communication links and GPS-based navigation depend on an accurate characterization of charged particle density in the upper atmosphere. For decades, scientists have been working towards accurate weather forecasting (day-to-day changes/variability) in the near-Earth space region, also known as space weather. This is non-trivial, since the entire atmospheric system is under the continuous influence of lower atmospheric processes (meteorological effects) and from above (impacts of the Sun and geomagnetic processes) (Lübken et al., 2010; Liu et al., 2010). The study of meteorological effects on space weather was not possible until early 2000s due to limited amount of data owing to shortcomings of both satellite-borne and ground-based instruments. Before that, the textbook knowledge was that the space weather is only influenced by the Sun and the particles from the magnetosphere. Recent advances in satellite missions and progress in whole atmosphere modeling component have provided enough data to have a detailed look into upper atmospheric dynamics. In the region extending between roughly 60 through 120 km, the coupling of the neutral dynamics of the lower atmosphere to the ionized upper atmosphere plays a critical role. This region is probably the most important one among Earth's atmospheric layers to understand how various atmospheric waves forced from below drive variability in space weather on day-to-day to few years (interannual) timescales. The main interest of this thesis is to address what causes the modulation of day-to-day variability in near-Earth space (i.e. space weather) and how it is connected to the weather activities in the lower atmosphere.

1.1.1 Earth's Atmospheric Layers

Earth's atmospheric layers are separated by changes in the atmosphere's temperature gradient (see Figure 1.1). The temperature profile depends on the heating and cooling of various chemical constituents concentrated at different heights and their role in mainly the radiative balance of the atmosphere. The lowermost layer, the troposphere (from ground to ~15 km), contains most of the atmosphere's mass and it is where tropospheric 'weather' such as clouds and rainfall occurs. Since near the surface higher dense gases absorb more radiation from the Sun, air temperature is higher near the ground. The temperature decreases with increasing height due to air thinning and most water vapor freezes out due to the temperature minimum at the tropopause (~15 km). In the stratosphere, extending from the tropopause up to heights of approximately 50 km, temperature increases with increasing height because solar ultra-violet radiation is absorbed by stratospheric ozone.

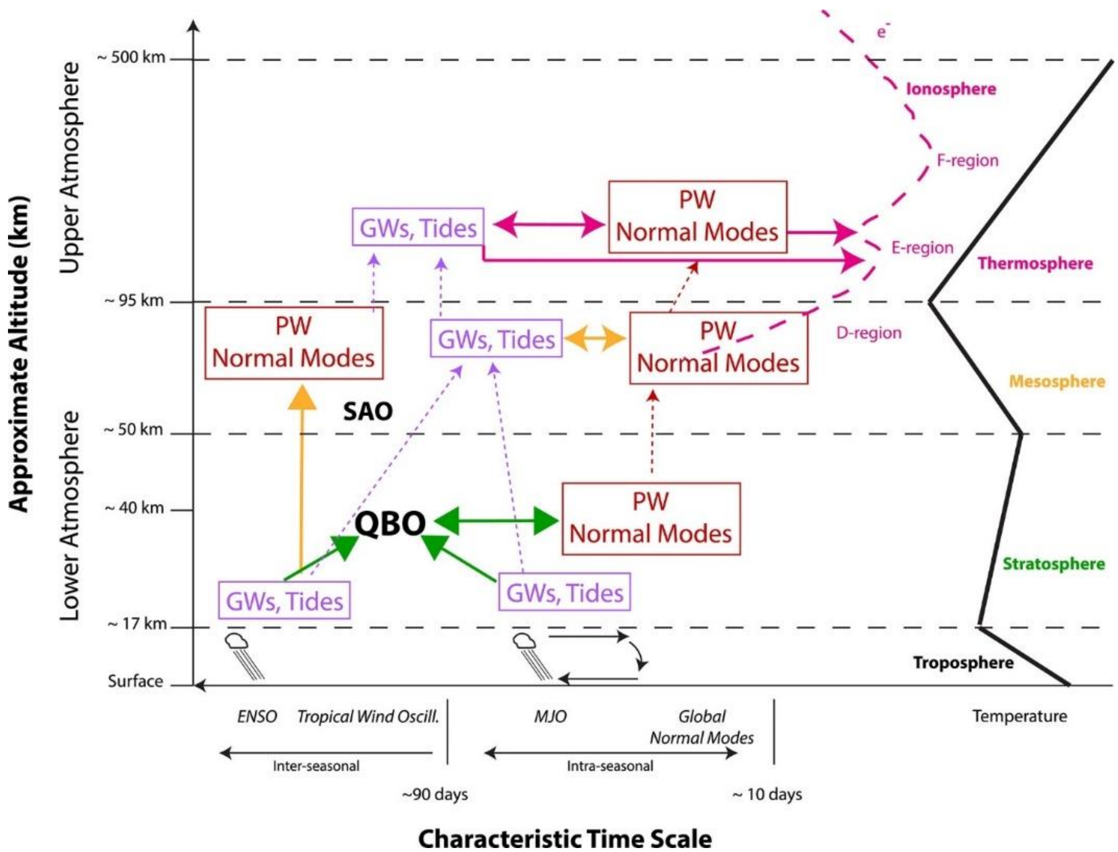

Figure 1.1: The figure illustrates the vertical altitude in terms of different layers, i.e. troposphere to thermosphere, with the corresponding temperature gradient (in the right). One can notice a schematic depiction of the range of time scales (x-axis) with vertical altitudes (y-axis) starting from timescales of global normal modes, intra-seasonal, intra-annual (semiannual or SAO), and interannual (QBO, ENSO). As waves (gravity waves (GWs) and tides) are generated in the lower atmosphere, they are subject to changes on each of these timescales through either wave-wave interaction or change in forcing and/or propagation condition. (Sassi et al., 2019)

Above the stratopause (a local temperature maximum), the rate of change of temperature again changes direction in the mesosphere i.e., decreasing in temperature with increasing height, as at heights of approximately 50-85 km, the CO_2 cooling dominates heating through ozone. Above the mesopause in the thermosphere region, extreme ultraviolet (EUV) solar radiation is absorbed by atomic oxygen and nitrogen leading to a rapid temperature increase with increasing height. The ionization also becomes important in the thermosphere, i.e., the ionosphere. The Earth's mesosphere and lower thermosphere (MLT) region extending between roughly 60 through 120 km altitude (also coinciding with the lowermost ionosphere) is the region of interest for the study in this thesis as its dynamics hosts several atmospheric waves. These waves are key to understanding the connection of tropospheric weather and space weather as they are generally driven by tropospheric weather variations and they subsequently drive space weather variations above the MLT region. The MLT region is also interesting for being more sensitive to climate change than the troposphere (cooling of 10-15 K due to doubling of CO_2) (Akmaev & Fomichev, 1998). A detailed understanding of the mechanisms driven by waves within the MLT region is crucial for understanding the mean state and variability of the ionosphere/thermosphere system as a response to lower atmosphere processes and largely for better interpreting atmospheric observations, understanding the Earth climate system, and developing space weather forecast capabilities.

1.1.2 Atmospheric Waves

Earth's atmosphere possesses a broad spectrum of waves and these atmospheric waves can be distinguished by their spatial and temporal scales. While small-scale gravity waves (GWs) have typical horizontal wavelengths of several km to several hundred km, horizontal scales of solar tidal waves (i.e., atmospheric tides) and planetary waves (PWs) are comparable to the circumference of Earth i.e., in thousands of kms. Although waves can be excited by different mechanisms, in general, meteorological processes in the troposphere (e.g., changes in heating due to tropical rainfall rates, topographical irregularities, land-sea distribution and disturbances such as mountain waves and tsunamis) are the primary sources of these motions (Kato et al., 1982; Tsuda & Kato 1989; Williams & Avery, 1996; Hagan & Forbes, 2002). In addition, there is also a set of waves corresponding to the normal modes (or "free" or resonant modes) of the atmosphere (Madden, 2007; Forbes, 1995). Waves can propagate upward and grow in amplitude due to exponentially decreasing neutral mass density ρ (in order to satisfy wave energy conservation). Thus, although wave disturbances are relatively small at the source levels in the lower atmosphere, their amplitudes can become significant enough at higher altitudes to influence the state of the thermosphere. All waves are subject to various dissipation processes. As the waves dissipate, the momentum and energy from waves/disturbances are transferred to the mean flow which impacts the background or mean state of the atmosphere. Large-scale waves, such as PWs, can possess relatively larger amplitudes in the lower atmosphere, and can therefore dissipate and/or encounter critical levels at lower altitudes (Forbes & Garrett, 1979). However, local-scale GWs and global-scale atmospheric tides can reach up to the MLT region and influence the state of the ionosphere-thermosphere (above MLT region).

1.2 Atmospheric Tides

Global-scale atmospheric tides, originating in the lower atmosphere, are less intermittent than PWs and GWs and are known to influence the state of ionosphere-thermosphere region through neutral-ion coupling (also called dynamo process) (Forbes et al., 2000). Tides have continuous tropo/stratospheric sources as they are mainly caused by the solar heating of the tropospheric water vapor and stratospheric ozone (Forbes, 1995). Tides can also be forced by the latent heat distribution in the tropics due to land-sea contrast. Tides are large enough to propagate up to the MLT region and dominate the MLT dynamics as they have their maximum in the MLT region where their amplitudes are comparable to the background winds. Although the upward-propagating tidal momentum is heavily damped above the MLT region (i.e. >100 km, E region) by various dissipative mechanisms (in particular molecular diffusion), the polarization electric fields the tides produce (by pushing ions in the ionosphere while electrons are attached to magnetic field lines B) can cause detectable modulations of ion density in the upper portion (150-300 km, F region i.e. near-Earth space) of the ionosphere. This is as the feedback between neutral winds and ionized gas may occur via the Lorentz force UxB (Forbes & Lindzen, 1976, 1977; Richmond et al., 1976). Immel et al. (2006) found the ionospheric densities being varied due to atmospheric tides which are mainly driven by tropical convection systems. Due to their significant impacts, tides have been studied extensively in the past few decades, with several observations and models dedicated to investigating their dynamics, climatology and influences. Tidal climatology (≥seasonal) has been extensively studied (Oberheide & Forbes, 2008), while the characteristics on shorter-timescale (<seasonal) in

the middle and upper atmosphere are still among the least known and understood phenomena. One of the main reasons is the lack of proper understanding of the wave-wave coupling of tides with other atmospheric waves due to limitations in observational and model capabilities. Through tidal-GW coupling, tides can have an impact on the critical levels that propagating GWs encounter, producing periodic variations in GW momentum flux deposition (Fritts & Vincent, 1987), while GWs themselves may adjust tidal amplitudes and structures resulting in short-term (~ few hours) tidal variability (Agner & Liu, 2015; Liu et al., 2013; Ortland & Alexander, 2006). PWs can also modulate the tidal amplitudes with PW periodicities (~few days to <30 days) and contribute to the short-term tidal variability (Hagan & Roble, 2001; Mayr et al., 2003; Pancheva & Mitchell, 2004). Moreover, the causes of tidal variations on intraseasonal timescale (i.e., less than a season and more than a month; 30-90-days) is not understood properly. This thesis digs deeper into the physical causes of the short-term tidal variability. The detailed study depends on the spatial and temporal characteristics of tides.

Tides, being mainly forced by daily solar heating, modulate atmospheric field variables (e.g. winds and temperature) with periods that are subharmonics of a solar day. Traditionally, the notations “D” and “S” are utilized to represent the diurnal and semidiurnal tides with periods of 24 and 12 hours respectively, and “W”, “E” and “S” are used to denote the westward-propagating, eastward-propagating, and stationary tides, respectively. The numbers following them correspond to the zonal wavenumbers. Thus, DW1 refers to the diurnal westward propagating tide with zonal wavenumber s=1. By the same token, DW2 and DE3 represent the westward propagating diurnal tide with wavenumber 2 and eastward propagating diurnal tide with wavenumber 3, respectively. Figure 1.2 depicts the tidal structure with respect to longitude, latitude, and local time. The zonal wave number is determined as the number of maxima/minima at a given latitude as a function of longitude (e.g., a clear zonal wave number 4 (wave-4) structure with 4 maxima/minima in Figure 1.2). Studying tides in the local solar time frame (0-24 hrs) has the result of Doppler-shifting the wavenumber of the wave from 3 to 4 (this can also be understood by the result of viewing an eastward propagating wave in a westward propagating Earth's reference frame). This is carefully addressed when tides are analyzed using satellite view (Oberheide et al., 2003).

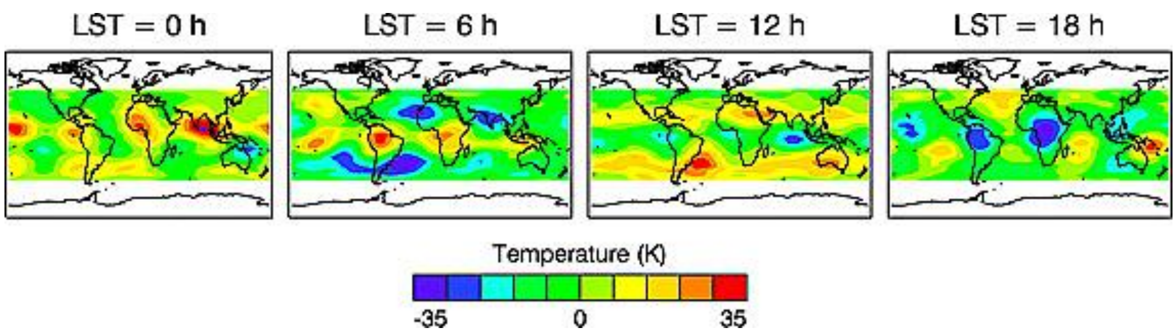

Figure 1.2: The overall tidal structure in temperature observed at 100 km by TIMED satellite (discussed in detail in Chapter 2) as a function of latitude and longitude at 4 local times. (Oberheide et al., 2011)

1.2.1 Classical Tidal Theory

The theoretical study of large-scale waves in a rotating fluid such as waves in an ocean with uniform depth and on an atmospheric sphere of uniform temperature, dates back to the early eighteenth century. These efforts led to the mathematical formulation of the general equation describing such waves/oscillations, which is now known as Laplace's tidal equation (Laplace, 1799). Later, Hough (1898) introduced the functions which describe the horizontal structure of Laplace's tidal equation; while a separation between the vertical and horizontal structures of the three-dimensional Laplace's tidal equation was introduced by Margulis (1893) with the solution of an eigenvalue problem.

The classical tidal theory (Chapman & Lindzen, 1970) involves solving Laplace’s tidal equation which provides a first-order prediction of the tidal perturbation structures in an isothermal, motionless, and inviscid atmosphere. The obtained tidal structures are in terms of modal latitudinal structure (Hough modes) and vertical wavelengths. The derivation of Laplace’s tidal equation primarily involves a set of linearized and simplified primitive equations in spherical coordinates governing the global-scale tidal oscillations (Chapman & Lindzen, 1970). These are conservation equations of momentum (E1.1 and E1.2) and energy (E1.3) along with the continuity equation (E1.4), where log pressure altitude $z = H\ln(P_s/P\ )$ is used as a vertical coordinate with $H = 7.5\ km$ and surface pressure $P_s = 1000\ hPa$. Note that the equations are obtained here for an isothermal atmosphere and with no mean/background wind, and no tidal dissipative effects. The time derivatives of the tidal winds, i.e., meridional (v'; northward motion) and zonal (u'; eastward motion) momentum equations are determined by the Coriolis force $\{2\Omega \sin\varphi\ (u', v')\}$ and pressure gradient force $\left\{\frac{1}{a}\frac{\partial \phi'}{\partial \varphi}, \frac{1}{acos\varphi}\frac{\partial \phi'}{\partial \lambda}\right\}$, which are referred to as classical terms (McLandress, 2002). The time derivative of the vertical geopotential $\phi'(\sim \int g(z,\varphi)dz$ or $\sim T'$; temperature field) gradient is changed by either vertical motion w' or external heating J'(i.e., mechanical or thermal forcing).

$$\frac{\partial u'}{\partial t} - 2\Omega \sin\varphi\, v' + \frac{1}{a cos\varphi}\frac{\partial \phi'}{\partial \lambda} = 0 \qquad [E1.1]$$

$$\frac{\partial v'}{\partial t} + 2\Omega \sin\varphi\, u' + \frac{1}{a}\frac{\partial \phi'}{\partial \varphi} = 0 \qquad [E1.2]$$

$$\frac{\partial^2 \phi'}{\partial t \partial z} + N^2 w' = \frac{\kappa J'}{H} \qquad [E1.3]$$

$$\frac{1}{a cos\varphi}\left(\frac{\partial u'}{\partial \lambda} + \frac{\partial (v' cos\varphi)}{\partial \varphi}\right) + \frac{1}{\varrho_o}\frac{\partial (\varrho_o w')}{\partial z} = 0 \qquad [E1.4]$$

with,

$N^2 = \frac{\kappa g}{H}$, Brunt-Vaisala (buoyancy) frequency,

$\kappa = \frac{R}{c_p} \approx \frac{2}{7}$,

$\varrho_o \propto e^{-z/H}$, density,

Ω angular velocity of the Earth,

z altitude,

λ longitude,

φ latitude,

a radius of the Earth,

g gravitational acceleration,

H constant scale height.

The set of equations E1.1-1.4 can be solved for longitudinally propagating waves of zonal wavenumber s and wave frequency ω with respect to time and longitude:

$$\{u', v', w', \phi'\} = \{\hat{u}, \hat{v}, \hat{w}, \hat{\phi}\}\, e^{i(s\lambda - \omega t)}$$

Here for $s > 0$, eastward propagating waves are represented with $\omega > 0$ while westward propagating waves are denoted by $\omega < 0$. Using equations E1.1, E1.2, and E1.3, $(\hat{u}, \hat{v}, \hat{w})$ are replaced by $\hat{\phi}$, which results in a single second-order partial differential equation in terms of $\hat{\phi}$(z,φ). In an isothermal atmosphere with no background winds, one can solve for $\hat{\phi}$ by the separation of variables method (equation E1.5) which yields two equations (E1.6 and E1.8) each for φ (latitudinal coordinate) and z (vertical coordinate), respectively. Note that the expression of Laplace operator $\mathcal{L}$ in equation E1.7 comes from equation E1.6.

$$\hat{\phi} = \sum_{n} \Theta_m(\varphi) G_m(z) \qquad [E1.5]$$

$$\frac{\partial}{\partial \mu}\left[\frac{(1-\mu^2)}{(f^2-\mu^2)}\frac{\partial \Theta_m}{\partial \mu}\right] - \frac{1}{f^2-\mu^2}\left[-\frac{s}{f}\frac{(f^2+\mu^2)}{(f^2-\mu^2)} + \frac{s^2}{1-\mu^2}\right]\Theta_m + \varepsilon_m \Theta_m = 0 \qquad [E1.6]$$

$$\Longrightarrow \mathcal{L}\Theta_m + \epsilon_m \Theta_m = 0 \qquad [E1.7]$$

$$i\omega H\left[\frac{1}{\varrho_o}\frac{\partial}{\partial z}\varrho_o \frac{\partial}{\partial z} G_m\right] + \frac{1}{\varrho_o}\frac{\partial}{\partial z}(\varrho_o \kappa J_m) = -\frac{i\omega\kappa}{h_m} G_m \qquad [E1.8]$$

where, $f = \frac{\omega}{2\Omega}, \mu = sin\varphi, \epsilon_m = \frac{(2\Omega a)^2}{g h_m}, J' = \hat{J} e^{i(s\lambda - \omega t)}$, and

$$\hat{J} = \sum_{m} \Theta_m(\varphi) J_m(z) \qquad [E1.9]$$

The equation associated with the horizontal structure of the tide (with zonal wave number s) is known as Laplace tidal equation (E1.7) and the solutions are provided by Hough functions $\{s, \Theta_m\}$. Hough functions are complete set of orthogonal eigenfunctions which provide a basis to describe the latitudinal structure of tides. Each tidal component of a certain wavenumber/frequency pair (i.e., $\{s, \omega\}$) can be described as a superposition of associated Hough functions of index m (often called tidal Hough modes). The equation

E1.8 associated with the vertical structure of the tides is connected with the eigenvalues ϵ_m of Hough functions (i.e., latitudinal structure of tides) by equivalent depth h_m. So, each tidal mode has a unique equivalent depth which is related to its vertical structure and a unique latitudinal distribution. For diurnal tides, odd numbers of m in tidal modes $\{\Theta_m\}$ correspond to waves symmetric with respect to the equator, and even numbers corresponding to antisymmetric waves. For semidiurnal tides, odd numbers of m represent the antisymmetric modes and even numbers represent symmetric modes. Several tidal components for a given zonal wave number s exist which (horizontal structures) are represented as unique superposition of different Hough modes or tidal modes (s, m), as can be understood from Figure 1.3. The characteristic of each mode is provided by Forbes (1995). The tidal heating term J' can also be expanded in terms of Hough functions (equation E1.9) as there is no heating source in the MLT region and tides are generated due to the heating in the lower atmosphere. To investigate the response of heating in each tidal Hough mode, tidal heating can be projected on Hough modes. The vertical structure of each mode can be derived after substituting $G_m^* = G_m \varrho_o^{1/2} N^{-1}, x = \frac{z}{H}$, and $H = 7.5\ km$ in equation E1.8 for an isothermal atmosphere. This results in the expression given in equation E1.10, which solves for trapped ($\alpha_m^2 < 0$), propagating ($\alpha_m^2 > 0$) and free modes ($\alpha_m^2 = 0$) of wave oscillations in the vertical direction.

$$\frac{\partial^2 G_m^*}{\partial x^2} + \alpha_m^2 G_m^* = F_m(x) \qquad [E1.10]$$

$$\Longrightarrow\ G_m^*(x) \sim A e^{i\alpha_m x} + B e^{-i\alpha_m x} \qquad [E1.11]$$

where, $\lambda_{z,m} = \frac{2\pi H}{\alpha_m}, \alpha_m = \sqrt{\frac{\kappa H}{h_m} - \frac{1}{4}}, \&\ F_m(x) = -\frac{\varrho_0^{-1/2}}{i\omega N}\frac{\partial(\varrho_0 J_m)}{\partial x}$

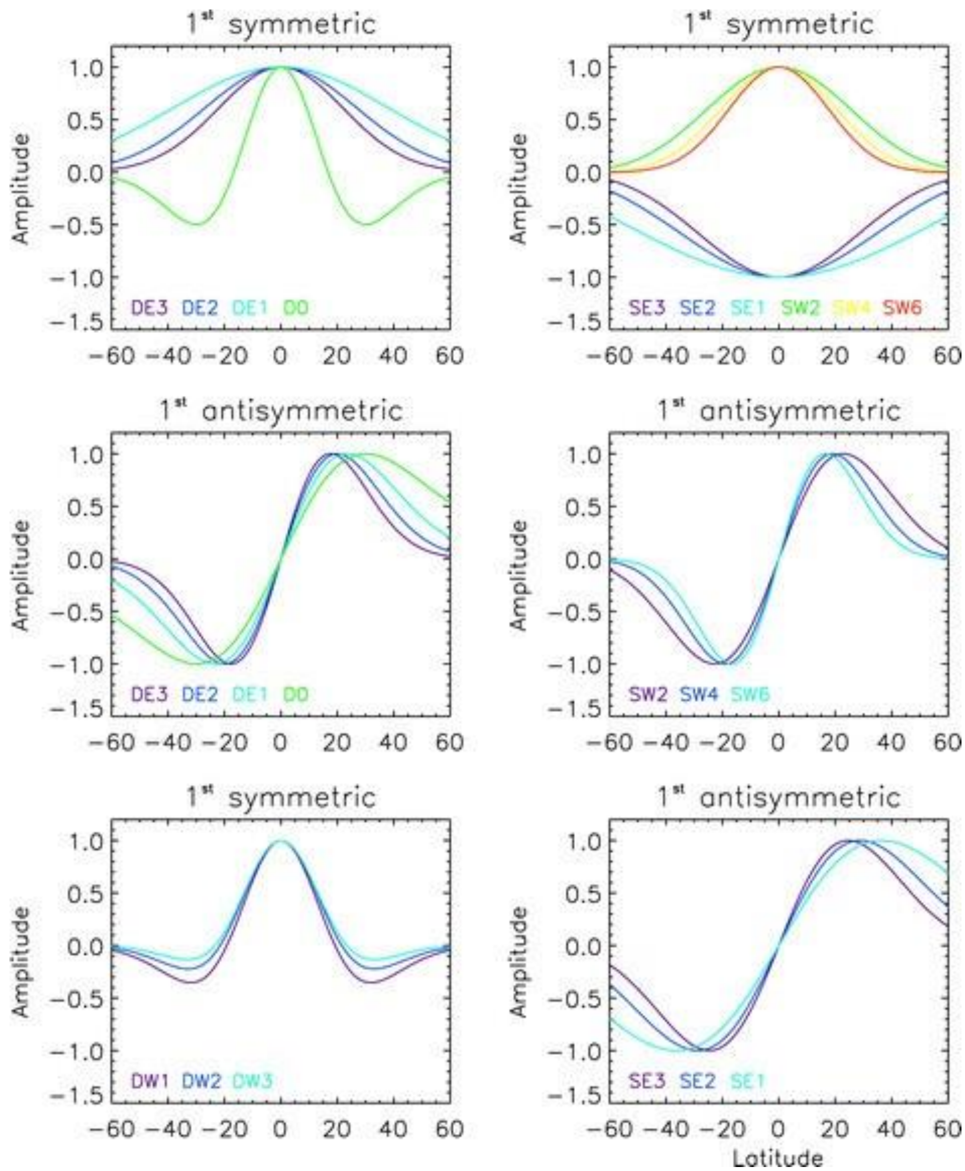

Figure 1.3: The first symmetric and antisymmetric components of both diurnal and semidiurnal eastward/westward/stationary propagating tidal components of various zonal wave numbers. (Trukowski et al., 2014)

The $\hat{u}, \hat{v}$ can be solved for tidal winds in a similar manner using the following expressions:

$$\hat{u} = \frac{\omega}{4\Omega^2 a} \sum_m \mathrm{U}_m(\varphi) G_m(z) \quad [E1.12]$$

$$\hat{v} = \frac{-i\omega}{4\Omega^2 a} \sum_m \mathrm{V}_m(\varphi) G_m(z) \quad [E1.13]$$

$$U_m = \frac{1}{(f^2 - \sin^2 \varphi)} \left[\frac{s}{\cos \varphi} + \frac{\sin \varphi}{f} \frac{\partial}{\partial \varphi} \right] \Theta_m \qquad [E1.14]$$

$$V_m = \frac{1}{(f^2 - \sin^2 \varphi)} \left[\frac{s \tan \varphi}{f} + \frac{\partial}{\partial \varphi} \right] \Theta_m \qquad [E1.15]$$

The wind expansion functions (U_m, V_m) are basically the meridional derivatives of Θ_m. This is why the latitudinal structure of the mode $(s = 1, m = 1)$ is symmetric about the equator in terms of the geopotential, temperature and zonal wind, while antisymmetric for the meridional wind (figure not shown here). Note that the vertical structure functions $G_m(z)$ describe the vertical structure for all three quantities $\hat{u}, \hat{v}, \widehat{\Phi}$ which depends on J'. The vertical structure equation also shows that the amplitude increases exponentially with height, $\sim e^{z/2H}$, as density decreases, and the downward phase progression of tides means upward energy propagation. This can be understood as the vertical group velocity $C_{gz,m} = H \frac{\partial \omega}{\partial \alpha_m}$ can become positive only if α_m and ω have the opposite signs (Forbes, 1995). For a given height and longitude, the tidal wave maximizes for $s\lambda - \omega t + \alpha_m x = 0$, opposite signs of α_m and ω results in downward phase progression $\left(\frac{\partial t}{\partial x} < 0\right)$ associated with the upward transport of wave energy $(\alpha_m^2 > 0)$.

In classical tidal theory, the distribution of heating drives the generation of atmospheric tidal components. Hough modes may be excited when the heating efficiently projects onto its latitudinal structures. Even with realistic distributions of atmospheric heating specified, the agreement of classical tidal theory with atmospheric tidal observations is limited, due to the theoretical assumptions (such as no dissipative or nonlinear effects due to the background atmosphere are included in the Equation E1.1-1.4).

While dissipation is not included in classical tidal theory, modeling and observational studies have concluded that dissipation from radiative cooling, friction, turbulence and diffusion of momentum and heat have an important role in the damping of tidal amplitudes (Lindzen, 1971; Forbes & Hagan, 1979). Subsequently, only a few tides are able to propagate above 100 km and directly penetrate the thermosphere and ionosphere. Furthermore, the inclusion of realistic physical processes such as friction, mean winds and a nonuniform background atmosphere in the linearized perturbation equations (e.g., E1.16 and E1.17, where mean zonal wind $\bar{u}$ is not zero and X and Y are nonconservative mechanical forcings such as gravity wave drag, ion drag, and eddy and molecular diffusion) results in solutions that are not separable in latitude (φ) and altitude (z) and thus cannot be solved analytically. Hence, the latitudinal shape of each classical Hough mode is no longer independent of height (Richmond, 1975). In order to determine tidal solutions for a given forcing profile, the governing equations must be solved using numerical methods. A number of numerical or modelling studies (Lindzen & Hong, 1974; Forbes & Hagan, 1988) have analyzed how mean winds can alter the latitudinal and vertical structure of tides from classical tidal theory. Note that the advection terms (3^{rd} term in right hand side of equations E1.16 and E1.17) and curvature terms (4^{th} term) arises due to the presence of the mean zonal wind. The effects of mean winds have been studied by considering impact of linear and nonlinear advection term by mean winds in the tidal momentum equations (Lu et al., 2012). The dissipation (X, Y) due to the eddy and molecular diffusion in the tidal momentum equations is parametrized by an effective Rayleigh friction coefficient (with complex frequency) while the heat is parametrized as a Newtonian cooling (i.e. rate of loss of heat through radiation) term in the thermal energy equation (Forbes & Vincent, 1989). The complex frequency allows one to approximate the effects of damping or dissipation on the vertical structure of propagating tides. The effect of gravity wave drags (GWD) are parametrized as well in the modelling study.

$$\frac{\partial u'}{\partial t} = 2\Omega \sin\varphi\, v' - \frac{1}{a\cos\varphi}\frac{\partial \Phi'}{\partial \lambda} - \left(\frac{\bar{u}}{a\cos\varphi}\frac{\partial u'}{\partial \lambda} + \frac{v'}{a}\frac{\partial \bar{u}}{\partial \phi}\right) + \frac{\bar{u}v'}{a}\tan\varphi + X \qquad [E1.16]$$

$$\frac{\partial v'}{\partial t} = -2\Omega \sin\varphi\, u' - \frac{1}{a}\frac{\partial \Phi'}{\partial \varphi} - \left(\frac{\bar{u}}{a\cos\varphi}\frac{\partial v'}{\partial \lambda} + \frac{v'}{a}\frac{\partial v'}{\partial \varphi}\right) - \frac{\bar{u}u'}{a}\tan\varphi + Y \qquad [E1.17]$$

Spatial gradients in the background wind or temperature have been observed to significantly enhance or suppress the propagation of waves (Walterscheid, 1980; McLandress, 2002). Additionally, large eastward or westward zonal winds can Doppler-shift tides to smaller or larger frequencies, modifying the inherent propagation and dissipation characteristics of each wave (Forbes & Vincent, 1989). In reality, the presence of mean winds and nonuniform background fields may alter the Hough mode decomposition of tides. There are several perspectives that can be used to describe these effects on the Hough modes. One perspective is the "mode coupling" approach (Forbes & Hagan, 1988). In this context, the tide is still assumed to be decomposed into a series of classical Hough modes and the main effect of zonal mean winds is to couple energy from one classical Hough mode to another. The different superpositions of the Hough modes in different seasons point to a potential mechanism for the seasonal variation of tides (Forbes & Hagan, 1988; Oberheide & Forbes, 2008; Zhang et al., 2012).

Note that the existence of both tides and PWs in the atmosphere has been quantitatively predicted by classical tidal theory (Chapman & Lindzen, 1970). PWs generally encompass all global scale oscillations that have periods greater than a solar day. Like atmospheric tides, PWs can propagate horizontally with varying wavenumber and frequency, as well as vertically, carrying momentum and energy. PWs incorporate a broad range of wave types including Rossby waves and Kelvin waves that arise due to the rotational effects of the Earth's atmosphere. A few of PWs may arise as manifestations of the unforced, resonant modes of the atmosphere e.g. 5-day, 10-day, 16-day and 23-day westward propagating waves (Madden, 2007). Lastly, the nonlinear wave-wave interactions between atmospheric tides, PWs and GWs are not captured through the application of classical theory because nonlinear terms are neglected in the linearized governing equations E1.1-E1.4.

Classical tidal theory is used in practice to decompose the latitudinal observed tidal structures as a superposition of Hough modes in the MLT region, discussed in depth in Chapter 2. The fitting of Hough modes $\{\Theta_{\mathrm{m}}, U_m, V_m\}$ to the observation field for a given zonal wave number yields the complex amplitudes of tidal fields in geopotential (or temperature), zonal and meridional winds. The fitting is performed at each altitude to obtain the vertical structure of each mode. As the seasonal variation in tidal components depends on the superposed Hough modes which can be influenced by the tidal-mean wind interaction, a study with Hough mode decomposition of MLT tides can be used for additional insights, explained in detail in Chapter 2.

1.2.2 Diurnal Tides: Migrating and Nonmigrating

DW1 is the migrating diurnal tide (s=1) which moves synchronously westward with the Sun, i.e., with the same phase speed as the Earth's rotation. Since for DW2 and DE3, s

$\neq 1$, they are nonmigrating tides. They do not follow the westward motion of the Sun. Classical tidal theory predicts that each tidal component is composed of a series of Hough modes and the excitation of a particular Hough mode depends on efficient projection of heating in its latitudinal structure and the altitude structure. Each Hough mode has a particular wavelength. Heating is most efficient if the thickness of the layer is about half a wavelength, to avoid cancellation effects or too inefficient forcing. Migrating tides are mainly excited by the absorption of near-infrared (IR) solar radiation by water vapor in the troposphere and ultraviolet solar radiation by ozone in the stratosphere (Forbes, 1995). Solar heating in the troposphere projects most efficiently on the DW1 (1,1) Hough mode. The characteristics of the DW1 (1,1) Hough mode dominates the latitudinal structure of the DW1 throughout the troposphere, stratosphere and mesosphere. Unlike DW1, another prominent MLT nonmigrating tide is DE3, which is generally described with the help of 2 Hough modes, i.e. the first symmetric and first antisymmetric mode. This is because the nonmigrating tide DE3 is mainly excited by zonal wave number 4 (sometimes called wave-4) structure of latent heat release in the tropical rainfall region (Hagan & Forbes, 2002). Briefly, DE3 and DW5 are the result of an interference between wave-1 diurnal solar heating and the wave-4 latent heating. DW5 dissipates before DE3 due to its shorter vertical wavelength. Historically, ground-based radars have revealed many properties of the diurnal tide, including its vertical structure in amplitude and phase and its seasonal dependence at various locations. Long-term radar observations showed the amplitude to be deeply modulated on timescales ranging from a few days to a seasonal dependence (Vincent et al., 1988; Manson et al., 1991; Fritts & Isler, 1994). An inherent weakness of these studies was the inability to distinguish between the migrating tide and nonmigrating tides. The unambiguous identification of migrating and nonmigrating tides only became possible with the advent of the UARS (Upper Atmosphere Research Satellite), launched in 1991 (Lieberman et al., 1991; Talaat & Lieberman, 1999). This study includes the diurnal migrating DW1 and nonmigrating DE3 tidal extraction from the TIMED (thermosphere ionosphere mesosphere energetics and dynamics) satellite as the migrating DW1 and nonmigrating DE3 are the most prominent tides in the MLT dynamics.

1.2.3 Diurnal Tidal Variability: Long-term and Short-term

Atmospheric tides observed by satellite measurements in the mesosphere and lower thermosphere exhibit substantial long- and short-term variability in amplitude and phase. They are studied on various temporal scales because they introduce a large longitudinal and local time variability in the MLT region (Hagan et al., 1997; Hagan & Forbes, 2002; Khattatov et al., 1996; Miyahara et al., 1999) and the ionosphere (e.g., Immel et al., 2006, 2009; Pedatella et al., 2016). In particular, the DE3 tide propagates further into the thermosphere where it impacts the energy budget of the thermosphere through modulation of the 15 micrometer CO_2 and 5.3 micrometer NO infrared emissions (Nischal et al., 2017, 2019), and mean winds, temperature and constituents (Jones et al., 2014, 2016, 2019). The seasonal variability of the DW1 and DE3, and its impact on the ionosphere and thermosphere, has been extensively studied in both numerical models (Akmaev et al., 2008; Liu et al., 2010; Häusler et al., 2010) and observations (Forbes et al., 2008, 2009; Lühr et al., 2008; Pedatella et al., 2008). Figure 1.4 depicts the observed amplitude variations of

DW1 and DE3 temperatures from January-December during 2009, obtained by the TIMED satellite.

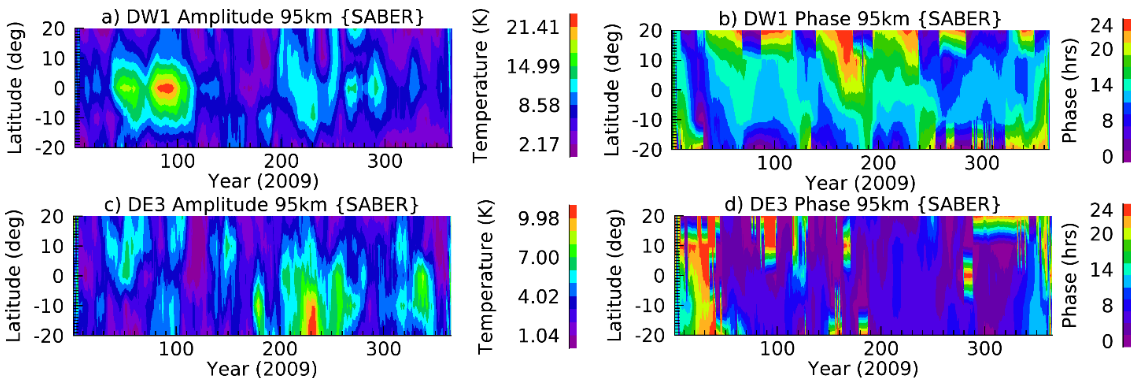

Figure 1.4: 11-day running mean of a) DW1 and c) DE3 tidal amplitudes and corresponding phases in b) and d) at 95 km observed by TIMED satellite during 2009, discussed further in Chapter 2.

The underlying mechanisms associated with the seasonal (summer-winter) variability of the diurnal tide involve the interference of different tidal Hough modes, as discussed in section 1.2.1. The seasonal variation in DW1 is mainly due to changes in tropospheric forcing in the (1,1) mode with additional effects due to mean/background winds. Briefly, DW1 has two maxima during spring and fall equinox conditions when heating is most efficient in the (1,1) mode which is due to equal amount of daylight and darkness at all latitudes. However, mode coupling occurs when the vertical shear in the mean flow becomes significant which is when the reversal of the sign occurs for the summer and winter jets in the upper mesosphere (McLandress, 2002; Ortland, 2005). This results in hemisphere asymmetries or contribution due to other Hough modes in DW1 amplitudes. DE3 is mostly represented by the first symmetric and first antisymmetric modes. Vertically propagating atmospheric tides can also be impacted by propagation conditions such as the Quasi-Biennial Oscillation (QBO) and forcing conditions such as the El Niño–Southern Oscillation (ENSO) and the solar cycle. QBO, ENSO and solar cycle are the dominant modes of interannual variability in the atmosphere (shown in Figure 1.5).

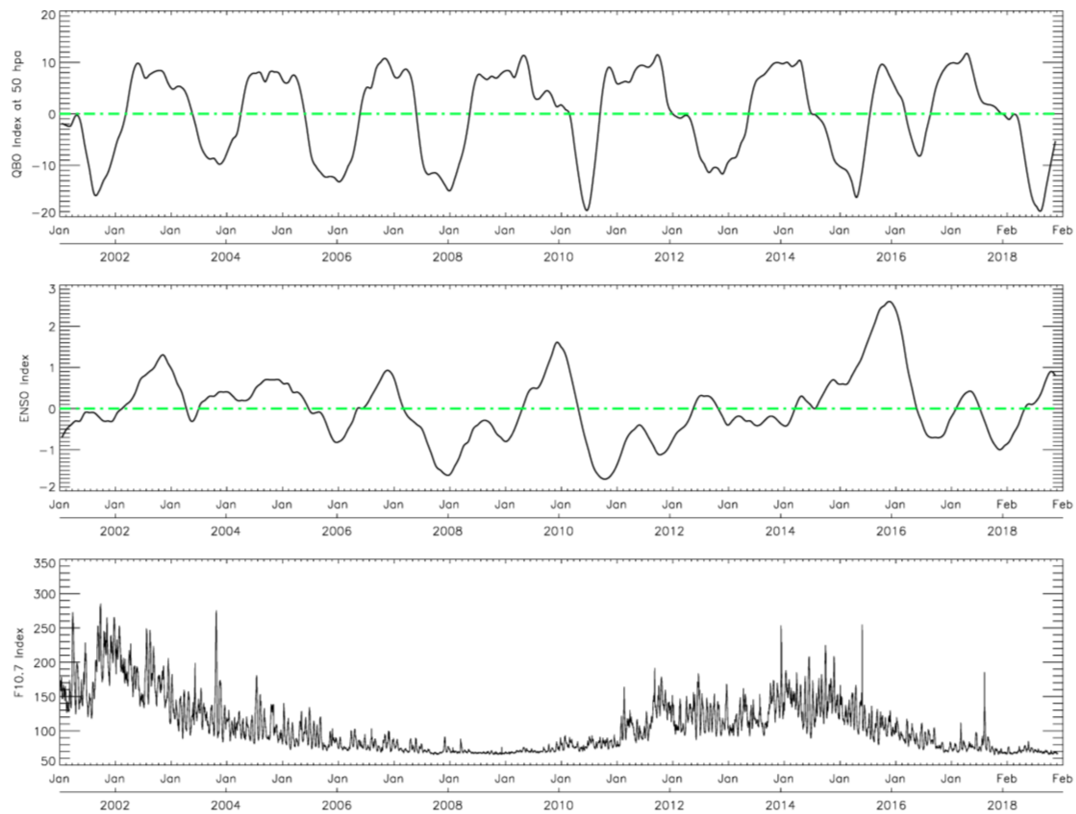

Figure 1.5: The stratospheric QBO index, tropospheric ENSO index and F10.7 index for daily solar flux to the atmosphere. The green line in QBO and ENSO indices represents the zero-line. The positive and negative indices of QBO represent westerly and easterly direction of equatorial winds at the 50 hPa pressure level, respectively. The positive and negative indices in ENSO represent warm and cool phases of the Pacific Ocean sea surface temperature in region 3.4 known as El Niño and La Niña, respectively.

Figure 1.6 shows the interannual variation in DE3 tides as a function of latitude and altitude. A few studies have investigated the role of ENSO in tidal-forcing (Gurubaran et al., 2005; Lieberman et al., 2007; Warner & Oberheide 2014) and the role of the stratospheric QBO in driving interannual tidal variability (Burrage et al., 1995; Hagan et al., 1999; Oberheide et al., 2009; Gurubaran et al., 2009; Mukhtarov et al., 2009).

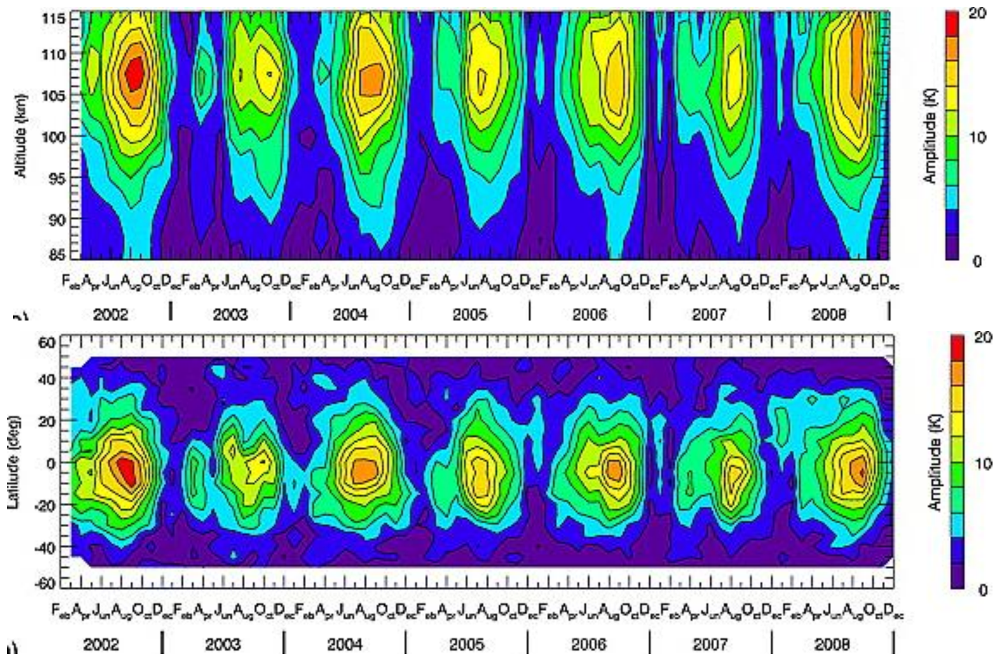

Figure 1.6: (Top) DE3 temperature amplitudes averaged between ±5° latitude range and (bottom) amplitudes at peak altitudes in MLT region ~100 km observed by the TIMED satellite for the years 2002-2008. (Oberheide et al., 2009)

The QBO is the characteristic mean flow behavior of zonal winds in the tropical stratosphere-mesosphere system. Studies have shown that QBO interaction with tides can dampen or enhance the tides as they propagate upwards to the MLT region (e.g., Andrews et al., 1987; Mayr & Mengel, 2005). ENSO is linked to periodic warming (El Niño phase) and cooling (La Niña phase) in western and central Pacific sea-surface temperatures, resulting in changes in large-scale convective systems and hence a large-scale redistribution of water vapor latent heat release and radiative heating. Consequently, ENSO modifies the forcing condition in particular for nonmigrating tides (Gurubaran et al., 2005; Liebermann et al., 2007). Warner & Oberheide (2014) found enhanced DE3 tides during the 2010/11 La Niña phase due to enhanced tidal forcing and a negligible response during the El Niño phase. Solar activity continuously affects space weather from above and plays an important role in determining the state of Earth's atmosphere. One may assume that solar activity is expected to have some influence on tides, however, many existing studies of MLT tides (e.g., Bremer et al., 1997; Fraser et al., 1989, and thereafter) do not show a statistically significant correlation between tidal amplitude and solar activity, likely due to the small solar cycle variations in the Sun’s infrared emissions absorbed in the troposphere.

Apart from variations in the seasonal and interannual tides for such conditions (Nischal et al., 2019; Oberheide et al., 2009; Warner & Oberheide, 2014; Yang et al., 2018), there is significant variability on intraseasonal to day-to-day timescales in satellite observations (Lieberman et al., 2004; Liu et al., 2007). Though progress have been made in predicting some aspects of tidal seasonal to interannual variability, day-to-day variability is more difficult to explain and is the result of several different mechanisms. Figure 1.7 shows the observed diurnal tidal amplitudes at 85 km averaged for 4 days (black) in comparison to the averaged amplitudes for 60 days (red). Tides vary significantly from one day to another day. However, ground-based observations cannot resolve the tidal spectrum in terms of migrating and nonmigrating tides, a task that requires global satellite-borne observations. Only a few studies that clearly and unequivocally identify short-term variability in the tidal frequency/wavenumber spectrum (e.g., Lieberman et al., 2015) have been carried out, due to the insufficient time resolution of standard (Fourier-based) satellite diagnostics that use spectral space/time fit methods to extract the tidal spectrum. As such, the short-term tidal variability (tidal weather) is poorly understood in comparison to tidal variations on a seasonal or longer timescale (tidal climate). In Chapter 2, the deconvolution technique used to retrieve short-term tidal variability from satellite observations is overviewed.

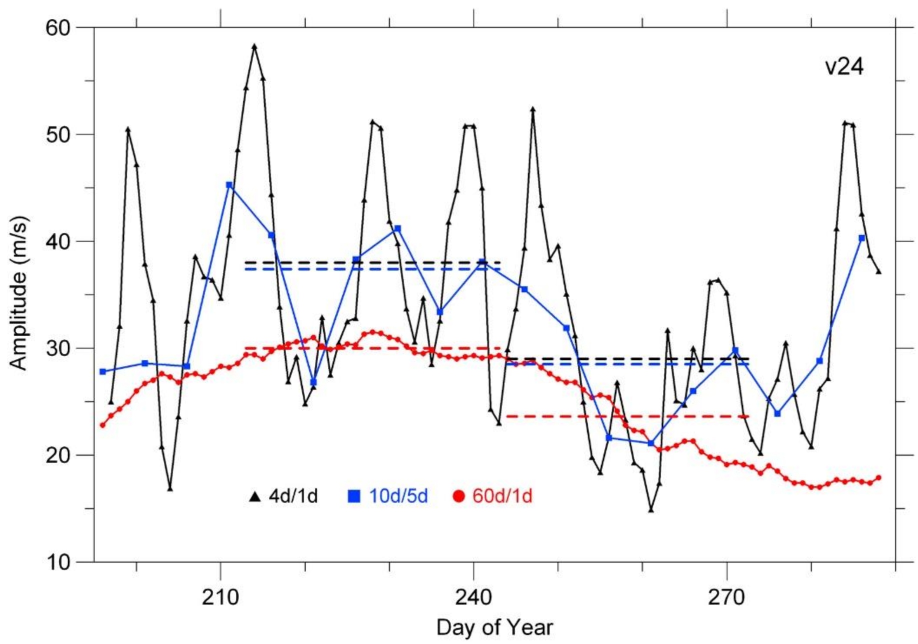

Figure 1.7: The meridional diurnal tidal amplitudes in meteor radar observations at 85 km over the period July-October during 2005 for 4-day, 10-day and 60-day composite analyses represented by black, blue, and red lines. (Kumar et al., 2014)

Here, the overarching goal of the thesis is to address the following science objectives using satellite short-term tidal diagnostics:

1. What are the statistical characteristics of the short-term tidal variability on various timescales?
2. What are the underlying physical mechanisms?

With this study, the effort is to understand how various propagation and forcing conditions modulate day-to-day tidal variability -in other words- under which atmospheric conditions the short-term tidal variability will be largest. This is important for space weather prediction, as discussed in section 1.1. Model studies suggest that, in addition to variations due to changes in solar heating and the background zonal mean winds, day-to-day tidal variability can also result from local changes of the apparent tidal amplitudes and phases from tidal-GWs interactions, or the excitation and modulation of nonmigrating tides due to tidal-PWs interactions (Riggin et al., 2003; Riggin & Liebermann, 2013; Liu & Hagan, 1998; Teitelbaum, 1991; Lieberman et al., 2015). Non-linear interactions of tides and PWs as a significant source of day-to-day tidal variability have been reported by several studies using ground-based observations (Nakamura et al., 1997; Pancheva et al., 2002; She et al., 2004), satellite observations (Lieberman et al., 2004; Liu et al., 2007; Kumari & Oberheide, 2020), and numerical modeling and simulations (Chang et al., 2011; Pedatella et al., 2012; Hagan & Roble, 2001; Angelats i Coll & Forbes, 2002; Vitharana et al., 2019). As mentioned in Chapter 2, the tidal amplitudes and phases can be obtained from satellite global observations on a day-to-day basis and this thesis uses available tidal timeseries during 2002-2019 from the TIMED satellite. One of the goals of this thesis is to analyze the observed day-to-day tidal variability on various PW timescales. Chapter 3 addresses the details of statistical analysis as a part of this thesis. The effort is to understand what causes the characteristics of changes in day-to-day variability of tides on different temporal scales and also to further investigate whether the propagation and forcing conditions such as QBO, ENSO, and solar cycle on interannual timescales also impact the day-to-day tidal variability on various PWs timescale. A major part of Chapter 3 has been published in Kumari & Oberheide, (2020). Chapter 4 includes the analysis on intraseasonal timescales in addition to their underlying causes. To explain intraseasonal oscillations in the MLT region, Eckerman et al. (1997) suggested that tropospheric convection associated with the Madden-Julian Oscillation (MJO) modulates the intensity of upward-propagating GWs and tides. Briefly, the MJO is an eastward moving disturbance near the equator (±30°) that typically recurs every ~30-90 days in tropical winds, clouds, rainfall and many other variables (Zhang, 2005) which is known to modulate stratospheric GWs, GW drag and zonal winds (e.g. Alexander et al., 2018). Major parts of Chapter 4 have been published in Kumari et al. (2020) and submitted as Kumari et al. (2021). In summary, long duration of day-to-day tidal observations provides an unprecedented opportunity to explore systematic connection between various propagation and forcing conditions such as stratospheric QBO, ENSO, solar cycle, MJO and MLT tides. Lastly, the findings of this thesis are enumerated in Chapter 5 with their importance in broad understanding of space weather predictions in the ionosphere-thermosphere region.

CHAPTER TWO

SATELLITE OBSERVATIONS OF SHORT-TERM VARIATIONS IN TIDES

2.1 Satellite Tidal Diagnostics

Slowly precessing satellite-borne instruments in a low Earth orbit usually sample the atmosphere at two local solar times a day for a given latitude. How to deconvolve such satellite observations into associated tidal components and periods? The common practice is to bin the observations into time intervals (e.g., 60 days for TIMED, 27 day for ICON) spanning 24 hours of local time (LT) (Salby, 1982; Lieberman, 1991; Talaat & Lieberman, 1999). Note that this method limits the study of short-term changes in tides as 60-day averaging (for TIMED) is involved for each analysis. This is due to the lack of 24 hours sampling in a given day; SABER sampling has been studied by Oberheide et al. (2003). The TIMED satellite is in a 625 km orbit of 74.1^{o} inclination. SABER (Russell III et al., 1999) is one of the four instruments on the TIMED satellite. The instrument was designed to study the energy budget, chemistry, and dynamics of the middle and upper atmosphere, especially in the MLT region. SABER's limb measurements cover the spectral range 1.27-17 µm. Temperature profiles are retrieved from the 15 µm and 4.3 µm CO_2 channels (Rezac et al., 2015) between ~20-110 km, and 53^{o}S and 83^{o}N or 53^{o}N and 83^{o}S, depending on the TIMED yaw cycle. Day and nighttime measurements are made routinely. The yaw cycle refers to the TIMED spacecraft changing its orientation every 60 days in order to keep the spacecraft facing the anti-Sun side. The TIMED spacecraft was launched in December 2001 and the SABER instrument has collected data continuously since January 25, 2002. TIMED takes 90 minutes to complete one orbit and thus it orbits Earth 15 times in a given day. The orbit precession of 12 minutes per day towards earlier times for ascending and descending orbit nodes, respectively, then results in a full 24 hours local time coverage every 60 days. Ascending (asc) orbit nodes are the instrument footprints when the satellite moves from south to north and descending (dsc) orbit nodes are the footprints for north to south movement. Figure 2.1 shows the SABER asc and dsc orbit sampling on a given day. The error estimate of measured temperature values in the MLT region varies up to 2.5 K below 100 km and 10 K above 100 km (Rezac et al., 2015).

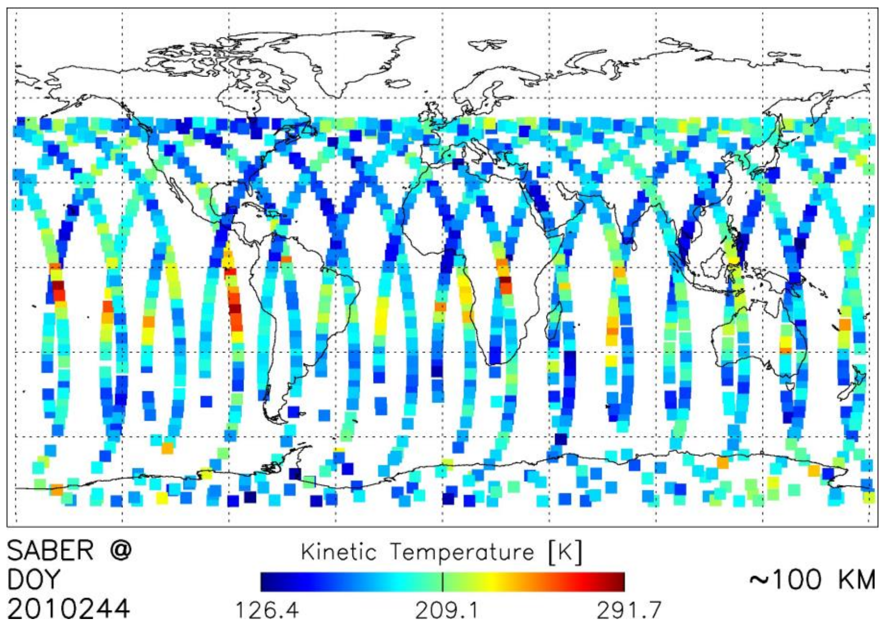

Figure 2.1: Temperature measurements along the SABER measurement track at 100 km altitude on 1st September 2010.

Basically, 60-days of SABER onboard TIMED observations of temperature are compiled into satellite-related coordinates and the spectral-time spectrum of dataset then provides observed global tidal oscillations, as 60-day averages. The oscillations corresponding to the whole tidal spectrum at each latitude can be expressed as a function of local solar time t as $\sum_{s,n} T_{s,n} \cos\left(\omega_n\left(t - t_{s,n}\right) - \lambda(s + n)\right)$, where wave frequency is

$\omega_n = \frac{2n\pi}{24} hr^{-1}$ and longitude λ. The $\lambda(s+n)$ term comes from the fact that the tides are analyzed in local time (LT, i.e., in rotating Earth's frame as Earth rotates beneath satellite measurement tracks/orbits) rather than in universal time (UT) and $t_{UT} = t_{LT} - \frac{\lambda}{2\pi} * 24$. The Fourier fits of the tidal spectrum to the binned data provide tidal amplitudes and phases in terms of various zonal wavenumbers ($|s| = (1, 2, \ldots)$; eastward; $s>0$ and westward; $s<0$) for each period in harmonics of a day (diurnal; $n=1$ and semidiurnal; $n=2$). Note that the nomenclature here for eastward and propagating waves differs from Chapter 1, where s was taken as a positive integer and positive values of ω correspond to eastward propagating and negative values to westward propagating waves. In this chapter, the Fourier fitting considers ω a positive integer while the sign of s determines the direction of propagating tidal waves. Further as discussed before, the spacecraft precesses through 24 hrs in LT over ~60 days, thus 60-day combined data is needed for the Fourier fitting. Consequently, 60-day averaging cannot resolve short-term (a few days) tidal variability.

Another frequently used approach for short-term tidal analyses is to analyze the differences between the daily measurements taken on the asc and dsc orbit nodes of the satellite (e.g., Wu et al., 1998; Ward et al., 1999; Oberheide et al., 2000, 2002). The background atmosphere (temperature/winds) including low-frequency PW-scale waves vanishes in the difference fields and, consequently, the difference can be interpreted as tidal in nature. However, it is impossible to calculate space-time spectra from the daily difference fields as the observed tidal signatures are a conglomerate of several tidal components and frequencies. The deconvolution of migrating and nonmigrating diurnal tidal components can be carried out at latitudes with a local solar time difference of ~12 hours between asc and dsc orbit nodes, owing to the vanishing semidiurnal signatures in the difference fields. This approach has been successfully applied to the MLT temperature data from CRISTA (Oberheide et al., 2002). A direct application of this method is, however, not suitable for most satellite instruments, because their maximum local solar time asc/dsc separation is considerably smaller than 12 hours, and some modifications of the analysis method are needed: non-vanishing semidiurnal tides in the asc/dsc differences are moved into the methodology error. For example, the difference corresponding to wave-4 will consist of diurnal components DW5 and DE3 and the semidiurnal components SE2, and SW6. Asc/dsc differences caused by the latter components will contribute to error analysis of the diurnal amplitudes while deconvolving DW5 and DE3 diurnal components is not trivial. For the SABER sampling, the maximum asc/dsc LT difference is 10 hours at 40°S and 9 hours at the equator, which is enough to allow for a reliable deconvolution of diurnal tidal components from the daily differences, as further explained in the following.

2.1.1 SABER Short-term Tidal Diagnostics

The tidal deconvolution approach has been developed in the early 2000's by Oberheide et al. (2002). The important characteristics of the approach are summarized in the following as it is used to produce the baseline tidal set for the further analysis in Chapters 3 and 4. A detailed mathematical treatment can be found in Oberheide (2007). The approach with asc/dsc differences, also called "deconvolution" method, has been validated and proven its usefulness for studying the short-term variability of various diurnal tides using WINDII and SABER data (e.g., Lieberman et al., 2013, 2015; Oberheide et al., 2015; Pedatella et al., 2016). An interesting outcome of this method was that the diagnosed day-to-day DE3 variability on timescales of days to weeks from SABER tidal deconvolution approach has been shown to be connected to short-term variability in the ionosphere and upper thermosphere (Pedatella et al., 2016).

Tidal Deconvolution

The approach starts with differencing asc and dsc SABER temperatures (ΔT). As discussed, all semidiurnal tidal components must vanish in ΔT when there is 12 hr time difference(Δt) between asc and dsc measurements, as they are observed in phase on both the asc and dsc orbit nodes (Oberheide et al., 2002). The remaining patterns in ΔT can then be attributed to diurnal tides (assuming negligible terdiurnal tides with 8 hrs period). Amplitude and phase calculations are carried out exactly as described in detail by Oberheide et al. (2000) for the migrating tide, and by Oberheide et al. (2002) for the nonmigrating components. An important assumption of this technique is that the short-term variability originating from the asc-dsc orbit node differencing still assumes constant amplitudes and phases within one day of observations. The detrended asc and dsc daily data are separately binned into 5° latitude bands and fitted to $\sum_{s,n} T_{s,n} \cos\left(\omega_n\left(t - t_{s,n}\right) - \lambda(s+n)\right)$ using a least squares fit technique for effective zonal wavenumbers s′=|s + n| from 0–6. This results in,

$$T^{asc} = \sum_{s,n} T_{s,n} \cos\left(\omega_n\left(t_{asc} - t_{s,n}\right) - \lambda(s+n)\right) + T_b \quad [E2.1]$$

$$T^{dsc} = \sum_{s,n} T_{s,n} \cos\left(\omega_n\left(t_{dsc} - t_{s,n}\right) - \lambda(s+n)\right) + T_b \quad [E2.2]$$

where T_b is for the non-tidal background.

Migrating Diurnal tide

For n=1 and s=-n i.e., s′=0 (migrating diurnal component)

$$\Delta T = T^{asc} - T^{dsc} = T\cos\left(\frac{\pi}{12}\left(t_{asc} - t_{1,1}\right)\right) - T\cos\left(\frac{\pi}{12}\left(t_{dsc} - t_{1,1}\right)\right) \qquad [E2.3]$$

Therefore,

$$\Delta T = -2T\sin\left(\frac{\pi\,\Delta t}{12*2}\right)\ \sin\left(\frac{\pi}{12}\left(\frac{1}{2}(t_{asc} + t_{dsc}) - t_{1,1}\right)\right) \qquad [E2.4]$$

$$\text{or,}\quad \Delta T' = 2T\ \cos\left(\frac{\pi}{2} + \frac{\pi}{12}\left(\frac{1}{2}(t_{asc} + t_{dsc}) - t_{1,1}\right)\right) \qquad [E2.5]$$

where, $\Delta t = t_{asc} - t_{dsc}$ & $\Delta T' = \Delta T/\sin\left(\omega_1 \frac{\Delta t}{2}\right)$

Note that for the migrating (s′=0, s=-n) diurnal and semidiurnal tides, these components are longitude-independent ($\lambda(s + n) = 0$) in the local solar time representation. They are observed as zonally symmetric oscillations in the satellite data. For $\Delta t = t_{asc} - t_{dsc} = 12$ hrs, one gets $\sin\left(\omega_1 \frac{\Delta t}{2}\right) = 1$, however for SABER $\Delta t = 9$ hrs at equatorial latitudes, this results in $\sin\left(\omega_1 \frac{\Delta t}{2}\right) < 1$. This value can be absorbed on the left hand side of the equation E2.4 by substituting $\Delta T' = \Delta T/\sin\left(\omega_1 \frac{\Delta t}{2}\right)$, as shown in the equation E2.5. Briefly, the zero temperature nodes in $\Delta T'$ as well as the $\Delta T'$ minima/maxima provide the phase information from which the amplitude can be derived. Zero nodes, $\Delta T' = 0$, occur at altitudes where the tidal perturbations are observed in phase on both the asc and dsc orbit nodes. As such, $t_{1,1} = \frac{1}{2}(t_{asc} + t_{dsc})$; the value of $t_{1,1}$ is used to derive amplitudes T at $\Delta T' = 0$ heights. Also, at altitudes of minima/maxima, the vertical gradient will be zero. So,

$$\frac{\partial \Delta \mathrm{T}}{\partial \mathrm{z}} = \frac{\pi}{12}\frac{\partial \mathrm{t}_{1,1}}{\partial \mathrm{z}} * \left(\mathrm{T}\sin\left(\frac{\pi}{12}\left(\mathrm{t}_{\mathrm{asc}} - \mathrm{t}_{1,1}\right)\right) - \mathrm{T}\sin\left(\frac{\pi}{12}\left(\mathrm{t}_{\mathrm{dsc}} - \mathrm{t}_{1,1}\right)\right)\right) + \frac{\partial \mathrm{T}}{\partial \mathrm{z}}\frac{\Delta \mathrm{T}}{\mathrm{T}} \quad [E2.6]$$

$$\text{or,} \quad \frac{\partial \Delta \mathrm{T}}{\partial \mathrm{z}} = \frac{\pi}{12}\frac{\partial \mathrm{t}_{1,1}}{\partial \mathrm{z}} * 2\mathrm{T}\sin\left(\frac{\pi}{12}\frac{\Delta \mathrm{t}}{2}\right)\cos\left(\frac{\pi}{12}\left(\frac{1}{2}(\mathrm{t}_{\mathrm{asc}} + \mathrm{t}_{\mathrm{dsc}}) - t_{1,1}\right)\right) \quad [E2.7]$$

$$\&, \frac{\partial \Delta \mathrm{T}'}{\partial \mathrm{z}} = \frac{\pi}{12}\frac{\partial \mathrm{t}_{1,1}}{\partial \mathrm{z}} * 2\mathrm{T}\cos\left(\frac{\pi}{12}\left(\frac{1}{2}(\mathrm{t}_{\mathrm{asc}} + \mathrm{t}_{\mathrm{dsc}}) - t_{1,1}\right)\right) = 0 \quad [E2.8]$$

Neglecting $\frac{\partial \mathrm{T}}{\partial \mathrm{z}}\frac{\Delta \mathrm{T}}{\mathrm{T}}$ from equation E2.6 (as a second order term), it is used to solve for T amplitudes at minima/maxima of $\Delta \mathrm{T}$ or $\Delta \mathrm{T}'$ heights (equations E2.7-2.8), where $\Delta \mathrm{T}' = \Delta \mathrm{T}/\sin\left(\omega_1 \frac{\Delta \mathrm{t}}{2}\right)$. Interpolation is then used to create a complete height profile for the migrating tidal amplitude. Phase angles are inferred at the maxima, minima, and zero crossing of the difference $\Delta \mathrm{T}'$ with the assumption of downward phase progression in LT, which is reasonable since the latter corresponds to upward energy flux and tidal forcing in the lower atmosphere, as explained in Chapter 1. There is potential for aliasing by semidiurnal tides when the $\Delta \mathrm{t}$ is not 12 hours. This is the case for SABER where the equatorial local time difference is 9 hours. The magnitude of this semidiurnal tidal aliasing depends on season, latitude, and altitude. SABER diagnostic using 60-day running mean Fourier fits indicates ≥10 K amplitude of the semidiurnal tide at altitudes ≥100 km in the 20–40° latitude range but comparatively small (≤5 K) amplitudes equatorward of 20° (e.g., Akmaev et al., 2008). Note that semidiurnal tidal amplitudes decrease rapidly toward lower altitudes at all latitudes, that is, ≤5 K in the 20–40° latitude range at 90 km (Pancheva et al., 2009). The semidiurnal aliasing can be estimated as the semidiurnal amplitude times $\sin\left(\frac{\pi}{6}\frac{\Delta \mathrm{t}}{2}\right)$ which is generally on the order of ≤1.2 K equatorward of 20° but substantially larger poleward of 20° at altitudes above 90 km (Vitharana et al., 2019). The analysis done in this thesis using diurnal tides is focused on altitudes below 100 km and at equatorial latitudes, where the semidiurnal component aliasing is minimum.

Nonmigrating Diurnal tides

The analysis of the observed nonmigrating diurnal tides (i.e. $s' \neq 0$) from ΔT fit results is much more complicated. Satellite instruments measuring at constant LT at a specific latitude and orbit node (such as the daily SABER measurements) imply that the observed zonal wavenumber s' corresponds either to a component with $s = s' - n$ or to a component with $s = -s' - n$. How does one deconvolve ΔT into their corresponding tidal components? Using trigonometric expressions, the difference of asc and dsc tidal fit results can be expressed for $\Delta t = t_{dsc} - t_{asc}$ as,

$$\Delta T = 2 \sum_{s,n} T_{s,n} \sin\left(\omega_n \frac{\Delta t}{2}\right) \sin\left(\omega_n (t_{asc} - t_{s,n}) + \omega_n \frac{\Delta t}{2} - (s+n)\lambda\right) \qquad [E2.9]$$

Note that Δt is defined differently here than for the migrating diurnal tide case above, for mathematical simplicity. The factor $\sin\left(\omega_n \frac{\Delta t}{2}\right)$ accounts for the LT difference between the asc and dsc measurements (i.e., 9-10 hours for SABER). For a given Δt and $n = 1$ i.e., $\omega_1 = \frac{\pi}{12}$ diurnal tides,

$$\Delta T = 2 \sum_{s,1} T_{s,1} \sin\left(\omega_1 \frac{\Delta t}{2}\right) \sin\left(\omega_1 (t_{asc} - t_{s,1}) + \omega_1 \frac{\Delta t}{2} - (s+1)\lambda\right) \qquad [E2.10]$$

This assumes that semidiurnal tides can be considered as part of the diurnal tide error, similar to the migrating diurnal tide case. As explained above, for SABER $\Delta t = 9$ hrs at equatorial latitudes, and $\sin\left(\omega_1 \frac{\Delta t}{2}\right)$ value can be absorbed into the left hand side of the equation E2.10 by substituting $\Delta T' = \Delta T/\sin\left(\omega_1 \frac{\Delta t}{2}\right)$ and the remaining second term is a superposition of various zonal wave numbers. Depending on the yaw-associated spacecraft orientation for SABER, $\Delta t \approx 7$ hr or $\Delta t \approx 11$ hr at 20–40° latitude, and $\Delta t \approx 9$ hr at the equator.

As discussed, the observed zonal wavenumber s′ is a linear combination of two tidal components (s = s′ − n and s = −s′ − n). To exemplify this for s′=1, the linear combination of two diurnal tidal components with s=-2, 0 (DW2 and D0) will be measured in the $\Delta T'$ difference as follows:

$$\Delta T' = 2T_{-2,1} \sin\left(\omega_1(t_{asc} - t_{-2,1}) + \omega_1 \frac{\Delta t}{2} + \lambda\right)$$

$$+ 2T_{0,1} \sin\left(\omega_1(t_{asc} - t_{0,1}) + \omega_1 \frac{\Delta t}{2} - \lambda\right) \qquad [E2.11]$$

$$\text{or, } \Delta T' = T_0 \sin\left(\omega_1 t_{asc} + \omega_1 \frac{\Delta t}{2} + \lambda - \Theta\right) \qquad [E2.12]$$

where $T_o^2 = T_{-2,1}^2 + T_{0,1}^2 + 2T_{-2,1}T_{0,1}\cos(\phi_{-2,1} - \phi_{0,1})$, $\phi_{-2,1} = \frac{\pi}{2} + \frac{\pi}{12}(t_{asc} - t_{-2,1})$, and $\phi_{0,1} = \frac{\pi}{2} - \frac{\pi}{12}(t_{asc} - t_{0,1})$.

Here, the parameters T_0 and Θ are easily obtained from the fit of the $\Delta T'$. They need to be deconvolved into amplitudes ($T_{-2,1}, T_{0,1}$) and phases ($\phi_{-2,1}, \phi_{0,1}$) of the two underlying tidal components. For altitudes with $\phi_{-2,1} - \phi_{0,1} = \Psi = \pm\pi/2$, one gets $\overline{T}^2 = T_{-2,1}^2 + T_{0,1}^2$, which is found to lie between maxima and minima in adjacent heights, as shown in Figure 2.2 with red points.

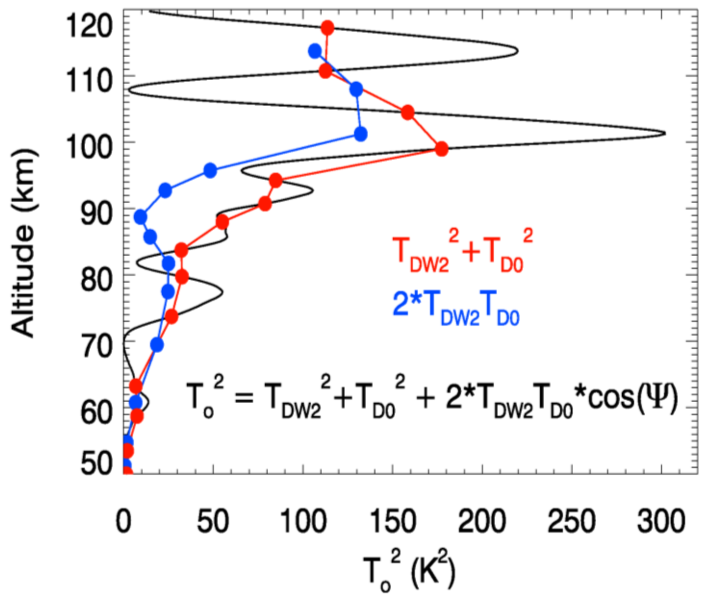

Figure 2.2: Squared Wave-1 amplitude T_0^2 depends on amplitudes of tidal components DW2 (s=-2), D0 (s=0) and a phase factor Ψ (phase difference between two tidal components) which can be evaluated at extrema and midpoints. Phase factor Ψ is obtained at extrema (maxima/minima, red dots) and mid points (blue dots) of T_0^2. (Oberheide, 2007)

At maxima and minima level (blue points in Figure 2.2) $\phi_{-2,1} - \phi_{0,1} = 0, \pm\pi$, and the cosine term is ±1 and $2T_{-2,1}\,T_{0,1} = A = T_0^2 \mp \overline{T}^2$, and A can consequently be solved for. The profile of A and $\overline{T}^2$with altitude is calculated by linear interpolation. The sign of phase is chosen such that only upward propagating tides are allowed (see details in Oberheide et al., 2002), which makes sense since tides propagate upward as explained in Chapter 1. This implies that the phases of the two components to be deconvolved decrease with height.

DE3 can be obtained by deconvolving wave-4 *($n = 1, s' = 4, s = -5{,}3$)* observations in DW5 and DE3 using the same concept. The resulting amplitude error is ~0.5 K. See Oberheide et al. (2000, 2002) for complete mathematical details of the solution method including error estimates. Figure 2.3 shows the deconvolved SABER DE3 tidal amplitudes in the MLT region during 2008 in comparison to Fourier fits of the 24 hr LT tidal observation composites of 60 days.

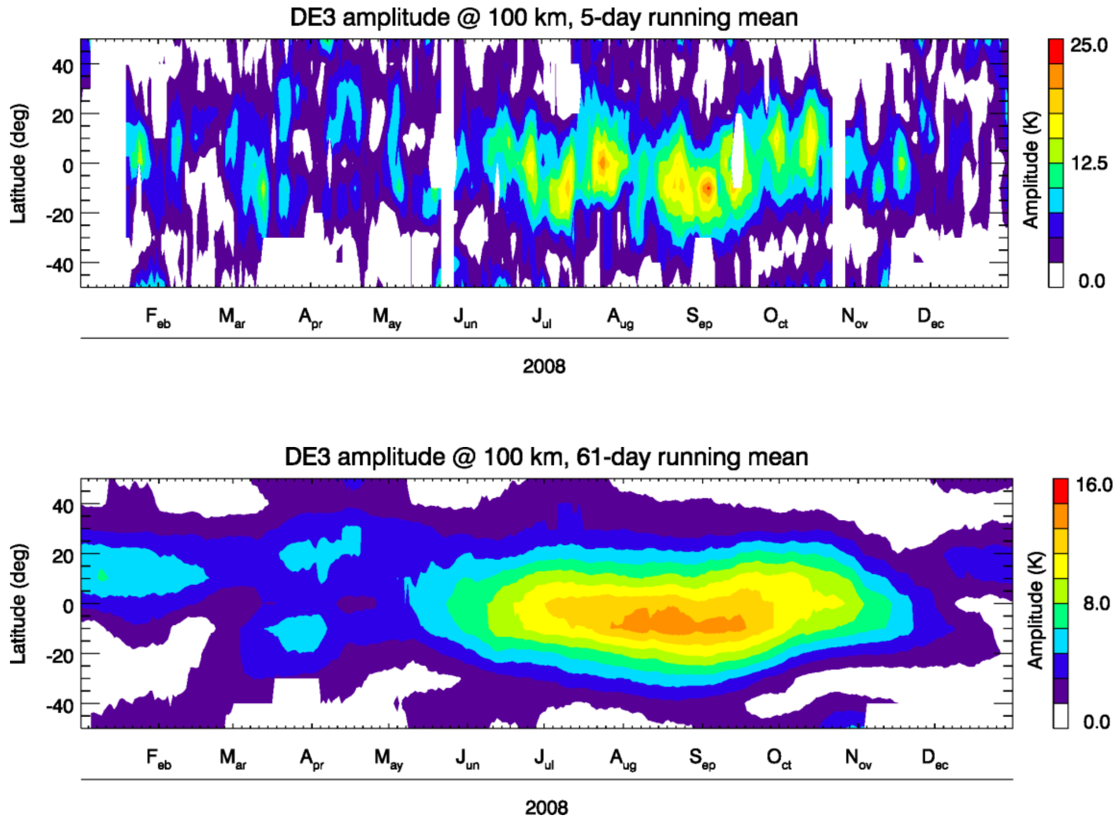

Figure 2.3: 5-day running mean of DE3 amplitudes retrieved from SABER temperatures during 2008 using (top) tidal deconvolution approach i.e. day-to-day variability and (bottom) Fourier fits of the 24 hrs LT tidal observation composites of 60 days i.e. 60-day averaged variability. Note the different colorbar values for both plots. (AGU Fall meeting 2015 SA41B-2327 talk)

A 60-day vector averaging of amplitudes and corresponding phases (not shown) from the deconvolution approach reproduces the amplitudes from standard Fourier fitting of 60-day combined data (full LT coverage, composite day, Figure 2.3b). The range of tidal temperature values is larger than the 60-day averaged tidal amplitudes. This highlights the importance of short-term tidal diagnostics as the averaging smooths the variability by more than ~35%. Data gaps may occur every 60 days at all latitudes due to the TIMED yaw cycle and occasionally at individual latitudes when the tidal deconvolution algorithm failed to converge. Linear interpolation is used to fill the data gaps. Figures 1.4a and 1.4c in Chapter 1 illustrate the 11-day smoothed (migrating) DW1 and (nonmigrating) DE3 daily amplitudes for the year 2009 and 95 km. The observed short-term amplitude variability is considerable and frequently reaches ~10 K for DE3 tide and ~20K for DW1 tide within a few days. This is also evident in Figure 2.4 which shows the 11-day running mean (for plotting purpose) of the DE3 amplitudes for the years 2002-2018 retrieved from the SABER tidal deconvolution approach.

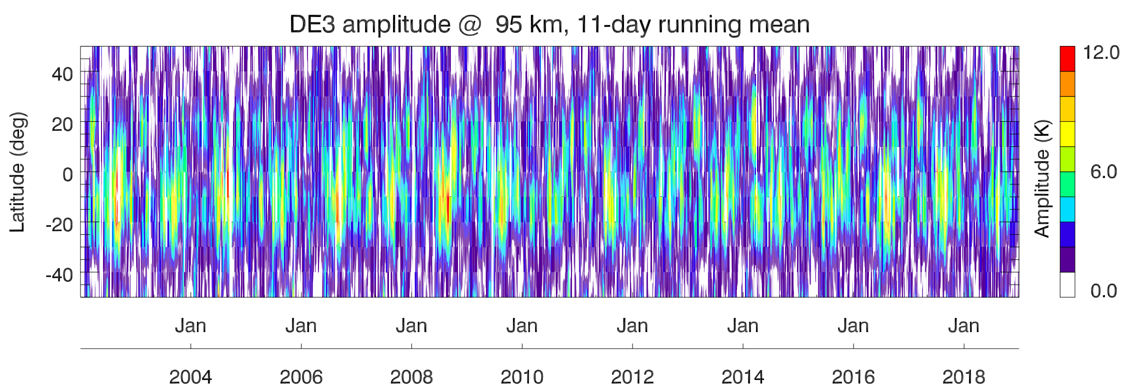

Figure 2.4: 11-day running mean of the DE3 amplitudes from the SABER tidal deconvolution approach.

The long duration of timeseries can be used to study tidal variability on day-to-day to interannual timescale at each altitude and latitude in the MLT region.

2.1.2 Hough Mode Extension Fits

For further analysis, it is important to note that classical tidal theory (see Chapter 1) shows that the DE3 tide is largely a superposition of a symmetric (vertical wavelength $\lambda_z \approx 56$ km) and an antisymmetric ($\lambda_z \approx 30$ km) mode with respect to the equator, while the DW1 tide largely consists of the first symmetric mode ($\lambda_z \sim 27$ km) (e.g., Oberheide & Forbes, 2008). Seasonal and interannual variation of each of these modes are different from each other as they depend on efficient forcing and interaction with the mean flow (background). The symmetric mode of DW1 dominates during Northern Hemisphere (NH) spring and the antisymmetric mode of DE3 always dominates in NH winter while the symmetric mode of DE3 dominates in NH summer and fall. The symmetric modes are mainly forced due to tropospheric heating, while the two dominant modes in DE3 are as a consequence of tropospheric heating as well as mean zonal wind variations in the stratosphere and lower mesosphere (Oberheide & Forbes, 2008; Zhang et al., 2012). Depending on the latter, wave energy is transferred from one mode to another (mode coupling), causing, for example, a bite-out around an altitude of 80 km in the symmetric mode in NH winter with simultaneous amplification of the antisymmetric mode. On the other hand, the mean zonal winds are more favorable for the upward propagation of the symmetric mode in NH summer than for that of the anti-symmetric mode. See Zhang et al. (2012) for a detailed discussion. Mean zonal wind variations can therefore impact the symmetric and antisymmetric modes quite differently, along with tidal heating variations. Analyzing the observed short-term tidal variability needs to account for this. In the next step, the observed DW1 and DE3 amplitudes and phases are thus projected into symmetric and antisymmetric modes using Hough Mode Extension (HME) fitting. Figure 2.5 shows the altitude and latitude structure of amplitude and phase of DE3 HME1 and DE3 HME2 (DW1 HME1 not shown here).

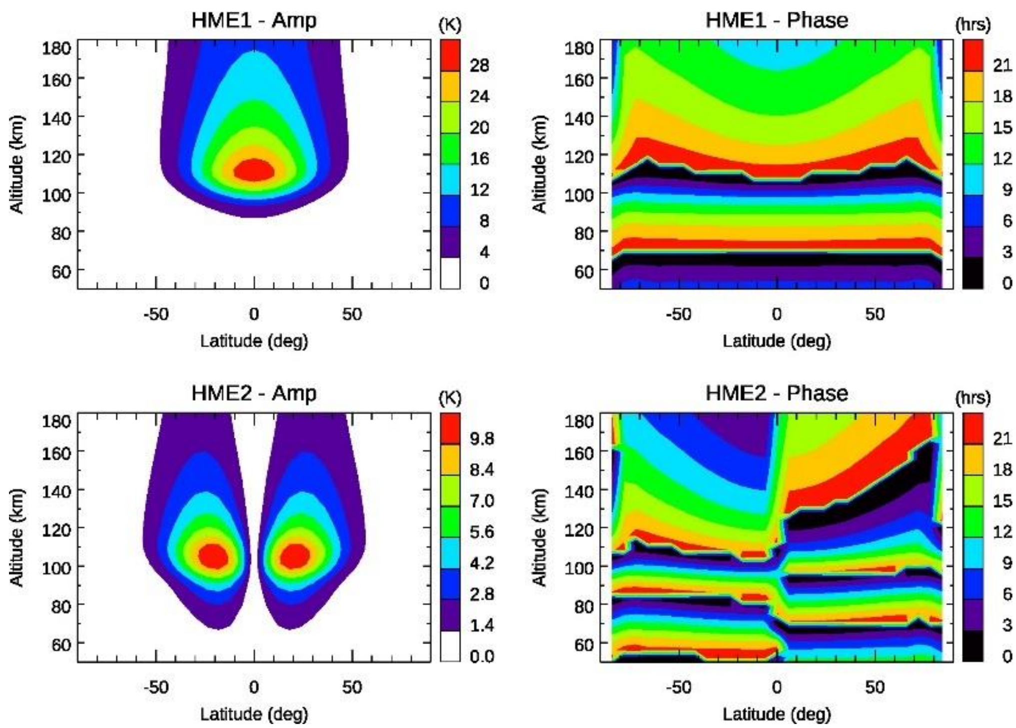

Figure 2.5: (Left) Amplitudes and (right) phases of altitude-extended of first (top) symmetric and first (bottom) antisymmetric Hough modes of DE3 tidal component in temperatures and the magnitude and phase are arbitrary in HMEs and are then constrained by fits to the data. Note that the figure shows Hough mode extension and not Hough modes. (Supplementary figures of Kumari & Oberheide (2020))

HMEs are extensions of classical Hough functions in that they account for tidal dissipation (Lindzen et al., 1977). The latter makes the classical tidal equations inseparable and instead of latitude-dependent Hough functions and exponential amplitude growth with height, one obtains two-dimensional (latitude, altitude) Hough Mode Extensions from numerical solutions of the tidal equations with dissipation. See Oberheide & Forbes (2008) for a detailed discussion and the numerical HME computation. Each HME is a self-consistent latitude vs. height set of amplitudes and phases in tidal temperature, winds, and density, from pole-to-pole, 0-390 km, and time-independent.

The observed DW1 and DE3 amplitudes and phases from the tidal deconvolution approach are then fitted between 30^{o}S-30^{o}N and 90-110 km to the first symmetric HME (HME1, corresponding to the 1st symmetric Hough mode) and first antisymmetric HME (HME2, corresponding to the 1st antisymmetric Hough mode) in complex space, resulting in two complex fit coefficients for each day. The lower fit boundary of 90 km is chosen to only fit data above the mode coupling region where the HME fit approach is applicable (Oberheide and Forbes, 2008). The latitude range is chosen to cover the amplitude maxima of both modes. Variations in these parameters do not change the results in an appreciable manner. Since the latitude/height information is completely contained in the HMEs (in the sense of a tensor basis), the fit coefficients are independent of latitude and altitude, and only depend on time. The rather complicated structure of the observed amplitudes and phases is thus reduced to two latitude- and altitude-independent complex coefficients for each day, from which amplitudes and phases can easily be reconstructed using the HMEs shown in Figure 2.5.

Figure 2.6a shows the 2018 DE3 amplitudes retrieved from SABER deconvolution, where data gaps (white color) occur every 60 days at all latitudes due to the TIMED yaw cycle and occasionally at individual latitudes when the tidal deconvolution algorithm failed to converge. Figure 2.6b shows the reconstructed amplitudes of DE3 after HME fits.

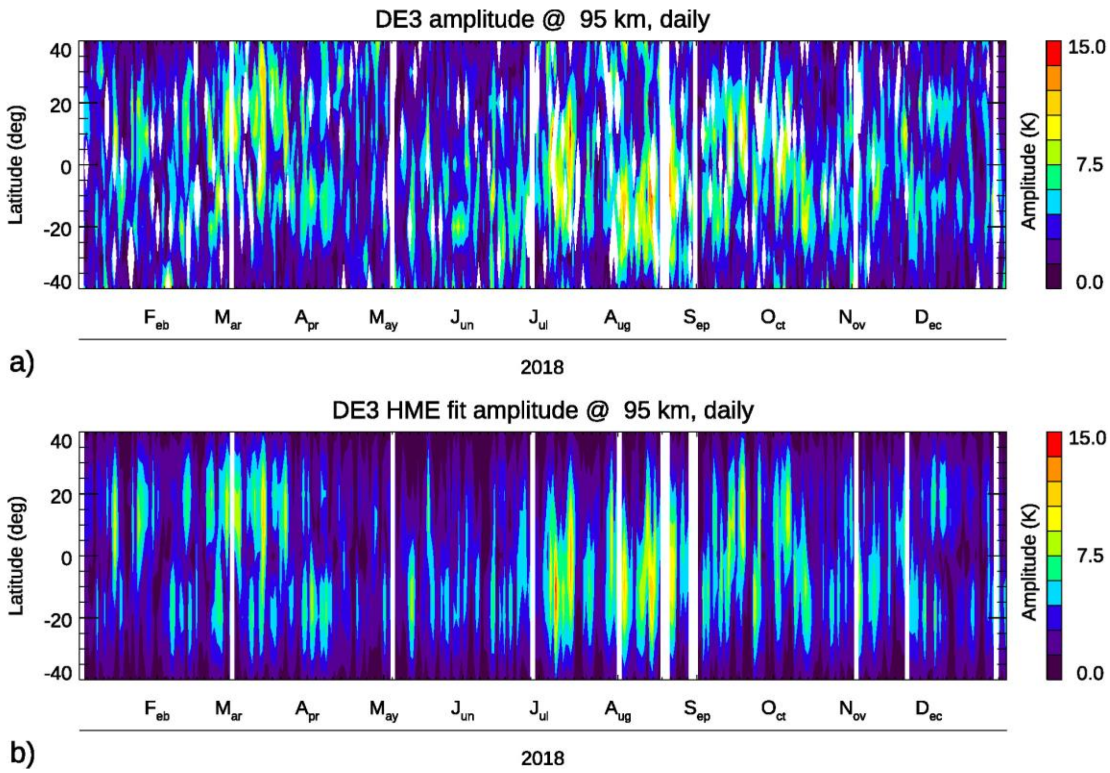

Figure 2.6: (a) Daily DE3 tidal temperatures from SABER for the year 2018 at 95 km. White color indicates data gaps. (b) Corresponding amplitudes from Hough Mode Extension (HME) fitting (Kumari & Oberheide, 2020).

The observed short-term amplitude variability is considerable and frequently reaches ~10 K within a few days. A 60-day vector averaging of Figure 2.6a amplitudes and corresponding phases (not shown) reproduces the amplitudes from standard Fourier fitting of 60-day combined data (full local time coverage, composite day, not shown). Most features of Figure 2.6a are preserved in the Figure 2.6b and differences are due to using HME1 and HME2 only. Adding higher order HMEs (2nd symmetric and anti-symmetric modes) would result in a closer match to the observations. However, their contribution is found to be comparatively small, and therefore the focus is on the HME1 and HME2 variability in the following. Omitting higher order HMEs in the fit does not pose a problem as HMEs (because of the orthogonal Hough modes) are orthogonal to each other. Overall, the amplitudes of the HME projections along with the tidal deconvolution error (~0.5K) yield a total error ~1K in tidal amplitudes.

Similar to Figure 2.6a, Figure 2.7a and 2.7b shows the DW1 and DE3 amplitudes obtained from SABER deconvolution during 2009 and, additionally, Figure 2.7c-e shows the reconstructed timeseries using individual HME modes during 2009 e.g., DW1(HME1(1)), DE3(HME1(1)) and DE3(HME2(2)) amplitudes after fitting HME1 and HME2.

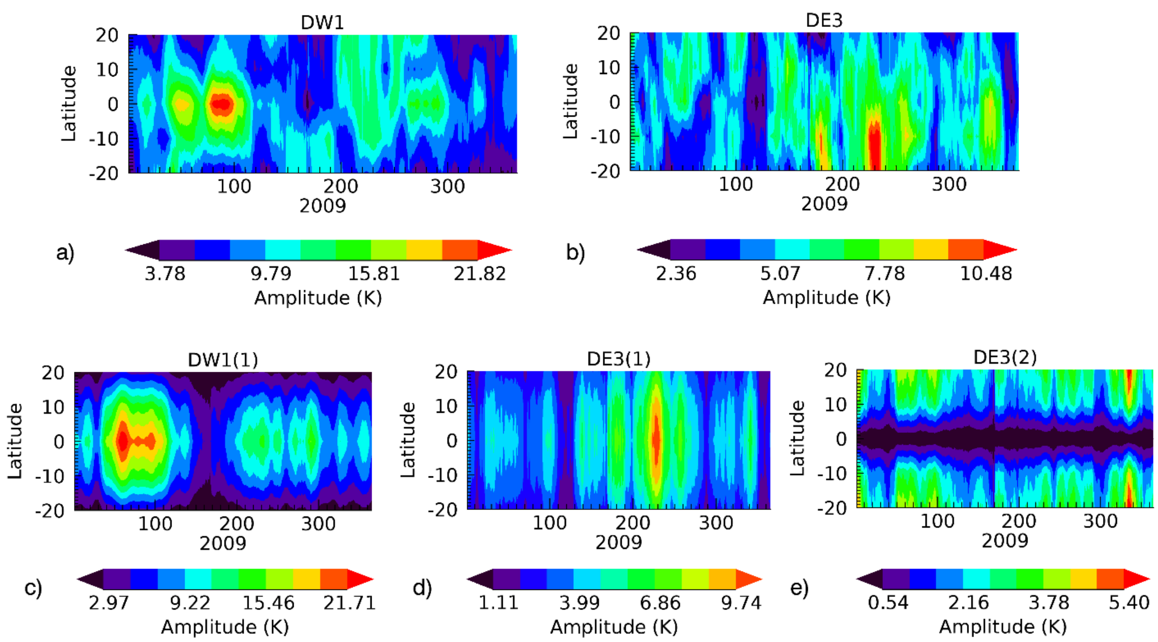

Figure 2.7: 11-day running mean of the daily (a) DW1 and (b) DE3 tidal temperature amplitudes from SABER for the year 2009 at 95 km after Hough Mode Extension (HME) fitting are shown as (c) DW1(HME1), (d) DE3(HME1), and I DE3(HME2).

Note that Figure 1.4 in Chapter 1 shows the DW1 and DE3 phases during 2009. While both HME1 and HME2 are important to retain major features of DE3 (Figure 2.6), the latitude/seasonal structure of first symmetric equatorial HME1 mode (Figure 2.7c) is enough to explain major features in DW1 tides (Figure 2.7a). Figures 2.6 and 2.7 clearly show that the whole three-dimensional (latitude, altitude, time) tidal temperature dataset can thus be reduced to one-dimensional (time) with complex fit parameters for DW1(1), DE3(1), and DE3(2), respectively. Figures 2.8a, 2.8c and 2.8e show the absolute value of the complex fit coefficients for DW1(1), DE3(1), and DE3(2). They are a measure for the relative strength of HME1 and HME2 as a function of time and as such unitless.

Figures 2.8b, 2.8d and 2.8f show the wavelet diagnostics (Torrence & Compo, 1998) of the coefficients which reveal a wide range of tidal variability in each mode, ranging from a few years to a few days, with already evident differences between the symmetric and antisymmetric modes of DE3, e.g., the missing/small QBO signal in the HME2 coefficients. As discussed earlier in section 1.2.3, variability on seasonal (Forbes et al., 2003, 2006; Oberheide & Forbes, 2008), annual, interannual (e.g., QBO (Oberheide et al., 2009) and ENSO (Warner & Oberheide, 2014)) timescales as a function of symmetric and antisymmetric modes has previously been studied. Nevertheless, short-term variability on less than a seasonal timescale is not well understood.

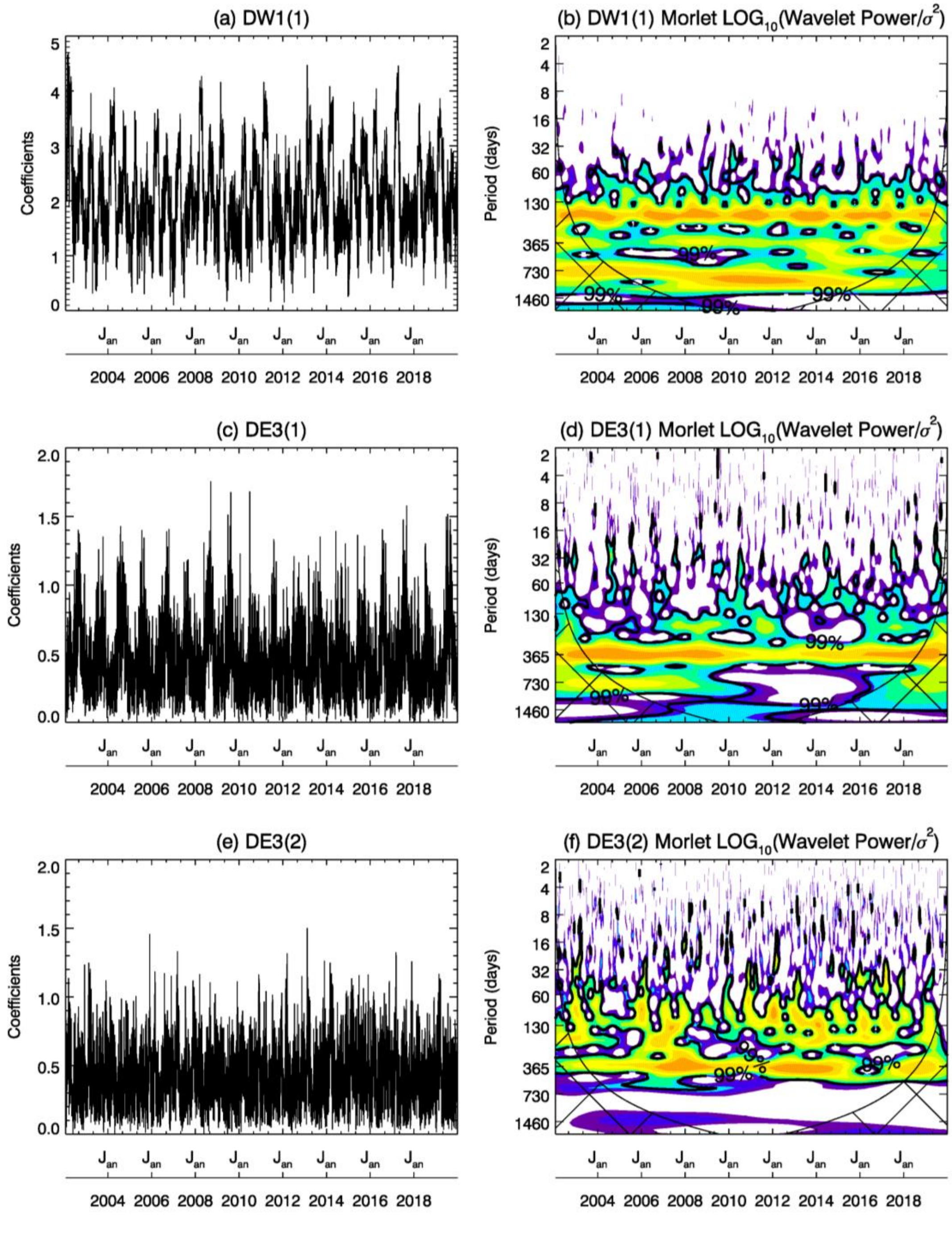

Figure 2.8: a) DW1(HME1), c) DE3(HME1), and e) DE3(HME2) coefficients with their Morlet wavelet power spectrum in b), d), and f), respectively. The black line indicates 99% confidence level and cross-hatched regions indicate the cone of influence (below the cone of influence, the results are not significant). The color indicates the magnitude of the periodic signals.

2.2 Short-Term Tidal Variability (Day-to-Day and Intraseasonal)

In the following, the focus is on the variability seen on an intraseasonal (30-90 day, Madden-Julian Oscillation) timescale and the <30-day variability related to tidal-planetary wave interactions. To delineate the tidal variability on different time scales, one can use the Lanczos bandpass filtering (Duchon, 1979) on tidal timeseries. Figure 2.9 shows the bandpass filter on 30-90-day and 2-30-day (<30-day) timescales for each of the tidal modes. From Figure 2.8, a comparison of tidal variability on timescales less than 30 days in the three tidal components shows that the DW1(1) day-to-day variation is not as prominent as DE3(1&2) day-to-day variations. This is also evident from Figure 2.9 as the variance of the tidal variability on <30-day timescale corresponding to the DW1(1) is 18% of the total variance, while for DE3(1) and DE3(2) the variances are 63% and 53%, respectively. The variances of the variability on intraseasonal (30-90-day) timescale for the three tidal modes are 9%, 11% and 13%, respectively, which indicates that the variability on day-to-day timescales is significantly larger than on intraseasonal timescales.

Wavelets allow one to estimate multi-scale temporal variations, but they do not allow one to gain physical insight into the causes of the short-term tidal variability and, equally important, how the short-term tidal variability changes on various temporal scales. As such, wavelets are useful to get a first impression of variability but not more. The next two Chapters 3 and 4 focus on understanding the causes of the short-term tidal variability, where the Bandpass-filtered coefficients (Figure 2.9) will be used for the analysis to study the causes of the short-term (both day-to-day and intraseasonal) variability in the two

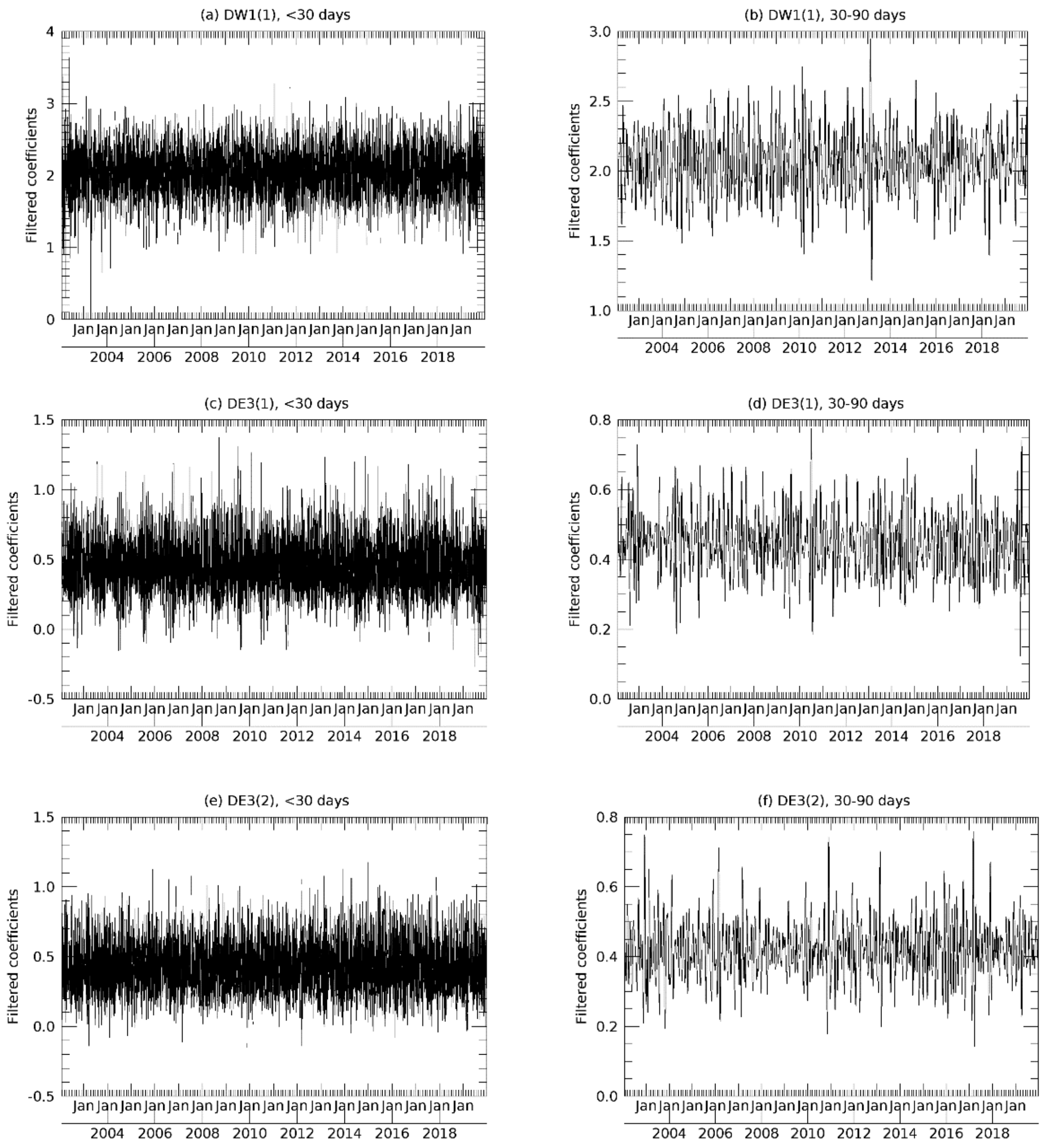

Figure 2.9: a)&b) DW1(HME1), c)&d) DE3(HME1), and e)&f) DE3(HME2) variability during 2002-2019 from SABER on day-to-day to few weeks (<30 days) and intraseasonal timescale (30-90 days), respectively.

diurnal tidal components and the corresponding three HME modes. Chapter 3 mainly focuses on understanding how the day-to-day tidal variability changes on various temporal scales, which is also helpful in understanding interhemispheric coupling due to the diurnal tides (DE3, DW1) and various PWs nonlinear wave-wave interactions. Here, interhemispheric coupling occurs as the DE3 and DW1 tides are mainly equatorial while PWs are mid latitude phenomena. Chapter 4 includes the analysis on the intraseasonal timescale, which is mainly due to the intraseasonal Madden-Julian Oscillation (MJO) in convection anomalies in the tropics. This is especially interesting as the MJO is a tropospheric phenomenon, but they can be important for accurate space weather prediction as there may be a significant ionospheric response to the MJO in the MLT tides. Chapter 4 focuses on understanding how the MJO-related effects modulate the tidal variability from the troposphere up to the MLT region. Understanding the causes of short-term tidal variability in the MLT region for various timescales is essential in order to effectively forecast space weather variations due to the upward propagating lower atmospheric tides as they have implications in the ionosphere and thermosphere region through the dynamo wind effect.

CHAPTER THREE

DAY-TO-DAY VARIABILITY IN DIURNAL TIDES

3.1 Tidal-Planetary Wave Interactions

Earlier studies such as Bernard (1981) and Manson et al. (1982) suggested that the day-to-day variation in tides is due to the local perturbations caused by the nonlinear wave-wave interactions of tides and PWs. Beard et al. (1999) investigated nonlinear coupling between tides and PWs and suggested that considerable tidal variability can be present due to the wave-wave interaction even in the absence of PWs in the observed region, since after the interaction tides may have propagated into another region of the atmosphere and lower frequency PWs may not have propagated to the observed region. The nonlinear coupling between tides and PWs was first investigated by Teitelbaum & Vial (1991) in the MLT region. The importance of nonlinearity depends essentially on the amplitude of the induced fluid velocity in the direction of the wave propagation. When two waves propagate simultaneously, the fluid velocity with a large component in the direction of propagation of one of the waves produces advection terms which can force secondary waves. Recent studies (e.g. Chang et al., 2011; Lieberman et al., 2015; Gan et al., 2017) showed the interaction of tides and PWs using observations and models and found a family of secondary waves (child waves) with beating frequencies ($f_{tide} \pm f_{PW}$) further interacting with tides, resulting in significant variability in tidal amplitudes on PW timescales. In other words, change in tidal amplitudes in the course of such a nonlinear interaction can be attributed to nonlinear advection transferring energy from the parent waves (tides and PWs) to the sum and difference child waves (Palo et al., 1998; Norton & Thuburn, 1999; Chang et al., 2009). Subsequently, these secondary waves beat with the tide to modulate the tidal amplitude with a period equal to that of the PW (wave-1 travelling normal modes e.g., westward propagating 5-day, 10-day, 16-day, and 23-day). Note that the nonlinear interactions between stationary (not travelling) PW modes and tides do not change the frequency of tides but can produce nonmigrating tides and broaden the zonal wave number spectra of the tides (Xu et al., 2013). Several studies report tidal modulation on various PWs timescales (2-30-day) using ground-based observations (Nakamura et al., 1997; Pancheva et al., 2002; She et al., 2004), satellite observations (Lieberman et al., 2004; Liu et al., 2007), and numerical modeling and simulations (Chang et al., 2011; Pedatella et al., 2012, Hagan & Roble, 2001; Angelats i Coll & Forbes, 2002, Vitharana et al., 2019). In this study, the focus is on tidal variability on PW timescales (i.e., <30-day) to study for tidal-PW interactions, in particular on the PW traveling normal modes. This is in order to delineate the causes of the short-term tidal variability on various PWs timescales.

From Chapter 1, the short-term tidal variability includes the range from intraseasonal (30-90-day) to day-to-day (<30-day) timescales. From Chapter 2, the baseline dataset to study the short-term tidal variability for this study can be obtained by the bandpass filtering of the tidal HME coefficients. The goal is to characterize variability from the filtered timeseries on different temporal scales due to the tidal-PW interactions, especially under variable tropospheric forcing and propagation conditions. As discussed in Chapter 1, vertically propagating atmospheric tides can also be impacted by propagation conditions such as the Quasi-Biennial Oscillation (QBO) and forcing conditions such as the El Niño–Southern Oscillation (ENSO), the Madden–Julian Oscillation (MJO) and the solar cycle. Apart from variations in the seasonal tides for such conditions (Oberheide et al., 2009; Warner & Oberheide, 2014; Yang et al., 2018; Nischal et al. 2019), there is a current lack of understanding as to whether the propagation and forcing conditions such as QBO, ENSO, solar cycle and MJO also impact the tidal variability on PW timescales. Dhadly et al. (2018) used (migrating) tidal wind observations from TIDI (TIMED Doppler Interferometer (Killeen et al., 2006; Wu et al., 2008a, 2008b)) and found a significant presence of the QBO in interannual variations of short-term (<30-day) migrating tidal variability but did not find a solar cycle signal. The interannual variations have been observed to produce teleconnection effects, since ENSO impacts the stratospheric QBO for more than a year (Sun et al., 2018) and the solar cycle signal depends on the stratospheric QBO (Labitzke & Loon, 1988). Briefly, QBO-solar cycle teleconnections effects in the polar vortex stability were recognized as the effects of the solar cycle became clearer if the (easterly/westerly) phase of the QBO was considered (Labitzke, 1982; Naito & Hirota, 1997). Therefore, the study of interannual variability needs to consider the composite influence of the solar cycle-QBO-ENSO on tidal amplitudes; however, the intra-annual variability may depend on MJO-QBO-ENSO teleconnections influence. This is because the MJO tidal-forcing can be contaminated by ENSO events as they may coexist in the tropical pacific. Thus, the overarching goal of this thesis is to establish the causes and relative impacts of short-term tidal variability under these forcing and propagation conditions. This chapter aims to identify changes in the <30-day short-term tidal variability of DW1(1), DE3(1), and DE3(2) coefficients and the atmospheric conditions under which the change is largest.

As such, the study of interannual variability of tidal variability on a 10-day PW timescale as part of this research has been published in Kumari & Oberheide (2020). The remainder of the Chapter is thus adopted from Kumari & Oberheide (2020) which discusses the development of a new framework based on information theory to study the tidal variability on various PW timescales. This framework is designed to observe complex processes across a wide range of temporal scales. Basically, it facilitates diagnostics for (statistical) pattern discovery in the variations of the short-term tidal variability. The pattern diagnostic can help us to understand the contributions from different periodic propagation and forcing conditions which contribute to the tidal variability on PW timescales. The formulation of the approach is based on conditional probability formulations of the tidal time series, where the fundamental concept is that the likelihood of occurrence of Y given X is more than the likelihood of Y occurring alone. The information-theoretic measure quantifies information flow between two constituent subsystems (i.e. X & Y samples) of a complex system (i.e. tidal timeseries) (Hlavackova-Schindler et. al., 2007). Kumari & Oberheide (2020) characterized the interannual changes in DE3 (HME1&2) variability on a 10-day PW timescale using this information-theoretic approach. These changes were studied with respect to the interannual modes of atmospheric variability such as QBO, ENSO, and solar cycle. In order to investigate the underlying physical mechanisms, one can investigate interannual variability in the parent waves i.e. DE3 and 10-day PW from SABER observations. This is because DE3-10-day PW nonlinear wave-wave interaction is the main cause of tidal variability on a 10-day PW timescale. This Chapter includes the description of methodology used in Kumari & Oberheide (2020) with the discussion of physical mechanisms responsible for tidal variability on a 10-day timescale.

3.2 Methodology: Information-Theoretic Statistics

The approach is adapted from climate studies, where information theory has been used as a tool to characterize patterns of climate variability and stability in long-term surface temperature records (Knuth et al., 2005; Larson, 2012). The first step is to map the short-term tidal variability timeseries x (i.e. tidal variability on PW timescales) in the normalized probability space. This is to estimate the time-dependent probability density function (TDPDF, $\mathrm{p(x,t)}$) from the given tidal time series x. A probability density function at $\mathrm{t_c}$ (PDF, $\mathrm{p(x, t_c)}$) provides a description of the variability statistics in a sample with a set of data points N centered at $\mathrm{t_c}$. A sample is a subset of the timeseries x and the subsequent (time-shifted) samples are prepared by advancing time steps with increments of one day. A TDPDF is a collection of time-shifted PDFs for each sample of the timeseries. A TDPDF shows how a PDF evolves with time or how variability varies in the probability space. The classical histogram approach is used for a PDF estimation of each sample, where the binning choice is crucially important. A histogram with low bin number fails to capture the essential characteristics of the PDF while a histogram with high bin number leads to random fluctuations between neighboring bins and thus introduces additional variance into the computed estimate. Therefore, it is of important to determine the optimal bin width or number, as the histogram must capture the major features (information) while ignoring fine details (noise). The Bayesian optimum binning scheme was used to get the optimum bin width for each sample which can further be used to get the PDF histogram of the sample, as illustrated in Figure 3.1. The Bayesian optimum binning scheme also provides the equations to estimate the PDF value μ_k and its uncertainty σ_k as a function of bin (once the bin number or bin width is optimized), shown in equation E3.1 and E3.2 respectively (Knuth, 2006).

$$\mu_k = \frac{M}{V}\frac{n_k + \frac{1}{2}}{N + \frac{M}{2}} \qquad [E3.1]$$

$$\sigma_k = \left(\frac{M}{V}\right)^2 \frac{\left(n_k + \frac{1}{2}\right)\left(N - n_k + \frac{M-1}{2}\right)}{\left(N + \frac{M}{2} + 1\right)\left(N + \frac{M}{2}\right)^2} \qquad [E3.2]$$

Here, M= number of bins chosen for the PDF estimation of sample, N=number of days in a sample, V=data range in a sample and, n_k = number of data points in the k^{th} bin, where k runs from 1 to M.

In short, Bayesian probability theory provides an algorithm that computes the posterior probability (equation E3.3) of the number of bins for a given data set (sample) which gives the probability of the hypothesis that may explain the observed data.

$$posterior\ probability\ \propto prior\ probability\ \times likelihood\ function \qquad [E3.3]$$

Here for the posterior probability estimation, the Bayesian principle uses the Dirichlet uniform prior multinomial distribution to evaluate the bin probabilities for the prior knowledge and a piecewise constant PDF with uniform bins to estimate the likelihood function, as detailed by Knuth, (2006). Briefly, the Dirichlet distribution is a generalization of the Beta distribution, which is the conjugate prior for coin flipping and the Multinomial distribution is a generalization of the Binomial distribution. The Dirichlet-multinomial is a multivariate extension of the beta-binomial distribution. As such, the uniform Dirichlet-multinomial distribution can be thought as the distribution of outcomes of n independent trials of a dice with six equally probable sides. Further, the optimum bin number is found by maximizing the logarithm of posterior probability. Briefly, the optimum bin number M^* for a given number of days N (i.e. sample length) is computed by maximizing the logarithm of the posterior probability (as shown in Figure 3.1a) computed for all bin numbers M in the range $[2, N-1]$.

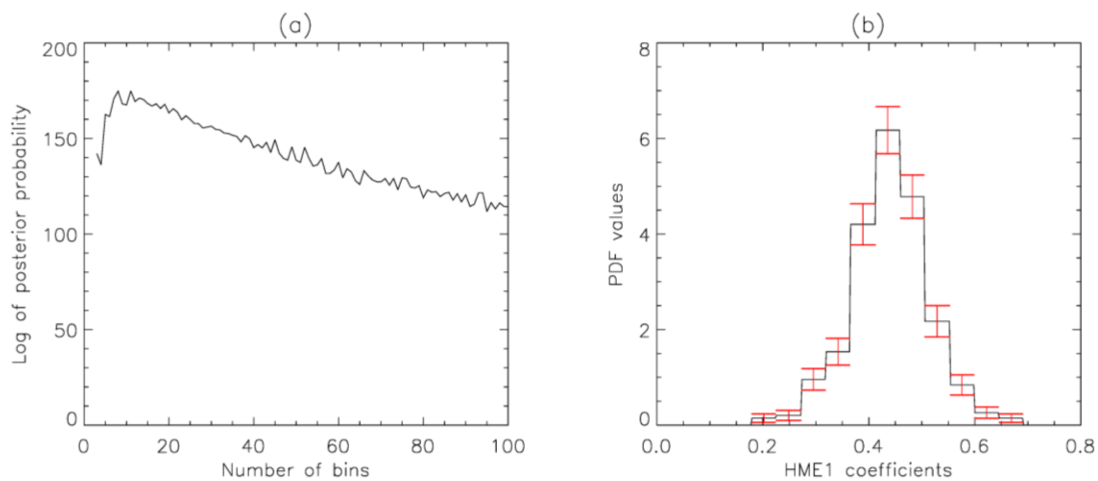

Figure 3.1: (a) Logarithm of posterior probability using equation E3.3 for 3-100 bin numbers (M) for sample at t_c = 3500 and N = 365. The curve maximizes for bin number M^* = 11 and continues to decrease monotonically for bin numbers larger than those included in the plot (b) PDF $p(x, t_c)$ using equation E3.1 and standard deviation (red bars) using equation E3.2. Note that the bin width is ~0.05 and the area under the PDF histogram is normalized to 1. The range of the sample is 0.2-0.7. PDF values, larger than 1, have the bin width less than 1 such that $p(x)dx \leq 1$. (Kumari & Oberheide, 2020)

Figure 3.1a shows the posterior probability maximizing at bin number 11 and Figure 3.1b displays a PDF of a 365-day sample from the (DE3(1)) tidal timeseries with bin number 11. The bin width is determined by dividing the range of variability in the sample (V) by the corresponding bin number (M). Extensive numerical experiments with the SABER data resulted in a value of $N > 150$, enough to avoid small sample sizes in the optimal binning scheme, which is consistent with the general numerical experiments in Knuth (2006). For this study, the sample length N is chosen to be a 365-day window in order to investigate interannual changes of the short-term tidal variability whereas the changes on intraseasonal (i.e. MJO timescale), seasonal and intraannual timescales are smoothed out while computing the PDF for a 365-day sample. It is important to understand that a TDPDF basically represents 'variability over variability', as it can be interpreted as the variability in time-shifted PDFs where PDF is the density distribution of the short-term tidal variability. In this study, the sample length for TDPDF estimation is chosen to be a 365-day window in order to investigate interannual changes of the short-term tidal variability.

Note that a higher range of the tidal variability would require a larger bin number and thus a relatively broader distribution and lower PDF values. A sample with lower bin number corresponding to a smaller range of variability would result in a narrower distribution and higher PDF values. This is important to consider since as the range of time-shifted samples varies, the PDF distribution of the samples also varies. In order to test this further, Figure 3.2 shows TDPDF estimation on short-term variability (<100 days) in F10.7 (solar cycle) indices (shown in Figure 1.5 in Chapter 1) using 365-day samples.

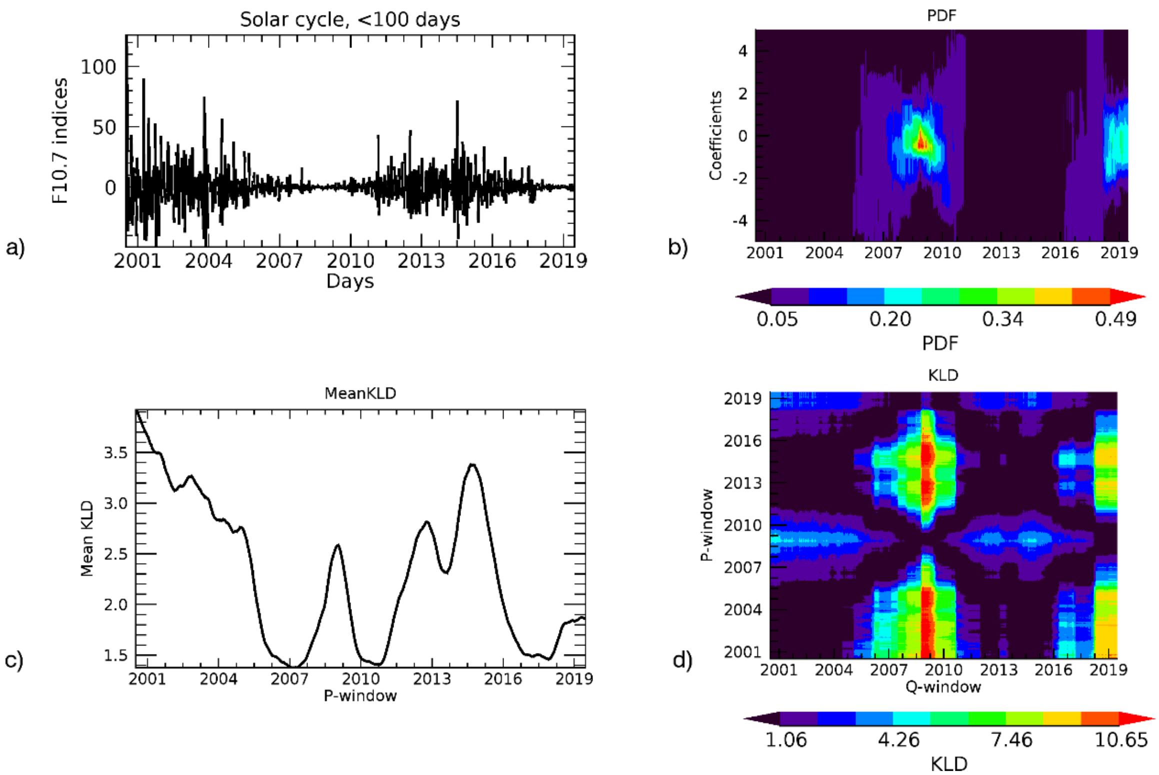

Figure 3.2: a) The (0-100-day) filtered F10.7 indices during 2002-2019, corresponding b) TDPDF using 365-day sampling window, d) KLD, and e) meanKLD timeseries. Large PDF values represent smaller variability in sample. Small PDF values and high KLD values represent large variability.

Figure 3.2a shows the F10.7 short-term variability timeseries and Figure 3.2b shows the corresponding TDPDF estimation. The PDF values corresponding to the samples during 2007-2010 and 2018-2019 are large due to having lower variability as compared to 2002-2006 and 2011-2017, as can clearly be seen in Figure 3.2a. Further, the information-theoretic Kullback-Leibler Divergence (KLD, (Cover & Thomas, 2006)) statistic can be used to quantify the dissimilarity or closeness of two time-shifted PDFs in a TDPDF (Larson, 2010). If $p(x, t_1)$ and $q(x, t_2)$ are two time-shifted PDFs at t_1 & t_2 obtained from two 365-days samples A & B centered at t_1 & t_2, respectively, using the method described above in this section, the KLD provides a measure of the divergence between the PDF for A and B samples, using equation E3.4.

$$D(p\|q) = \sum_{x} p(x, t_1) \log \frac{p(x, t_1)}{q(x, t_2)} \qquad [E3.4]$$

The higher the KLD value, the more $p(x, t_1)$ is structurally divergent from $q(x, t_2)$). A small KLD value for distributions p and q indicates that the PDFs are structurally similar. Therefore, a low KLD value corresponds to time-shifted samples with relatively stable variability while a high KLD value indicates high relative variability between time-shifted samples. It is to be noted that the KLD is not symmetric under the interchange of $p(x, t_1)$ and $q(x, t_2)$, and nonnegative by virtue of the Gibbs inequality. Pattern recognition using KLD values depends on how relative variability distributions of time-shifted samples evolve with time.

The KLD diagnostics of the TDPDF (Figure 3.2b) is shown in Figure 3.2d. The KLD color contours are the divergence of $p(x, t_1)$ from $q(x, t_2)$, with t_1 displayed on the $y-$axis and t_2 on the $x-$axis. Diagonal values in the contour plot are zero as there is no time shift between both PDFs along the diagonal. The non-diagonal values show a distinct pattern of non-zero KLD values that reflect the time evolution (changes) of the PDFs in the TDPDF. Note that there is a sharp transition of high to low and low to high KLD values indicating abrupt changes in short-term F10.7 variability. Intermittent non-diagonal low KLD values indicate low relative variability between the time-shifted $p(x, t_1)$ (window at y-axis) and $q(x, t_2)$ (window at x-axis), or in other words, $p(x, t_1)$ and $q(x, t_2)$ are similar and correspond to similar relative variability in their respective windows. In contrast, high

KLD values indicate high relative variability between $p(x, t_1)$ and $q(x, t_2)$, i.e., those years have a structurally different short-term F10.7 variability.

As discussed above, the range of the tidal variability within a sample window can vary as the sample window advances through the F10.7 time series. In particular, when the sample corresponding to $p(x, t_1)$ has a different range of variability than that of $q(x, t_2)$, it is possible that during KLD diagnostics one may compare null probability bins to finite probability bins. For example, when $p = 0$ and $q \neq 0$, the KLD calculation involves the term $0 \log \frac{0}{q} \approx 0$, causing a loss of information. When $p \neq 0$ and $q = 0$, the KLD calculation features the term $p \log \frac{p}{0}$, an undefined quantity. In order to correct for this in our diagnostics, one can replace null probability bins with bins of small $\boldsymbol{\varepsilon}$ values and then renormalize the distribution to retain the basic property of PDFs. There is no loss of information in KLD diagnostics after this modification. However, when $p \neq 0$ and $q = 0$, then due to the $\boldsymbol{\varepsilon}$ values assigned to zero probability bins, $D(p||q)$ (i.e., $p \log \frac{p}{\varepsilon}$; KLD of the high variability sample p relative to the low variability sample q(~$\boldsymbol{\varepsilon}$)) provides high KLD values, introducing an information bias. This can be clearly seen in the KLD diagnostics (Figure 3.2d) of short-term variability in F10.7 indices. Due to the information bias, in spite of having similar relative variability the KLD values for $p(x, t_1)|_{t_1 = d\{2001-07, 2011-17\}}$ & $q(x, t_2)|_{t_2 = d\{2007-10, 2018-19\}}$ are significantly larger than $p(x, t_1)|_{t_1 = d\{2007-10, 2018-19\}}$ & $q(x, t_2)|_{t_2 = d\{2001-07, 2011-17\}}$. As such, averaging the KLD values over all $q's$ in $D(p||q)$, i.e., the meanKLD (Figure 3.2c) shows a clear distinction between periods/regimes of low and high variabilities. This is to obtain the mean statistical characteristics of the interannual changes in the short-term variability in F10.7 indices, where high meanKLD values represent high relative short-term F10.7 variability, i.e. on timescales of less than 100 days. This method can be validated as the meanKLD value timeseries is similar to how the variances of 365-day samples from the short-term F10.7 timeseries (Figure 3.2a) evolve with time.

Figure 3.2 shows that meanKLD diagnostics clearly identifies the periodicities in the information bias as the recurring events of high variability samples on interannual timescale. This can possibly be studied for any contributions from interannual atmospheric variability modes e.g., QBO, ENSO and solar cycle. In the following, it is shown how the meanKLD diagnostics is used for the retrieval of the statistical characteristics of the interannual variability in the short-term tides on various PW timescales.

3.3 Results: Statistical Characteristics of Short-Term < 30-day Tidal Variability

The baseline dataset used in this analysis is shown in Figure 2.9, on which the information theoretic statistics is applied to retrieve statistical characteristics of short-term tidal variability on a day-to-day timescale. From Table 3.1, the variance of the 0-30 days bandpass filtered equatorial/symmetric mode DW1(1) variability (Figure 2.9a; Chapter 2) constitutes ~18% of the total HME1 variance (Figure 2.8a; Chapter 2). The bandpass filtering of DE3(1) (Figure 2.9d; Chapter 2) and DE3(2) (Figure 2.9f; Chapter 2) on 0-30 days shows 53% and 64% variance of total, respectively. As explained in section 3.2, an $N = 365$ day sampling window length can be used to select all the samples from the bandpass-filtered tidal timeseries. For each sample, a PDF estimation (histogram model) is carried out from the Bayesian statistics using equations E3.1 and E3.2, as explained above.

As samples have been created by advancing the time step by one day at a time, they collectively provide a TDPDF estimation, i.e. how PDFs of the variability in samples evolve with time.

Table 3.1: The percentage of total variance in the three tidal timeseries on 5-day, 10-day, 16-day and 23-day timescales, which explain 50% of the percent variance on <30-day timescale.

Bandpass filtering of the tidal modes on different PW timescales /Variance of the filtered data in %	DW1(1)	DE3(1)	DE3(2)
4-7 (5-day)	3.43	12.44	14.68
8-14 (10-day)	3.43	9.44	11.71
15-19 (16-day)	1.71	2.29	3.74
20-25 (23-day)	1.19	2.33	3.12
0-30 (<30-day)	18.05	53.18	63.66

Figure 3.3a-c shows the TDPDF estimation of the variations in <30-day bandpass filtered DW1(1) and DE3(1&2) tidal timeseries using the samples of a year's length from the three filtered HME timeseries (i.e. Figures 2.9a, 2.9c, 2.9e, Chapter 2). The PDF values in TDPDFs generally exceed 1 if the bin width is <1. The TDPDF shows a more complex structure than in Figure 3.2b (solar cycle short-term variability). Subsequently, the KLD values (calculated using equation E3.4, shown in Figure 3.3d-f) for all the three tidal timeseries have complex structure with respect to Figure 3.2c and the meanKLD (averaged KLD along x-axis, shown in Figure 3.3g-i, black lines) timeseries have several regions of

high variability regimes. They represent the mean statistical interannual characteristics of the short-term (<30 days) tidal variability. The red dotted lines represent the statistical error of the meanKLD values up to one standard deviation, which does not exceed 10%.

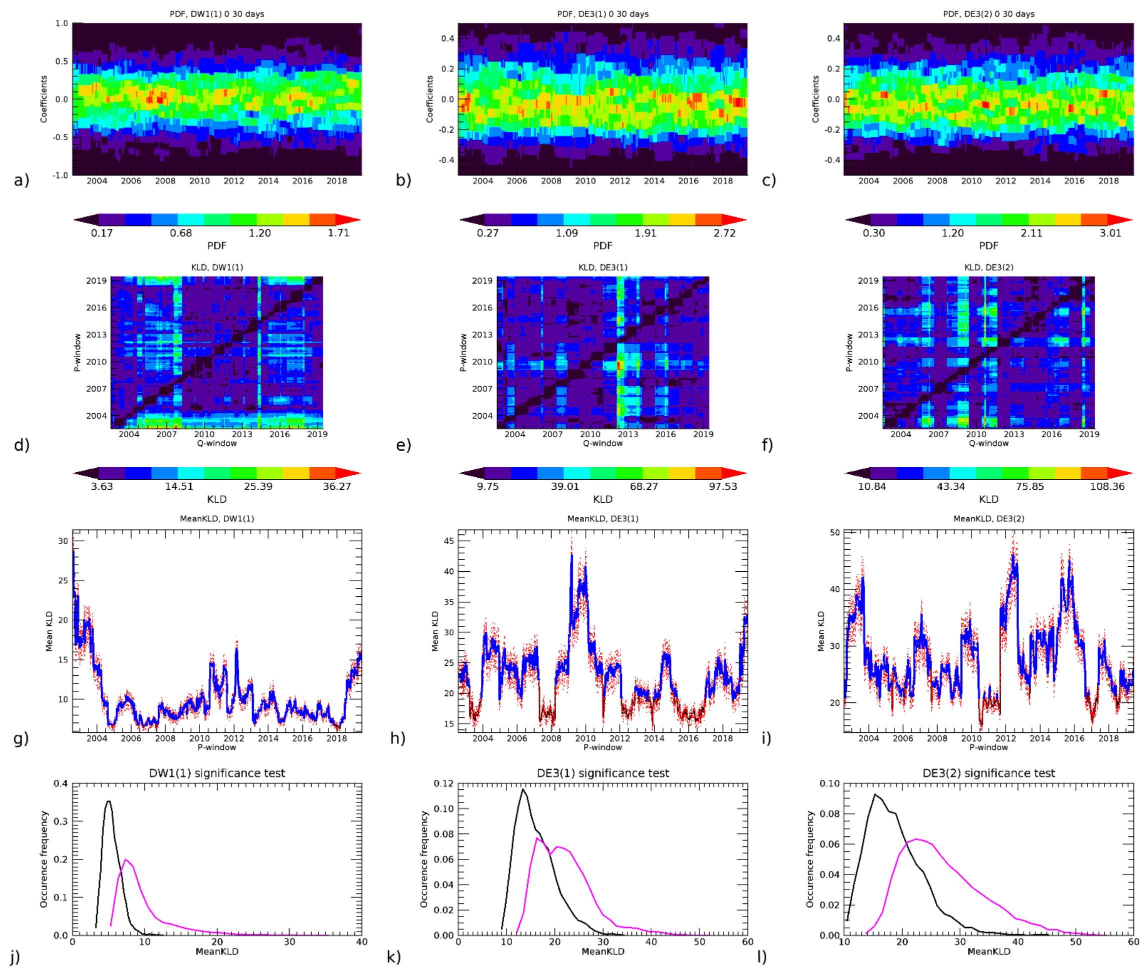

Figure 3.3: (a,b,c) TDPDF $(p(x,t))$, (d,e,f) KLD, and (g,h,i) meanKLD for sampling window 365-day from 0-30 days filtered DW1(HME1), DE3(HME1), and DE3(HME2) timeseries. The statistical significance test is shown in (j,k,l), respectively. The pink and black curves in (j,k,l) correspond to the occurrence frequency for each meanKLD value of tidal timeseries and its noisy counterpart. The values at which the pink curve is above the black curve or the meanKLD values which are statistically significant are shown as blue colors in (g,h,i) (overlapped on black and red curves). The red colors represent the statistical error of the meanKLD values up to one standard deviation.

Note that the timeseries shown in Figure 2.9 in Chapter 2 looks more complex than the timeseries shown in Figure 3.2a above. A study with short-term tidal timeseries on various PW timescales from SABER requires error estimation and statistical significance test of meanKLD values as there is ~1K error associated with the HME coefficients after tidal deconvolution and HME fits.

3.3.1 Error Estimation and Statistical Significance Test

The error of the meanKLD values has been calculated by propagating the PDF uncertainties (red bars in Figure 3.1b) of each bin to the meanKLD computations. This is done by 50 Monte Carlo simulations. For the statistical significance test, it is important to understand that any two non-identical PDFs will yield a positive KLD value, due to its mathematical properties. The statistical significance test of the meanKLD values is carried out by randomly shuffling the tidal timeseries to create 50 noisy timeseries and the meanKLDs are calculated for each noisy timeseries. This is to produce variabilities of similar magnitude but with no underlying physics. The distribution of occurrence frequency of each meanKLD values of the tidal timeseries (before shuffling) are compared with the distribution of meanKLD values of the noisy counterparts (after shuffling). Both distributions will have right tails, as KLD values cannot be negative. Therefore, one cannot assume a Gaussian distribution for noisy mean KLD values and quantifying the significance level corresponding to a p-value does not apply for the test. The meanKLD values at which the occurrence frequency is larger than its noisy counterparts are considered as statistically significant. This helps to understand whether meanKLD timeseries (e.g., Figure 3.2c) can be used for further analysis of underlying physical processes.

The statistical significance test is shown in Figure 3.3j-l for each of the tidal (bandpass filtered HME) timeseries which shows the occurrence frequency of each meanKLD values for (pink) tidal HMEs timeseries against their (black) noisy counterparts. The large mean KLD values are also present in noisy meanKLD timeseries (black line in Figure 3.3j-l). They can arise when two (time shifted 365-day) noisy samples have different ranges (different means of the sample distributions). Two samples from noisy timeseries can have different ranges as distributions using 365 data points cannot be true Gaussian distributions with similar means and standard deviations. All three distributions in Figure 3.3j-l have right tails, as KLD values cannot be negative. If the occurrence frequency of meanKLD values is higher than its noisy counterparts, such values are considered to be statistically significant meanKLD values. As such the blue lines in Figure 3.3g-i (overlapped at black lines) show the statistically significant meanKLD values against the meanKLD timeseries (black curve). The non-significant meanKLD values in percentage is tabulated in Table 3.2, which is less than ~20% for all tidal modes which is why the meanKLD values $p(x, t_1)|_{t_1=d\{2002-2019\}}$ in Figure 3.3g-i can be used as the statistical measure for the interannual variability characteristics of the short-term tidal variability on timescales of less than a month.

As discussed above, as the baseline timeseries (Figure 2.9) looks complex, the corresponding KLD values look complex in Figure 3.3d-f. In other words, the recurring patterns are not so distinguishable in the KLDs. This is because the variability on each PW timescale is not resolved in the KLD contour plots. Next, it is important to resolve tidal variability on various PW timescales by bandpass filtering at PW normal mode timescales (e.g., 5-day, 10-day, 16-day, 23-day).

Table 3.2: The percent of non-significant values in the meanKLD timeseries of each of the tidal timeseries on <30 day, 5-day, and 10-day timescales.

Non-significant meanKLD values (%)	DW1(1)	DE3(1)	DE3(2)
0-30 day	4	18	11
4-7 day	1	2	4
8-14 day	0	17	23

Due to atmospheric manifestations of normal modes, the observed variability of these wave periods in the atmosphere are often referred to, respectively, as the quasi-5-day wave (Q5DW), quasi-10-day wave (Q10DW), quasi-16-day wave (Q16DW), and quasi-23-day (Q23DW). The filter width (4-7, 8-14, 15-19, and 20-25 days) around each of the normal mode frequencies is chosen to cover the band of frequencies around each normal mode. Based on the tabulated percent variance of tidal timeseries on PW timescales in Table 3.1, the tidal variability on 5-day and 10-day timescales are important to explain most of the diurnal tidal variability on PW timescales. The variability on 16-day and 23-day timescales contains less than 5% of the total variance. In the remainder of the thesis, the focus is on short-term tidal variability on a Q5DW and Q10DW timescale with a bandpass filter width of 4-7 and 8-14 days, respectively. As such, KLD diagnostics is performed for the tidal variability on a Q5DW and Q10DW timescales whereas the DE3 tidal variability on a Q10DW timescale is explained in detail in Kumari & Oberheide (2020).

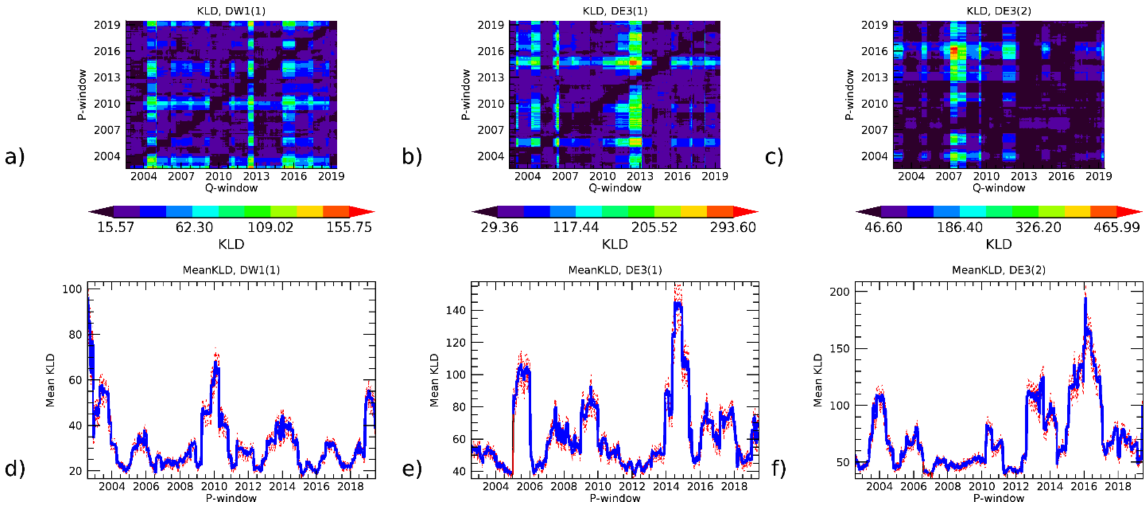

Figure 3.4: (a,b,c) KLD and (d,e,f) meanKLD for three tidal timeseries on a 5-day timescale.

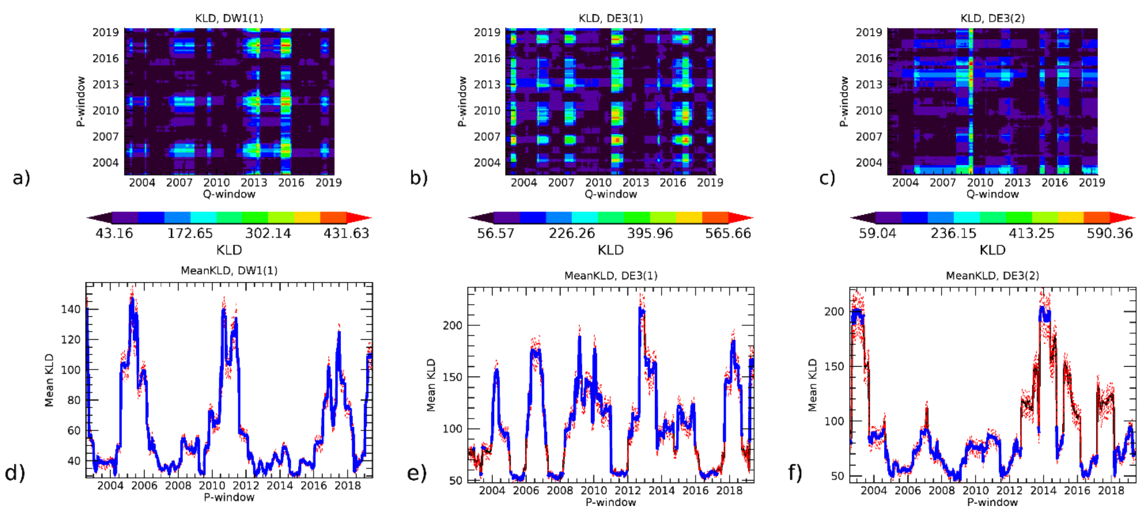

Figure 3.5: Same as Figure 3.4, but for tidal timeseries on a 10-day timescale.

The pattern disgnostic using KLDs is better resolved in Figures 3.4 and 3.5 than in Figure 3.3, in particular for the tidal variability on a 10-day timescale in Figure 3.5. With numerical experiments, it was found that our results are not sensitive to bin numbers within a certain range (neither too low nor too high) for SABER tidal timeseries. In order to save computational time, the meanKLD analysis in Figure 3.5 uses the constant bin number 21 for the PDF estimation of each sample. This is allowed as the results shown in Figure 3.5 are not sensitive to the bin numbers within a certain range. This can be verified by comparing the meanKLD values in Figures 3.5b and 3.5c with that of DE3 on a Q10DW timescale shown in Kumari & Oberheide, (2020) which used variable bin numbers for samples using Bayesian optimal binning scheme.

Interestingly, the meanKLD timeseries for tidal variability on 5-day timescale has interannual characteristics distinctly different from those of the meanKLD timeseries for the variability on 10-day timescale. On another note, meanKLD values for the variability on 5-day timescale do not have periodic regimes of high variability in a distinct manner as their counterpart for 10-day timescale. The meanKLDs of the DW1(1) variability on 10-day timescale have 4-6-year recurring regimes of high variability, while those of DE3(1) and DE3(2) show 2-3-year and 11-year periodic characteristics, respectively, whereas the meanKLD values for 5-day timescale show somewhat mixed periodic variations ranging from 2-3 year to 11-year. This is particularly interesting as it points to how DW1 and DE3 tidal variability for each PW timescale is unique, which motivates the further study of underlying physical mechanisms. The goal is to investigate the causes of such periodic high variability regimes or under which conditions the short-term tidal variability becomes large.

Table 3.2 shows the percentage of non-significant meanKLD values for each of the analyses. Though DW1(1) variability on different PW timescales is smaller than that of the DE3 tides, the non-significant meanKLD values are less for DW1 (<5%) than for DE3 (<25%). Since both high and low KLD values are significant as can be seen in Figure 3.4d-f and 3.5d-f plotted as blue colors overlapped on the black curve (i.e., meanKLD timeseries), the meanKLD values for both PW timescales are further used for understanding what causes such high variability regimes in the interannual characteristics of diurnal (DW1(1) and DE3(1&2)) tidal variability on a Q5DW and a Q10DW timescale. Finally, to delineate the causal relationship between relatively high interannual variability events and stratospheric QBO at 50 hPa, ENSO from Oceanic Niño Index (ONI) index, and solar radio 10.7 cm flux (F10.7) index (shown in Figure 1.5; Chapter 1), one can perform a multiple linear regression fit on the mean KLD values $\mathrm{Y(t)}$ using the following model:

$$\mathrm{Y(t)} = \mathrm{A_0} + \mathrm{A_1} \times \mathrm{QBO_{50hpa}}\left(\mathrm{t} - \mathrm{t_{QBO}}\right) + \mathrm{A_2} \times \mathrm{ENSO}(\mathrm{t} - \mathrm{t_{ENSO}}) + \mathrm{A_3} \times \mathrm{F10.7}(\mathrm{t} - \mathrm{t_{solar}}) \qquad [E3.5]$$

Here, $\mathrm{A_0}, \mathrm{A_1}, \mathrm{A_2}$, and $\mathrm{A_3}$ are the regression coefficients and $\mathrm{t_{QBO}}$, $\mathrm{t_{ENSO}}$, and $\mathrm{t_{solar}}$ are the lag parameters with respect to the timeseries of mean KLD values. The lag parameters are optimized for the best regression fit (i.e., corresponding to maximum linear regression coefficient (R_M) and linear correlation coefficients R_{QBO}, R_{ENSO} & $R_{F10.7}$) by advancing the mean KLD timeseries a time step interval of a day in the left direction (until

01/01/2001) with respect to QBO and ENSO indices. The best regression fits are shown as the green curves in Figure 3.6 for the three tidal modes on Q5DW and Q10DW timescales, where the weight parameter of each mean KLD value for the regression is inversely proportional to its standard deviation (uncertainty, shown as red in Figure 3.6).

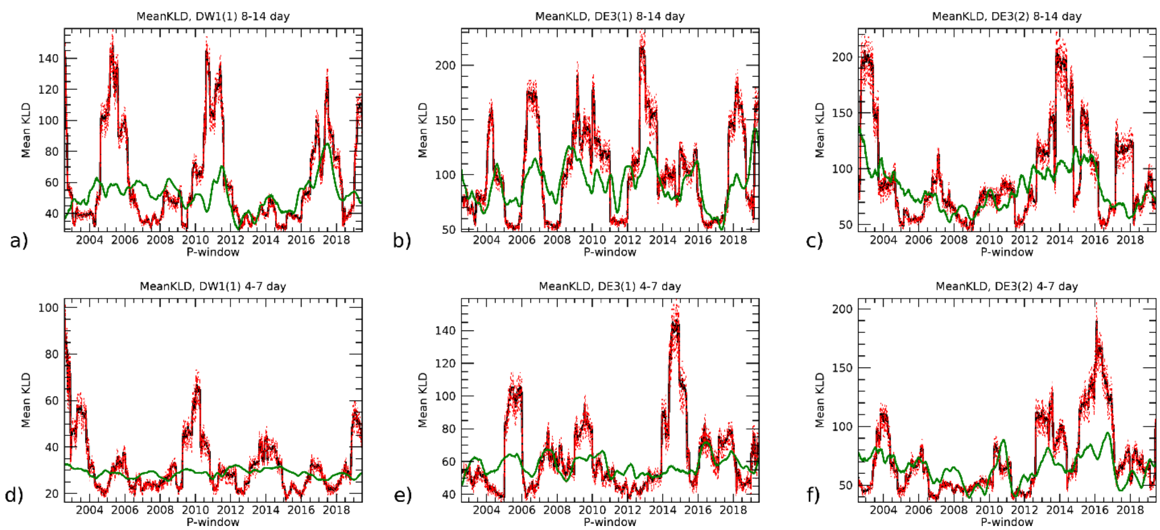

Figure 3.6: The black curves indicate the meanKLD timeseries of the three tidal modes on a (a,b,c) Q10DW and (d,e,f) Q5DW timescale. The red colors represent the uncertainties of meanKLD values up to one standard deviation. The green curve in each plot represents the best regression fit (using equation E3.5) of meanKLD values.

The best regression fits (R_M>~0.5) are obtained in the case of tidal variability on Q10DW timescale especially for HMEs of DE3 tides, as can be seen in Figure 3.6b and 3.6c with green curves. A regression correlation coefficient R_M of greater than 0.5 means that 50% of the variability in meanKLD timeseries can be explained by the combined effects of QBO, ENSO and the solar cycle. Table 3.3 shows correlation coefficients for DE3 HME1&2 tidal variability on a Q10DW timescale with respect to QBO (R_{QBO}), ENSO (R_{ENSO}), and solar cycle ($R_{F10.7}$) along with their lag values (t_{QBO}, t_{ENSO}, & $t_{F10.7}$; days for the best fit) and normalized fit coefficients with respect to their standard deviations. The lag with solar cycle timeseries is taken to be zero.

Table 3.3: Normalized fit coefficients (from the study of the DE3-10-day PW interactions) with respect to their standard deviations and the corresponding linear correlation coefficients from regression analysis on normalized (i.e. relative to the maximum) mean KLDs. Each fit coefficient is normalized to its standard deviation and the magnitude of normalized fit coefficients must be >1.96 to ensure a significance of over 95% based on student's t-test. The significant fit coefficients are marked as *.

	Normalized fit Coefficients\ Linear Regression Coefficient	QBO\ R_{QBO}	ENSO\ R_{ENSO}	F10.7\ $R_{F10.7}$
1.	HME1 on Q10DW timescale	-2.10*\-0.32	-1.97*\-0.24	-0.45\0.00
2.	HME2 on Q10DW timescale	-0.52\0.00	0.97\0.17	2.22*\0.49
3.	Q10DW in NH	3.33*\0.26	2.72*\0.17	-3.84*\-0.26
4.	Q10DW in SH	-2.96*\-0.11	4.56*\0.44	2.36*\0.31

The results of regression analysis for tidal variability on 5-day timescale are not shown in Table 3.3, as the multiple linear regression coefficient (R_M) values were on the order of ~0.3 which shows that the regression model with QBO, ENSO, and solar cycle cannot explain at least 70% of the interannual characteristics of tidal variability on 5-day timescale. This results in smaller fitting coefficients which may lead to unreliable physical interpretations. A similar scenario (R_M <0.5) was found for the regression analysis of DW1(1) on 10-day timescale. Nonetheless, the R_M value for DE3(1&2) tidal variability on 10-day timescale was found to be above 0.5, which is why the regression fit coefficients for DE3 on 10-day timescale are used for further interpretations. The multiple linear regression coefficient (R_M) for DE3(1) on 10-day timescale is 0.51 for a QBO lag of t_{QBO} ~ 7 months with corresponding linear correlation coefficient (R_{QBO}) ~ -0.32 and an ENSO lag (t_{ENSO}) of ~1 year with R_{ENSO} ~ -0.24, also summarized in Table 3.3 including the normalized fit coefficients with respect to their standard deviations. No solar cycle response is found. The mean KLD values of DE3(2) on a Q10DW timescale (black curve in Figure 3.5f) show a prominent 11-year pattern. The regression analysis (blue curve in Figure 3.8b) yields R_M ~ 0.54, which is predominantly due to solar cycle F10.7 variability (of zero lag and $R_{F10.7}$ ~ 0.49). Here, the positive sign in $R_{F10.7}$ indicates that the high variability regimes correlate with solar maximum conditions. There is no significant response to the QBO and ENSO for this mode. A negative sign in R_{QBO} means that the high variability regimes correlate with the easterly(westward) phase of the stratospheric QBO winds, while a positive sign represents high variability when westerly(eastward) QBO is present. Similarly, a negative sign in R_{ENSO} means a correlation with the cold or La Niña phase of ENSO and a positive sign means correlation with the warm or El Nino phase of ENSO. The uncertainty of the lag values is about 1-2 months using Monte Carlo simulations (with respect to meanKLD values and their uncertainties) with 100 iterations. However, the regression coefficients marked as * in Table 3.3 are statistically significant at the 95% level using Student's t-test. The fitting values of regression analysis in Figure 3.6b and 3.6c show how tidal variability on a Q10DW timescale is modulated by the QBO, ENSO and the solar cycle, with quite different responses in the symmetric HME1 and antisymmetric HME2 modes of DE3. Overall, short-term DE3 tidal variability on a

Q10DW timescale in the symmetric (HME1) and antisymmetric (HME2) modes of DE3 exhibit a very different interannual variability, which underlines the importance of diagnosing both modes separately.

As mentioned in section 3.1, F10.7, ENSO and QBO may in principle interact to produce atmospheric variability. The general linear regression model allows one for the incorporation of interaction effects between two predictor variables such as QBO*ENSO, F10.7*QBO and F10.7*ENSO. Therefore, the interaction effects can be investigated in the mean KLDs by adding each of the interaction terms individually to the regression model, such as $\mathrm{Y(t)} = \mathrm{A_0} + \mathrm{A_1} \times \mathrm{QBO_{50hpa}}(\mathrm{t} - \mathrm{t_{QBO}}) + \mathrm{A_2} \times \mathrm{ENSO}(\mathrm{t} - \mathrm{t_{ENSO}}) + \mathrm{A_3} \times \mathrm{F10.7}(\mathrm{t} - \mathrm{t_{solar}}) + \mathrm{A_4} \times \mathrm{QBO_{50hpa}}(\mathrm{t} - \mathrm{t_{QBO}}) * \mathrm{ENSO}(\mathrm{t} - \mathrm{t_{ENSO}})$, and so on. None of the interaction term coefficients are statistically significant in the regression fittings based on the student's t-test, as shown in Table 2 in Kumari & Oberheide (2020) (not shown here). Including all the three interaction terms in the regression model does not give any significant fit coefficients for interaction terms. As such, the inclusion of interaction terms in the multiple linear regression does not provide a better model to explain the statistical characteristics of the short-term variability in either mode. For an additional reference, a linear regression with the timeseries of either QBO or ENSO indices alone to DE3(HME1) mean KLD values does not yield coefficients of statistical significance, whereas the multiple linear regression with both QBO and ENSO in HME1 yields coefficients with a significance above the 95% threshold. This indicates that ENSO is evident and necessary along with QBO to explain the statistical characteristics of HME1 variability on a Q10DW timescale, while QBO or ENSO alone cannot do so.

The causes of such response due to QBO, ENSO and solar cycle in DE3 HME1&2 variability on a Q10DW timescale are studied in Kumari & Oberheide (2020) using the aforementioned meanKLD diagnostics. The following text is from Kumari & Oberheide (2020), which explains how DE3 and Q10DW waves after nonlinear wave-wave interactions modulate the DE3 variability on a Q10DW timescale in HME1 and HME2 modes as a function of QBO, ENSO, and solar cycle. The idea is to focus on the latitude/altitude overlap of parent/primary waves, i.e., DE3 and Q10DW, which is required for the interaction to take place. Also, one needs to understand how such nonlinear interactions over time result in tidal variability on a Q10DW timescale as a function of QBO, ENSO and/or solar cycle.

3.4 Causes of Tidal Variability on a 10-day PW Timescale

The latitudinal symmetry of DE3 amplitudes in the summer-winter season has been discussed in Chapter 1. A closer examination of the Q10DW seasonal variation and latitudinal symmetry is also important in understanding whether the interannual signals are caused in short-term DE3 variability (on Q10DW timescale) by a modulation of the DE3 or the Q10DW. Figures 3.7-3.10 show derived averaged Q10DW amplitudes from 2002-2018 from SABER, using the least-squares fit methodology discussed in detail by Kumari & Oberheide (2020). Basically, the diagnostic follows the approach of Forbes & Zhang (2015) where Q10DW of westward zonal wavenumber 1 is fitted on SABER observations with a sliding window of length three times the wave period (10 days).

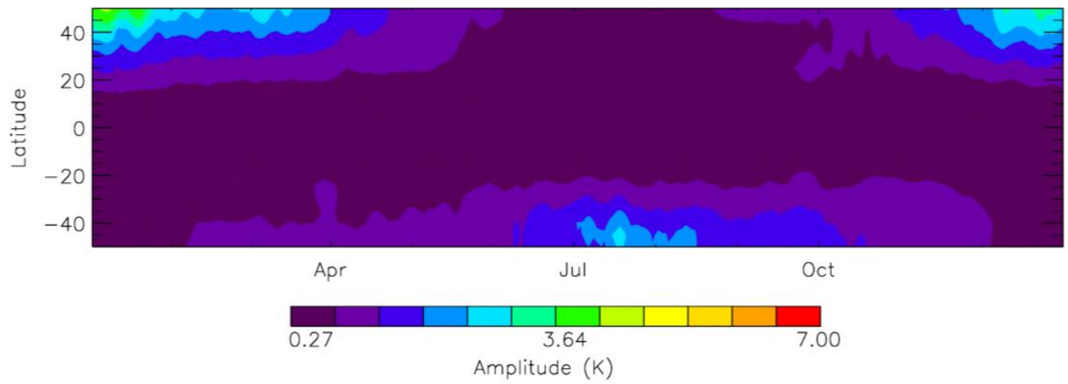

Figure 3.7: SABER Q10DW amplitudes averaged over 2002-2018 at 40 km altitude.

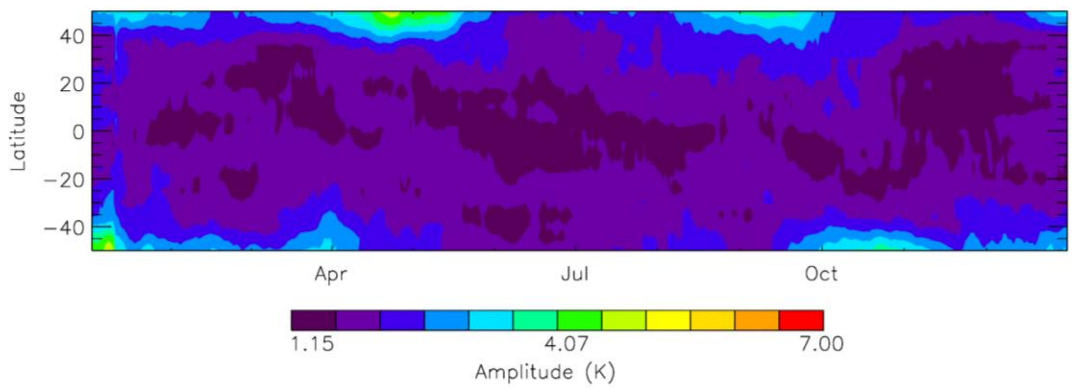

Figure 3.8: Same a Figure 3.7, but at 100 km altitude.

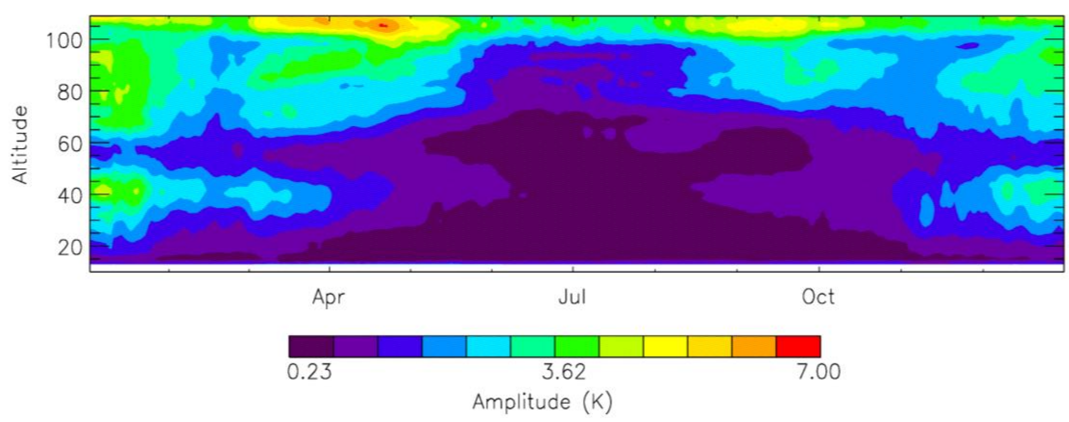

Figure 3.9: SABER Q10DW amplitudes averaged over 2002-2018 at 50º N latitude.

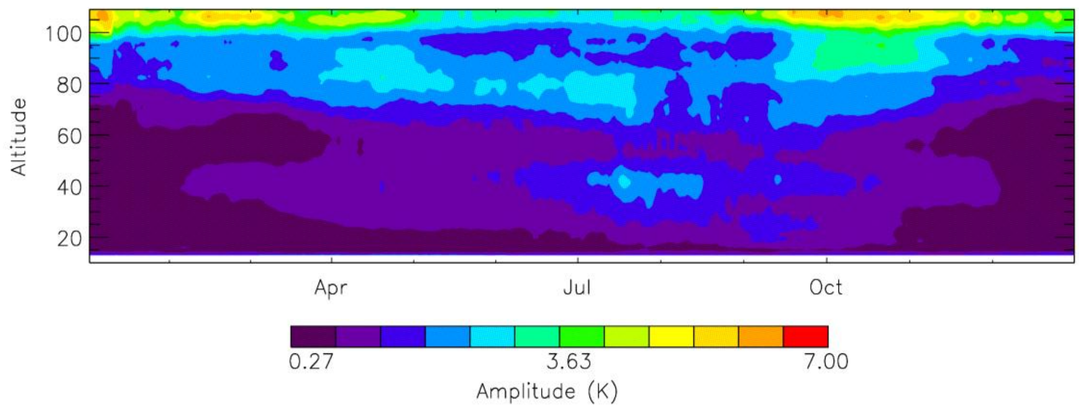

Figure 3.10: SABER Q10DW amplitudes averaged over 2002-2018 at 50° S latitude.

The Q10DW amplitudes in the stratosphere/lower mesosphere, also known as the (1,2) normal mode, maximizes in mid-high latitudes in the winter hemisphere (as seen in Figure 3.7) and its phase (not shown) is antisymmetric with respect to the equator. There is sufficient altitude/latitude overlap between DE3 HME1&2 modes and Q10DW. DE3 HME1 as the symmetric mode extends from the tropics to mid-latitudes prevailing in NH summer and can overlap with Q10DW amplitudes in the SH winter (June-September; Figure 3.10). As such, DE3 HME2 as antisymmetric mode prevailing in NH winter can overlap with Q10DW maximizing during NH winter (December-March; Figure 3.9). A nonlinear interaction between the DE3 and the 10-day PW (or Q10DW) generates two nonmigrating child waves DE4 and DE2 (with periods of ~27 hours and ~22 hours i.e. $f_{PW} \pm f_{tide}$) and as a result of child waves and DE3 interaction the DE3 is modulated on a Q10DW timescale. Note that Figure 3.8 shows an increase in equatorward Q10DW activity at 100 km as compared to at 40 km in Figure 3.7. During sudden stratospheric warming events (SSWs), Sassi & Liu (2014) reported that westward planetary waves propagate equatorward where they couple with tides. Thus, in addition to nonlinear wave-wave interaction due to altitude/latitude overlap, the increasing equatorward variability of the Q10DW above 40 km can also contribute to the DE3(1) and DE3(2) response in tidal variability on a Q10DW timescale. As a means of comparison, a KLD diagnostics is performed to study the interannual variations of the Q10DW during 2002-2018. Figures 3.11 and 3.12 show the results at 60 km and the latitude band (35^o-55^o N/S).

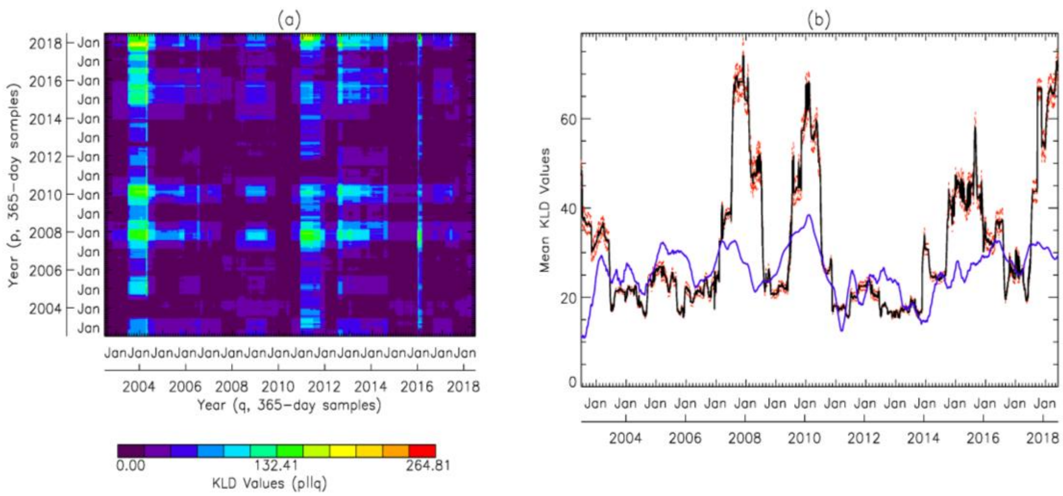

Figure 3.11: a) KLD diagnostics for monthly mean Q10DW amplitudes from SABER at 60 km altitude and averaged latitudes (35^o N-55^o N). b) Mean KLD values (black) of interannual variability in Q10DW with their uncertainty (red) and the regression fit (blue).

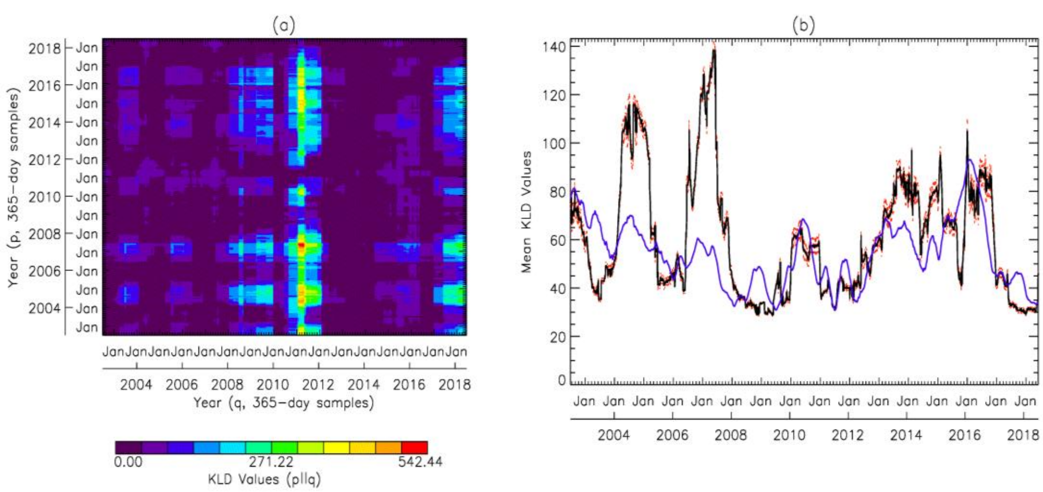

Figure 3.12: Same as Figure 3.11, but for SH.

All meanKLD values (i.e., black curves in Figures 3.11b and 3.12b) are statistically significant and the regression analysis (shown as blue curves) gives further insight into the response of the Q10DW interannual variations to QBO, ENSO and solar cycle. The results of the regression fits for the variations in the NH and the SH are part of Table 3.3. The lag to QBO ($\mathrm{t_{QBO}}$) is 9 months for both hemispheres and the lag to ENSO ($\mathrm{t_{ENSO}}$) is 2 months in the NH, and 6 months in the SH. R_{QBO} and $R_{F10.7}$ (Table 3.3) have opposite signs in both hemispheres while $\mathrm{t_{QBO}}$ is similar in both hemispheres. The uncertainty of the lag values is about 2 months. Next, the causes of the DE3(1&2) variability on Q10DW timescale is discussed in the following with the help of the regression results on the meanKLD diagnostics of the monthly mean Q10DW amplitudes.

3.4.1 DE3 Tidal Variability on a 10-day Timescale: Response to QBO

The negative sign in R_{QBO} means that the high variability regimes in meanKLD timeseries for DE3(1) mode overlap with the easterly phase of QBO winds in stratosphere. In other words, the easterly phase of QBO is responsible for the enhanced interannual variability in the DE3(1) tidal variability on a Q10DW timescale (Figure 3.6b). However, there is no response to QBO in DE3(2) variability on a Q10DW timescale (Figure 3.6c). The large response of the interannual DE3(1) variability on a Q10DW timescale with respect to the easterly phase of the QBO or easterly QBO can, in principle, arise from either the interaction of the Q10DW with QBO-modulated DE3 variability or DE3 interaction with a QBO-modulated Q10DW. Regarding the first hypothesis, Oberheide et al. (2009) showed that DE3(1) monthly mean amplitudes are ~20% larger during the westerly phase of the stratospheric QBO compared to the easterly phase. This has been explained using the Doppler shift towards higher frequency of eastward propagating tides (e.g., DE3) for easterly QBO winds in the mesosphere (which correspond to westerly stratospheric QBO winds), causing reduced dissipation in the mesosphere (Ekanayake et al., 1997). It is, therefore, unlikely that the observed larger variability during the easterly QBO comes from QBO-modulated DE3(1) variability. On the other hand, the regression on meanKLD diagnostics of the SABER Q10DW (Figures 3.11b and 3.12b; and corresponding Table 3.3) shows a response to the westerly QBO (positive correlation) in the NH and to the easterly QBO (negative correlation) in the SH, opposite to each other. As such, the tidal variability in the HME1 mode of DE3 should be large during the easterly QBO since DE3(1) interacts largely with the Q10DW in the SH winter, as explained above. This is consistent with Table 3.3 results for DE3(1) and supports the hypothesis that a QBO-modulated Q10DW is responsible for the enhanced DE3 HME1 variability on a Q10DW timescale.

Note that additional contributions may come from a direct QBO modulation of the symmetric Q10DW contribution at low latitudes, that is, due to the deviation from the (1,2) normal mode above 40 km altitude. Contributions to the Q10DW modulation of HME1 in DE3 during NH winter, on the other hand, are comparatively small, due to the small HME1 amplitudes in NH winter. Not much work has been done on investigating what causes a QBO modulation of the Q10DW. A QBO modulation of Q10DW has previously been reported by Lu et al. (2012) and Forbes & Zhang (2015) but they do not explain the underlying physical mechanisms. However, the data allow us to estimate where the

Q10DW-DE3(1) interaction takes place. Possible QBO effects on the Q10DW can be imposed anywhere in the stratosphere and mesosphere. The lag between the meanKLD and the QBO contribution (~ 7 months from easterly QBO) in the DE3(1) regression analysis helps to narrow the height at which the interaction of the DE3 and Q10DW may have occurred. Note that the lag value is consistent with that of Q10DW in the SH (i.e. ~9 months). Since the QBO in the mesosphere is out-of-phase to the QBO in the stratosphere (lag of 12-14 months), this indicates from a linear analysis of height vs phase that DE3 tides and Q10DW likely interacted between 50-70 km, i.e. the mesosphere.

DE3(2) variability on a Q10DW timescale, on the other hand, does not show a QBO signal (Figure 3.6c). This is surprising because DE3(2) has a sufficient latitude/altitude overlap with the Q10DW in NH winter and one should therefore expect enhanced DE3(2) variability during the westerly QBO because of the enhanced Q10DW. At present, the missing QBO signal in DE3(2) is not understood. One can only speculate that the large solar cycle signal in DE3(2) masks the QBO effect or the transient events (section 3.4.3) play a role.

3.4.2 DE3 Tidal Variability on a 10-day Timescale: Response to ENSO

Warner & Oberheide, (2014) found enhanced DE3 tides in both HME1 and HME2 modes during the 2010/11 La Niña (cold pacific) phase due to enhanced tidal forcing and a negligible response during the El Niño (warm pacific) phase. As such, the short-term DE3 response to ENSO must also be investigated with regard to the two hypotheses, on whether the variability corresponding to ENSO arises from the Q10DW or the DE3 tide itself. As established earlier, the interaction of Q10DW with the DE3(2) mode is more likely to occur in the NH wintertime while the interaction with the DE3(1) mode is more likely to occur in the SH winter. The DE3(1) regression analysis shows a negative correlation with ENSO (Figure 3.6b; corresponding R_{ENSO} in Table 3.3) which means that the interannual variability in DE3(1) on a Q10DW timescale is correlated with the cold or La Niña phase of ENSO. In contrast, the variability in DE3(2) (Figure 3.6c; Table 3.3) does not show any statistically significant correlation with ENSO.

The enhanced DE3(1) tidal variability during the La Niña phase is more likely caused by enhanced convective DE3 forcing as the KLD diagnostics of the Q10DW (Figures 3.11 and 3.12) indicates that the Q10DW interannual variability in both hemispheres largely responds to the warm or El Niño phase of ENSO (i.e. the linear regression correlation coefficients R_{ENSO} are positive). A lag of 1 year for DE3(1) with ENSO in the regression analysis of mean KLDs does not imply that the short-time DE3 variability retains a memory of several months to > 1-year in response to ENSO. It reflects the fact that the high-variability regime in DE3(1) responds to the La Niña phase of ENSO, which is consistent with the effect from the monthly DE3 due to enhanced convective forcing. Likewise, the high variability regime in Q10DW mean KLD diagnostics responds to the El Niño conditions. This is consistent with Garcia-Herrera et al. (2006) who reported that the westward planetary waves activity at NH middle latitudes is enhanced during El Niño events in NH winter. If the DE3(1) on a Q10DW timescale were to respond to the El Niño phase of ENSO, the interpretation for the causal mechanism would have been enhanced activity in the interacting Q10DW. Further, as mentioned above, the regression analysis of DE3(1) does not provide a significant fit coefficient for the interaction term QBO*ENSO. This is possibly because the QBO modulation in DE3(1) on a Q10DW timescale originates from the interacting QBO-modulated Q10DW in SH winter while ENSO modulation originates from the enhanced DE3(1) tidal variability during the La Niña phase.

3.4.3 DE3 Tidal Variability on a 10-day Timescale: Response to Solar Cycle

The solar cycle dominates the DE3 HME2 variability response (Figure 3.6c) but the DE3(1) mode variability lacks any response to the solar cycle (Figure 3.6b). See also Table 3.3. It is unlikely that this behavior comes from a DE3 solar cycle dependence. As the large DE3(2) mode in NH winter is predominantly caused by mode coupling with the DE3(1) mode, solar cycle variations in the mean winds would thus impact both modes and not only DE3(2). A solar cycle signal in DE3 amplitudes in the MLT region has not been reported yet. The solar cycle modulation of DE3(2) must thus come from the Q10DW through a mechanism that explains why the negative F10.7-Q10DW correlation in the NH (where the coupling with Q10DW-DE3(2) takes place) causes a positive F10.7-DE3(2) correlation (Table 3.3) and why the positive F10.7-Q10DW correlation in the SH (where the coupling with F10.7-DE3(1) takes place) does not cause a HME1 response. The solar cycle dependence of traveling planetary waves is a comparatively understudied field, mainly due to the challenge of obtaining homogeneous measurements on decadal time scales. The positive correlation of F10.7-DE3(2) on a Q10DW timescale and negative correlation of F10.7-Q10DW in the NH (Table 3.3) suggest that a direct modulation by the Q10DW cannot explain the DE3(2) solar cycle signal shown in Figure 3.6c. This indicates that the solar cycle response in DE3(2) variability on Q10DW timescale is more likely to come from transient events that have a solar cycle signal in NH winter where DE3(2)-Q10DW interaction occurs.

In a recent study, using geopotential measurements from Aura/Microwave Limb Sounder (MLS), Yamazaki & Matthias (2019) reported an unusual enhanced Q10DW activity at 55° latitude between 48- and 97-km altitudes caused by the final breakdown of the stratospheric polar vortex of 2016, 2015, and 2005 in NH winter due to the occurrence of sudden stratospheric warmings (SSWs). Labitzke & van Loon (1988) showed earlier that the polar warming in NH late winter is due to the occurrence of SSWs and the polar temperature is positively correlated with the solar cycle when the QBO is in the westerly phase, also known as solar cycle-QBO teleconnection effects. Camp & Tung (2007) later showed that a perturbed polar vortex can occur during easterly QBO at any stage of the solar cycle, while during westerly phase, a more disturbed vortex occurs during solar maximum. More importantly, the least-perturbed state of the polar stratosphere is at solar minimum and westerly QBO. This implies that a solar cycle signal in DE3(2) likely arises due to modulation by the westerly QBO, yielding a positive correlation with the solar cycle. This provides a consistent explanation for why DE3(2) on a Q10DW timescale has a strong positive correlation with the solar cycle. In addition, the lack of Q10DW transients during solar min/westerly QBO combined with the solar-cycle independence during easterly QBO conditions, which is along the QBO response of Q10DW in NH as shown in Table 3.3, then explains why there is no QBO signal in DE3(2), and why DE3(2) is heavily dominated by the solar cycle. Note that SSWs generally occur in the NH wintertime and rarely in the

SH, with an exception being a major 2002 Antarctic SSW event. Furthermore, DE3(1) overlap is large in the SH winter and rather small in the NH winter which explains the absence of a solar cycle response in DE3(1) variability. It would be worthwhile to test this scenario implied by our observational diagnostic with dedicated numerical modeling, which is of interest for future work.

Overall, the information-theoretic approach presented here can be used to statistically analyze short-term tidal variability on various planetary wave timescales. The important findings are that the DE3 short-term tidal variability on a 10-day planetary wave timescale depends on various propagation and forcing conditions such as QBO, ENSO, and solar cycle. Most interestingly, stratospheric polar vortex conditions are important for transmitting solar cycle signals into DE3 short-term variability at mid-equatorial latitudes. This highlights the importance of the study of the day-to-day tidal variability on a global scale.

CHAPTER FOUR

INTRASEASONAL VARIABILITY IN DIURNAL TIDES

4.1 Madden Julian Oscillation: An Intraseasonal Mode of Tidal Variability

The intraseasonal peak at 40-90 days in the Fourier spectrum of tidal diagnostics in the MLT region has been recognized in relation to the tropical tropospheric Madden-Julian Oscillation (MJO) (Gasperini et al., 2020; Kumari et al., 2020; Vergados et al., 2018; Yang et al., 2018). Sassi et al. (2019) suggested that MJO-related intraseasonal variations in the ionosphere are integral to improving space weather modeling and forecasting. Briefly, MJO is the dominant form of intraseasonal variability in the tropical atmosphere (Madden & Julian, 1972) and it is characterized by large-scale convective anomalies that develop over the tropical Indian Ocean and propagate slowly (~5 m/s) eastward over the western-central-eastern Pacific with individual events lasting 30 to 90 days (e.g., Zhang, 2005). Figure 4.1 depicts the eastward propagating MJO manifested in precipitation (rainfall) anomalies with its locations as integer phases 1-8. Like QBO and ENSO indices, the RMM (Real-time Multivariate MJO) index by Wheeler & Hendon (2004) is widely used for monitoring the strength (amplitude) and location (phase) of the MJO-convection. Figure 4.1 shows that the MJO-phases generally coincide with locations along the equator around the globe. For convenience, one defines 8 different MJO phases i.e. location of MJO-convection, numbered 1 through 8 (8&1: western hemisphere and Africa, 2&3: Indian Ocean, 4&5: maritime continent, 6&7: western Pacific).

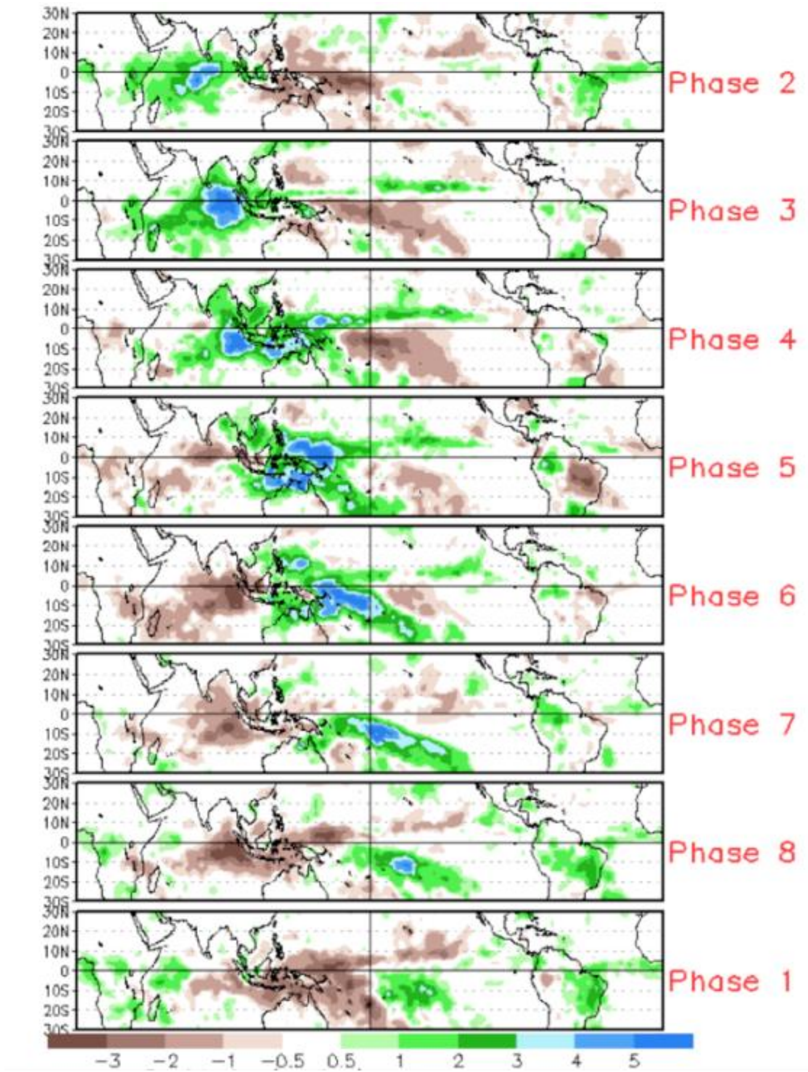

Figure 4.1: Difference from average rainfall (anomalies, mm/hr) for all MJO events from 1979-2012 for November-March for the 8 phases. The green shading denotes above-average rain fall and the brown shading denotes below average-rainfall. Note that the anomaly pattern propagates eastward. (NOAA MJO webpage)

An active-MJO event occurs when the MJO amplitude or RMM indices is greater than 1-1.5 for 5 consecutive days, i.e., the commonly used definition of active-MJO events. Figure A1 (see additional figures in Appendix toward the end of this thesis) shows the monthly distribution of active-MJO events during 2002-2018 years for both conditions (amp>1 and amp>1.5). Note that amp>1.5 is a stricter condition to select an MJO-event than amp>1, while both conditions (Figure A1a and A1b) show similar monthly distribution of MJO-events with higher number of MJO-active events in winter (1^{st} -3^{rd} and 12^{th} months on x-axis) than the summer (6^{th} -9^{th} months on x-axis). Figure A2 shows how the distribution of active-MJO events (number of days) for both conditions varies with seasons (winter (DJFM) and summer (JJAS)) and additionally as a function of MJO-phases. Figure A2 also shows that the phase 5-8 cluster corresponding to the active-MJO events are more common in the NH winter, while during the NH summer phase 1-5 cluster are more common.

The MJO is an eastward propagating Kelvin wave radiating away from the source region (Madden & Julian, 1994) and the study of MJO is especially interesting due to its relevance to the climate change research and Indian Monsoon prediction. Since the MJO is confined to the lower atmosphere (e.g., Tian et al., 2012; Zhang, 2005) due to its low frequency and slow zonal propagation speed, it may modulate the upward propagating tides and gravity waves (GWs) and thus potentially induce the same periodic signatures across a broad range of vertical levels. This makes the study of MJO effects important for the upper atmospheric dynamics. Eckermann et al. (1997), Lieberman et al. (1998), Garcia (2000), Isoda et al. (2004), and Kumar et al. (2007) suggested that the intraseasonal oscillations in the MLT zonal winds are possibly due to the intraseasonal variabilities in tides as a response to MJO-related convective forcing. Li & Lu (2020) found the modulation with respect to the locations of MJO-convection in GW temperature variances at SABER altitudes, while Yang et al. (2018) studied the modulation of intraseasonal signals in the MLT tides corresponding to the MJO-locations from numerical simulated tides with realistic tidal forcing in the lower atmosphere by SD-WACCMX (an explanation of SD-WACCMX model tidal simulations is provided later in section 4.2.3) . Figure 4.2 shows the modeled MLT DW1 temperature tidal climatology from the latter paper (that is, averaging DW1 amplitudes for 1979-2018 years) along with the intraseasonal anomalies in percentage (of seasonal mean) as a function of MJO-phase in boreal winter (December-February, DJF).

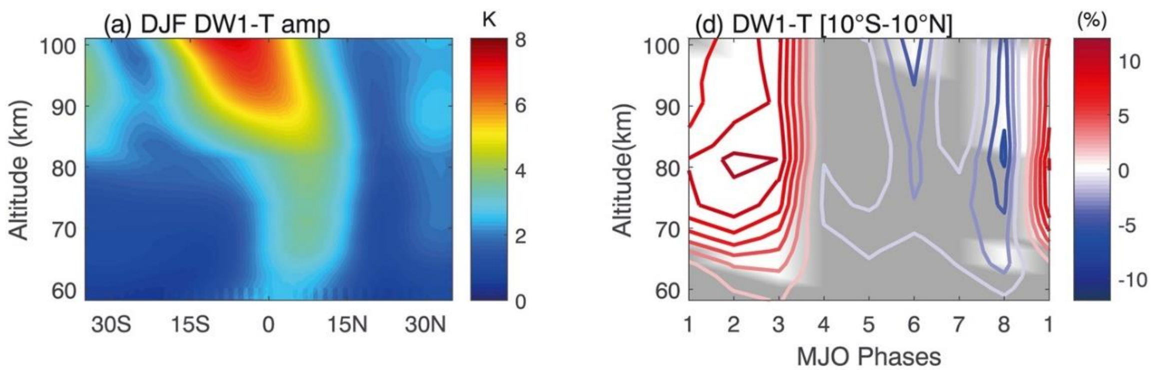

Figure 4.2: Left: Climatological mean of SD-WACCMX DW1 amplitudes in T(K) in the MLT, region during DJF months. Right: anomalous percentage variances of the mesospheric DW1 amplitudes in temperature averaged over 10ºS-10ºN for each MJO phase during DJF. (Yang et al., 2018)

In a statistical sense, Yang et al. (2018) found a clear connection between intraseasonal signals in DW1 from SD-WACCMX and the MJO: depending on the MJO phase (its location), convective anomalies lead to an enhanced/reduced DW1 forcing with amplitude differences of about 20% (peak-to-peak, ±10%). Briefly, the increased/decreased moisture over the enhanced/suppressed deep convection in a given MJO phase leads to stronger/weaker radiative DW1 forcing through increased/decreased water vapor in the equatorial troposphere (5–13 km altitude, 10°S–10°N). Yang et al.

(2018) also showed that the DW1 winds in the MLT region have variances as a function of MJO-phases similar to what is shown in the Figure 4.2 for DW1 temperature tides. In further investigation, Yang et al. (2018) found that the MJO-modified GW momentum forcing on the DW1 also plays a role, according to the model. Such analysis for intraseasonal variability in DE3 tides was not performed. Gasperini et al. (2017) found a 90-day signal in zonal mean winds and a DE3 proxy (“wave4”) derived from CHAMP and GOCE in the thermosphere but could not conclusively relate the signal to the MJO, because of ambiguities in the data analysis approach. In the following, the objective is to quantify the intraseasonal diurnal tidal variability as a response to MJO from observations and to delineate the causes which transmit the MJO response in tides up to the MLT region, along with supporting model simulations.

4.2 Analysis and Results

4.2.1 Intraseasonal Tidal Variability in SABER Tides: As a Function of MJO

To test the model hypothesis following the Yang et al. (2018) DW1 model study, Kumari et al. (2020) diagnosed the intraseasonal DW1(1) tidal variability as a function of MJO phase using SABER observations and extended the diagnostics to the nonmigrating DE3(1&2) component. Note that Yang et al. (2018) do not analyze the HMEs projection of DW1. The first step of the approach includes extract/filtering the intraseasonal (30-90-day) variability in MLT diurnal tidal amplitudes using a Lanczos bandpass filter. The next step is to identify active MJO events in each season using MJO amplitudes from the RMM index and then group the remaining set of bandpass-filtered tides (or anomalies) in 8 bins corresponding to 8 MJO phases, using the MJO-phase information of the corresponding active-MJO days. This allows one to relate the intraseasonal variability in tidal amplitudes with the MJO phases (as shown in Figure 4.2 with simulated DW1). Percent deviations from the seasonal mean was used in order to quantify the MJO signal in diurnal tidal variability at each MJO phase. Figure 4.3a shows the altitude structure of observed variations in DW1 HME1 amplitude (from SABER) as a function of MJO phases/locations in winter (DJF). The percent deviation (Figure 4.3b, shown for completeness) from the seasonal mean, however, is independent of altitude as the altitude and latitude structure is fully contained in the HME basis functions (Figure 2.5, Chapter 2). Therefore, the fit coefficients corresponding to each HME fit are altitude independent. It yields identical results to the percent deviations of the fit coefficients (Figure 4.3c).

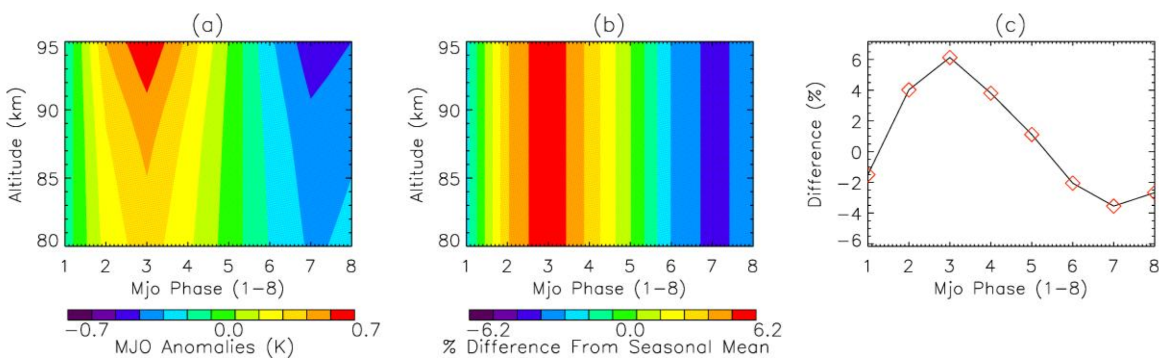

Figure 4.3: a) DJF bandpass filtered MJO anomalies in SABER observed DW1 HME1 amplitudes (K), averaged 10ºS-10ºN and grouped in 8 MJO phases corresponding to active MJO events. Note that DW1 HME1 amplitudes maximize at 95 km. b) Percent deviation of anomalies from the DJF mean at each phase (altitude independent by construction). C) The black curve is the amplitude percent deviation from b) and the red squares are the percent deviations obtained using bandpass filtered DW1 HME1 fit coefficients. (Kumari et al., 2020)

During boreal winter, the intraseasonal variability in DW1 tides as a function of MJO phase is ~10% (peak-to-peak difference) and somewhat smaller compared to the 15-

20% reported by Yang et al. (2018) in their model study (shown as the plot in the right within Figure 4.2). Nonetheless, the sign of the response found in Figure 4.3c for the various MJO phases largely agrees with their findings and as such gives observational credibility to the model prediction of how the MJO modulates the tides.

Note that Yang et al. (2018) only show DW1 results in boreal winter and do not provide model results for the DE3 component. However, it is certainly worthwhile to perform such analysis in each season and for intraseasonal variability in DE3 HME1 and HME2 timeseries. Seasonal means from each of the DW1 HME1, DE3 HME1 and HME2 amplitude timeseries (reconstructed using HME fit coefficients) were estimated for each season, i.e., northern hemisphere (NH) winter (December-January-February, DJF), NH spring (March-April-May, MAM), NH summer (June-July-August, JJA) and NH fall (September-October-November, SON) and the analysis followed the same methodology as used for Figure 4.3. For DE3, the seasonal variation is important as DE3 is equatorial during summer but nonequatorial in winter, this study is important in this context because one can investigate the contribution due to direct equatorial MJO- forcing (important for HME1 mode) or indirectly due to wind filtering effects (which is important for HME2 mode).

The results are summarized in Figure 4.4 that shows a comprehensive view of the intraseasonal variability in MLT diurnal tides as a function of season and MJO phases/locations for active MJO days. 50 Monte-Carlo simulations were used to calculate the uncertainty based on a tidal amplitude error (~1 K) estimated during the tidal deconvolution followed by HMEs projections of SABER temperatures. The length of the error bars (red bars) is <1% (equivalent to 0.02 K) for Figures 4.4a-h and does not exceed 9% (~ 0.12 K) for Figures 4.4i-l. Overall, the error bars are smaller than the change of percent deviation values in between MJO phases, which highlights the statistical significance of the tidal response. The error bars for DE3 HME2 (Figure 4.4i-l) are significantly larger than those for DW1 HME1 and DE3 HME1, due to the generally smaller amplitudes of DE3 HME2 (Figure 2.7e; Chapter 2).

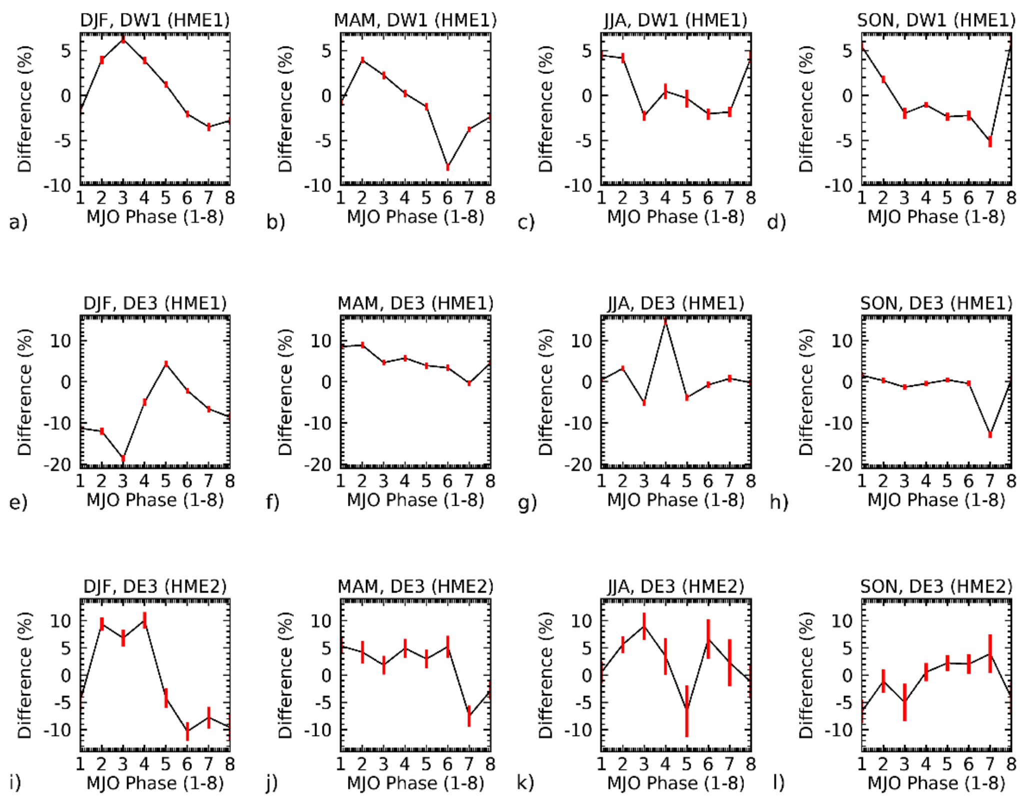

Figure 4.4: The statistical tidal response to the MJO (a-d; DW1 HME1, e-h; DE3 HME1, and i-l; DE3 HME2) in each season (DJF, MAM, JJA, and SON), computed with respect to the corresponding seasonal mean. The red bars are the corresponding error estimates. (Kumari et al., 2020).

It is evident that both the migrating and nonmigrating tides are considerably modulated by the MJO phase with the details of the responses varying from one season to another. The migrating diurnal tide has significant variability in spring (MAM, ~15%) and fall (SON, ~11%), while smallest in summer (JJA, ~7%). Interestingly, the MJO effects in both HME modes of the nonmigrating DE3 tide can be quite different and are possibly related to mode coupling (Chapter 1) in the stratosphere and lower mesosphere. The nonmigrating tidal response (~25%) to the MJO is about twice as strong as the migrating tidal response in summer (~8%) and winter (~10%). Moreover, the seasonal variation of the MJO response in nonmigrating tides is more prominent than in the migrating tides.

This is interesting as the similar intraseasonal variability modulation with MJO-phase are expected to be imposed on the ionosphere region through dynamo winds, similar to ENSO/tidal modulation (e.g., Jones et al., 2014, 2019). However, the analyses by Yang et al. (2018) and Kumari et al. (2020) do not enable the study of underlying physical mechanisms. Obtaining insight into the latter is the main goal of the following sections. It is also vital to do the extraction of eastward propagation anomalies for the tidal MJO-response diagnostics (Wheeler & Kiladis, 1999), because the MJO is an eastward propagating phenomenon. This requires the analysis to involve tidal phases. In the following, the text includes extraction and statistical characterization of the tidal MJO-response from the intraseasonal tidal anomalies. Subsequently, the findings of the study of the tidal MJO-response along with its underlying causes was submitted for journal publication (Kumari et al., 2021; submitted to JGR-Atmospheres). The following text contains details of the analysis and results and is largely taken from the submitted article.

4.2.2 MJO Signal Extraction in the MLT Tides: Hovmoeller Analysis

The SABER/MJO tidal diagnostic adopts the standard MJO diagnostic used in climate research and Monsoon prediction, which is Hovmoeller analysis (Wheeler & Kiladis, 1999) but applied to the tidal anomalies. The steps for Hovmoeller analysis are as follows: (i) compute tidal wave perturbations ($\mathrm{T_{s,n}}\cos(\omega_n t - s\lambda - \varphi)$; both amplitude and phase) for each day as a function of latitude and longitude (i.e., tidal deconvolution followed by HME projections explained in Chapter 2), (ii) compute a daily "composite-day" climatology by averaging the perturbations from multiple years (i.e., 2002-2019 for SABER), (iii) compute deviations (anomalies) from the climatology for each day, (iv) apply a 30-90 day bandpass filter and (v) extract the eastward-propagating signal (since the MJO is by definition eastward-propagating). Here, the Hovmoeller analysis with tidal perturbations uses tidal phase information unlike Gasperini et al. (2020), Kumari et al. (2020), and Yang et al. (2018) which used only the tidal amplitudes (not tidal phases) for their analysis. Noise errors in the input data diminish in the filtered data because of the bandpass filtering. The results of these steps are shown as Hovmoeller plots of the tidal components in Figure 4.5a, 4.5b and 4.5c, as MJO-signal/response at all longitudes from 2008 to 2010 of SABER tidal anomalies at 95 km in DW1-HME1 (DW1(1)), DE3-HME1 (DE3(1)) and DE3-HME2 (DE3(2)), respectively. The last step of the Hovmoeller analysis involves latitude averaging of the tidal anomalies. Note that HME1 is symmetric with respect to the equator and HME2 is antisymmetric. This is why the Hovmoeller analysis uses the latitude averaging from 20^{o} S to 20^{o} N for HME1 while equator (0^{o}) to 20^{o} N for HME2.

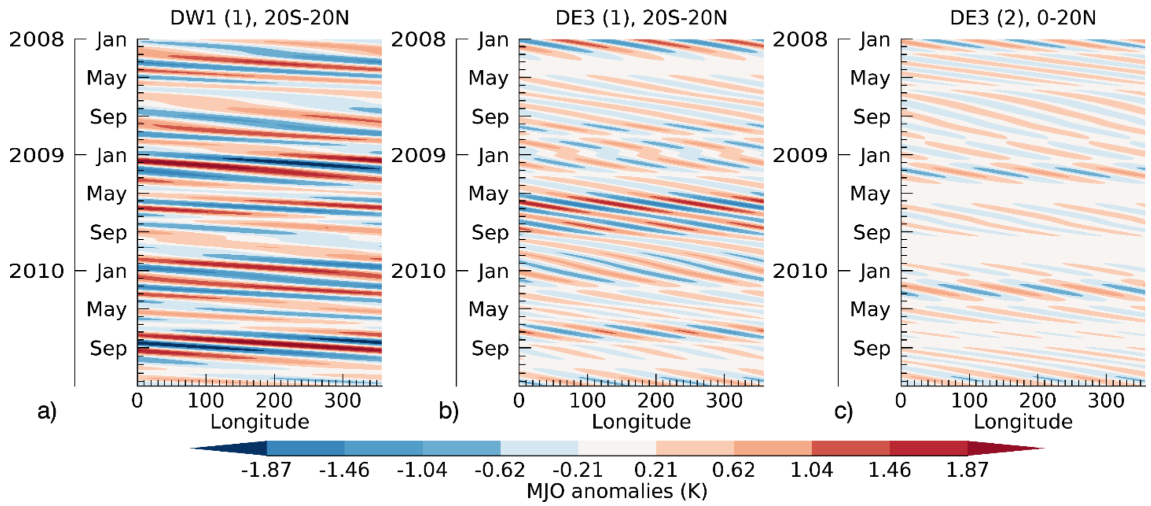

Figure 4.5: SABER Hovmoeller plots of the MJO-response during 2008-2010 and 95 km in a) DW1-HME1, b) DE3-HME1, and DE3-HME2. The latitude ranges used are 20^{o} S-20^{o} N and 0^{o}-20^{o} N for HME1 and HME2 modes, respectively.

Figure 4.5 shows how the MJO-response is unique for each of the HMEs. DW1(1) shows a larger response throughout the years 2008-2010 in comparison to DE3(1&2). However, the seasonal variation in the MJO-response is more evident in DE3(1&2). In particular, DE3(2) shows a larger response in winter months and DE3(1) shows a larger response in summer months.

The exact mechanisms and their relative importance are topics for dedicated model studies combined with observational support. In the following, a comparative analysis of tidal MJO-response as a function of MJO-phases/locations in SABER observations and SD-WACCMX model simulations of tides is studied as the agreement between model and observations enables the study of underlying causes of tidal variability modulated with MJO-phases.

4.2.3 Statistical Characteristics of the Tidal MJO-Response as a Function of MJO-Phase: SABER & SD-WACCMX

The Whole Atmosphere Community Climate Model with thermosphere and ionosphere extension (WACCMX) is a comprehensive numerical model, spanning the range of altitude from the earth's surface to the upper thermosphere (Liu et al., 2010, 2018; Marsh et al., 2013). The scientific goals of the model include studying solar impact on the earth's atmosphere, couplings between atmosphere layers through chemical, physical and dynamical processes, and the implications of the coupling for the climate and for the near space environment. A continuous run from 2002 to 2018 of the Specified Dynamics version of WACCMX (SD-WACCMX) has been performed on Clemson University's Palmetto supercluster by Dr. Xian Lu's research group and the one hourly output data are used in this study. A 2D sinusoidal fitting of wavenumbers from -6 to 6 and periods of 24, 12, 8 and 6 hours with respect to all longitudes and 5-day time interval is done on the SD-WACCMX temperature field to extract the amplitude and phase of each tides for the centered day. The 5-day window is chosen to suppress the contamination of long-period waves (such as planetary waves) on tidal retrieval while maintaining the information of short-term tidal variability. This 2D fitting is repeated by moving its window one day ahead to obtain the tidal timeseries for all 18 years of data. Here, the 2D fitting with shorter time interval than 5-day do not change the characteristics of the tidal variability on the intraseasonal (MJO) timescale. In Figure 4.6, the amplitude and phase comparison between SABER and SD-WACCMX tidal diagnostics (HME fits included) show clear agreement in terms of major seasonal/latitudinal characteristics between observational and model studies of diurnal tides. A 11-day running mean smoothing is applied for illustration purposes.

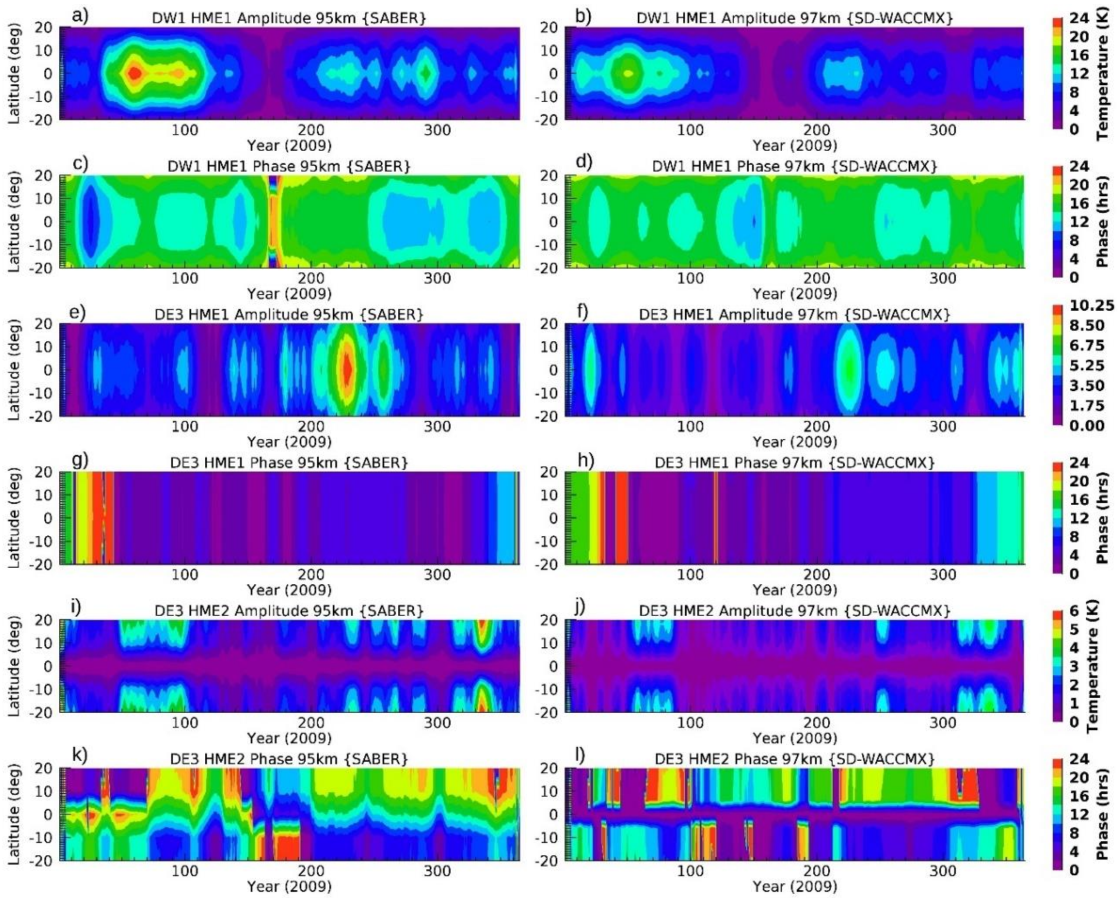

Figure 4.6: Amplitude and phase of SABER (left, 95 km) and SD-WACCMX (right, 97 km) temperature diurnal tidal components (a-d) DW1-HME1, (e-h) DE3 -HME1, and (i-l) DE3-HME2 during 2009.

Figure 4.6 also depicts the similarity in the seasonal variation (winter/summer) and the latitude structure (symmetric/antisymmetric) of the HMEs amplitudes between SABER and SD-WACCMX tides. DW1(HME1) and DE3(HME2) have a maximum in winter, respectively, while DE3(HME1) maximizes in summer. The seasonal characteristics of day-to-day variability in each HMEs simulated by SD-WACCMX is consistent with the observed SABER tides. There are small differences between short-term tidal variations in SABER observations and SD-WACCMX simulations, such as, DW1(HME1) simulated by SD-WACCMX in compare to observed by SABER shows larger tidal amplitudes in January month. Also, SD-WACCMX simulations of tides underestimate the short-term variations as the observed tides show larger amplitudes in comparison. Overall, these small differences are unlikely to play a large role in the intraseasonal tidal variability and the model can thus be used to explain the observed characteristics of the tidal variability on MJO-timescale.

To establish the general consistency of the SD-WACCMX tidal (DW1(1), DE3(1&2)) response to the MJO and SABER, one can first perform a statistical study as a function of MJO-phases using a similar approach as Yang et al. (2018) and Kumari et al. (2020). In this thesis, the statistical study of the MJO-responses in the SABER and SD-WACCMX tides (calculated using the 2002-2019 climatology) has used the years 2004-2017. After grouping the timeseries of tidal MJO-signals (from Hovmoeller plots of 2004-2017 at all longitudes, similar to Figure 4.5) in 8 MJO-phases for active-MJO days, the mean value in each bin is taken as the statistical measure of the MJO-response in an MJO-phase/bin. Figure 4.7 shows how the MJO-responses in the SABER DW1 and DE3 tidal components modulate with respect to MJO-phases 1-8 in the NH winter (with spring), i.e., December-January-February-March (DJFM) months and NH summer (with fall), i.e., June-July-August-September (JJAS) in the MLT-region at 95 km. It is to be noted that the number of days used for the averaging in each MJO-phase/bin varies from winter to summer and there are similar proportions of days in each bin for both conditions (i.e., amp

>1 & amp>1.5, Figure 4.2 and 4.3) which means that both conditions can be used to select active-MJO days for the statistical analysis.

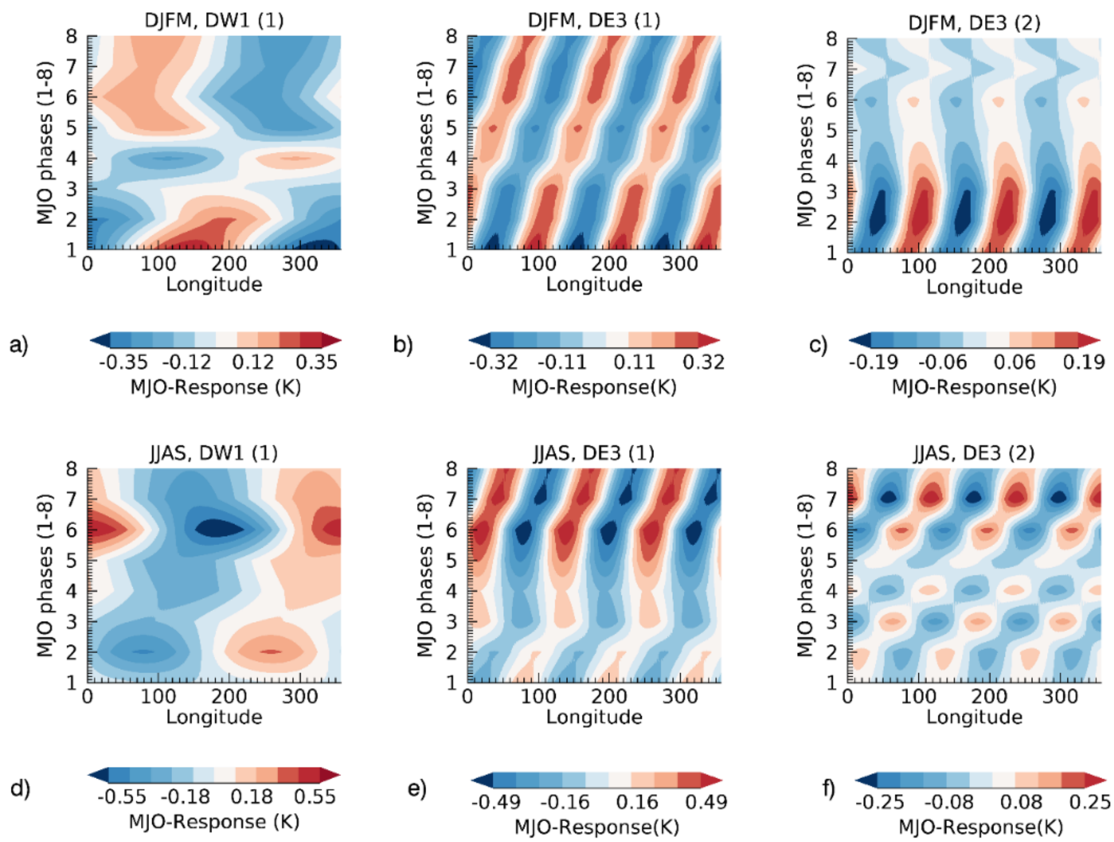

Figure 4.7: The statistical characteristics of the tidal MJO-response from SABER as a function of MJO-phases/locations, retrieved from years 2004-2017 of Hovmoeller timeseries of DW1(1), DE3(1), & DE3(2) in a), b), & c) NH winter and in d), e), & f) NH summer. The latitude averaging for HME1 modes uses the range 20^{o} S-20^{o} N, while 0-20^{o} N is used for the HME2 mode.

Figure 4.7 shows the largest statistical response in DW1(1) (Figure 4.7a & 4.7d) with respect to the MJO-phases, which is comparable to the MJO-response in DE3(1) (Figure 4.7b & 4.7e) while DE3(2) (Figure 4.7c & 4.7f) has a comparatively smaller response. The longitudinal structure (x-axis, Figure 4.7) for the MJO-response in DW1(1) has a zonal wave number 1 corresponding to DW1. Similarly, the MJO-response in DE3(1&2) shows a zonal wave number 3 longitudinal structure corresponding to DE3. The variation of the tidal MJO-response with respect to the MJO-phases/locations (y-axis, Figure 4.7) is evident in all three tidal components.

The amplitude (A) and phase (ϕ) of the MJO-responses shown in Figure 4.8 (black lines) has been retrieved from Figure 4.7a-f by fitting $Acos(n\lambda - \phi)$, where λ=longitude and n=1(DW1) and 3(DE3). This is to remove the longitudinal dependence in Figure 4.7. In other words, the black lines in Figure 4.8 show amplitudes and phases of the MJO-response in DW1(1) and DE3(1&2) at 95 km in winter (DJFM) and summer (JJAS) season retrieved from Figure 4.7. The statistical characteristics can then be studied in terms of the amplitude and phase of the MJO-response and their modulations with respect to the 8 MJO-phases. Note that the phase of the tidal MJO-response ϕ in radian is basically the phase in longitudes (i.e. x-axis in Figure 4.7) at each of the MJO-phases (i.e. y-axis in Figure 4.7), where the MJO-phase is the geographical location of MJO-convection given as an integer from 1 to 8 (see section 4.1). Figure 4.8 mainly shows the MJO-response in temperature tides from SABER (~95 km, black lines) as well as SD-WACCMX (~97 km, green lines) for NH winter (DJFM) and NH summer (JJAS) seasons. Regarding SABER MLT tides, the noise errors are diminished in the bandpass filtering (Figure 2.9, Chapter 2) and Kumari et al. (2020) (as described in section 4.2.1) showed that the total error due to the tidal deconvolution and HME fittings (which is ~1K) constitute 1%-9% (0.02-0.12 K) in the intraseasonal tidal variability varying as a function of MJO-phases. With this error, the modulation of intraseasonal variability with respect to the MJO phases is statistically significant and hence the MJO-response in SABER tides using Hovmoeller analysis is statistically significant. Figure 4.8 shows the comparative analysis of the MJO-response in each of the tidal components at 95 km from SABER observations and at 97 km from SD-WACCMX simulations.

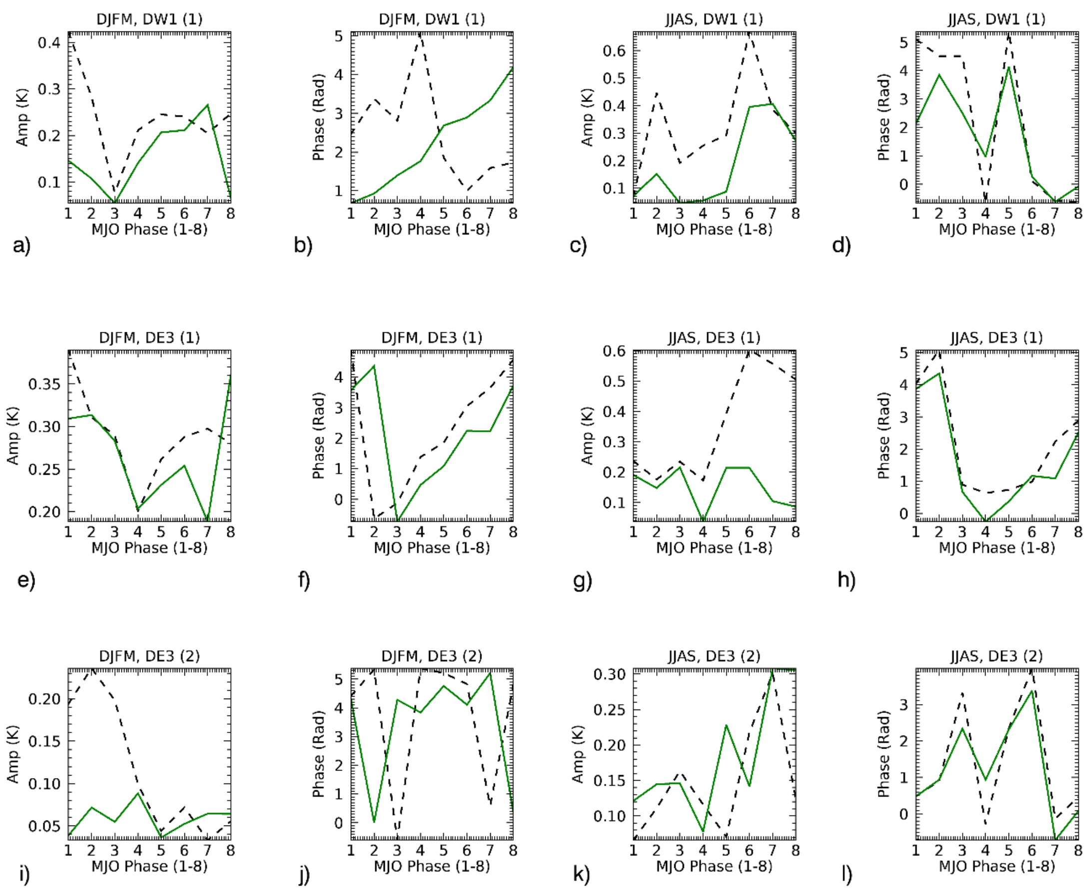

Figure 4.8: Comparative analysis of the MJO-response in SABER tides at 95 km (black-dashed) vs SD-WACCMX tides at 97 km (green) tides (tidal amplitude and phases shown in Figure 4.6).

The characteristics of the amplitudes and phases of the MJO-response as a function of MJO-phases in SABER diurnal tides during winter/summer season are generally consistent with the SD-WACCMX diurnal tides with the exception of DW1(1) and DE3(2) during winter, as shown in Figure 4.8b. Some systematic phase differences can be caused by the fact that the tides in the model and observations have a different vertical wavelength (e.g., SD-WACCMX tides maximize at slightly higher altitudes than SABER tides). Note that there is considerable variation taking place as a function of MJO-phases from winter to summer in all three tidal components and the amplitude of the MJO-response is larger in summer then winter. The seasonal modulation of the double peak amplitude structure as a function of MJO-phases (1-4 & 5-7) from winter to summer is evident in all three tidal components. The amplitudes and phases in longitudes are retrieved from Figure 4.7 where the y-axis in Figure 4.7 is the same as x-axis here. Note that the y-axis range is different for each of the plots and the difference shows the comparison in winter/summer amplitudes and phases for all the three tidal components. Overall, the observations support the results from the model simulations, which enables the following model-based study of underlying physical mechanisms.

4.3 Causes of Tidal MJO-Response in the MLT Region

Lieberman et al. (2007) proposed that whole-atmosphere coupling involving tidal variability may occur via (i) direct amplitude modulation by tropospheric heating, (ii) zonal mean flow interactions that modulate the tidal behavior as waves propagate through a variable background in middle and upper atmosphere or (iii) nonlinear wave-wave interactions. The MJO is known to modulate stratospheric gravity waves (GW), GW drag and zonal winds (e.g., Alexander et al., 2018; Eckermann et al., 1997; Li & Lu, 2020; Lieberman, 1998). As such, any MJO modulations of the MLT tides can be imposed by an

MJO in tropospheric forcing as well as strato/mesospheric winds, GW momentum forcing, and possibly other effects.

As the Modern-Era Retrospective analysis for Research and Applications version 2 (MERRA2, Gelaro et al., 2017) data are nudged from the surface to 60 km in SD-WACCMX model runs, one can study the tidal MJO-forcing in the tropospheric region using MERRA2 datasets. 3-hourly output from MERRA2 (Gelaro et al., 2017) are used to obtain other parameters of interest such as winds, pressure, surface specific humidity, latent and radiative heating needed for our study. Powell (2017) demonstrates that the heating profiles (temperature tendencies (K/s) due to moist/latent and radiative processes) in MERRA2 are sufficiently good for MJO studies. The next section 4.3.1 describes the MJO-response in each of the tropospheric tidal forcing components, i.e., DW1 and DE3 in the latent and radiative heating profiles. Section 4.3.2 then quantifies the MJO-response in MERRA2 tropo/stratospheric zonal and meridional wind to study the wind filtering effects on tides due to the MJO in the tropo/stratosphere region. Two SD-WACCMX runs are performed. The first one is the control run with the default MERRA2 nudging setup, which is used for Figure 4.8. In the second run, the MJO signals in the zonal and meridional winds of the MERRA2 data are removed first, and then used to nudge the SD-WACCMX (section 4.3.2). By removing the MJO signals in the zonal and meridional winds up to 60 km, the effects from the background wind filtering in the troposphere and stratosphere are suppressed. This is to distinguish the MJO-response in MLT tides due to the tropospheric tidal forcing from the wind filtering effect.

Therefore, multiple datasets (e.g. SABER, MERRA2, SD-WACCMX) are being used to close the gap in our understanding of how MJO forcing in the troposphere manifests itself in tides in the MLT region.

4.3.1 MJO-Response to Tropospheric Tidal Forcing

Tropospheric forcing needs to be studied using the same frequency/wavenumber picture as in the MLT (e.g., DE3, DW1) and subsequently their Hough mode (HM from classical tidal theory in Chapter 1, not altitude-extended HME) projections. Firstly, the DE3 and DW1 forcing in radiative and latent heating (i.e. tidal forcing in the troposphere region) from MERRA2 (2002-2019, in K/d units) are used to perform HM projection after averaging the forcing between 100-500 hPa (integrating the heating altitudes) in the troposphere. The retrieval of MJO-response in both radiative and latent forcing is derived using Hovmoeller analysis, just as in section 4.2.2 (i.e., for SABER and SD-WACCMX tides in the MLT region). However, the active MJO events in this case are chosen as the days when MJO amplitudes are greater than 1 for 5 consecutive days, which is a less strict condition to select active MJO events compared to the 2004-2017 analysis from section 4.2.3 (which used MJO amplitudes greater than 1.5 for 5 consecutive days). This is for plotting purpose because the MJO-response retrieved using this active-MJO condition provides better agreement with SABER MLT-tidal MJO-response than the condition used in section 4.2.3. As described in section 4.1, active MJO events have similar proportions of days in each bin for both conditions (i.e., RMM amplitudes >1 and >1.5), so choosing either of the conditions should not change the characteristics of MJO-response as a function of MJO-phases.

Figure 4.9 shows the amplitudes and phases of the MJO-response in radiative (red lines) and latent heating (blue lines, the amplitudes shown are multiplied by 3 for plotting purposes) in each season for each of the tidal components. The black lines in Figure 4.9 indicate amplitudes and phases of the MJO-response in SABER MLT-tides. Note that the SABER amplitudes are in Kelvin and multiplied by 0.05 for plotting purposes.

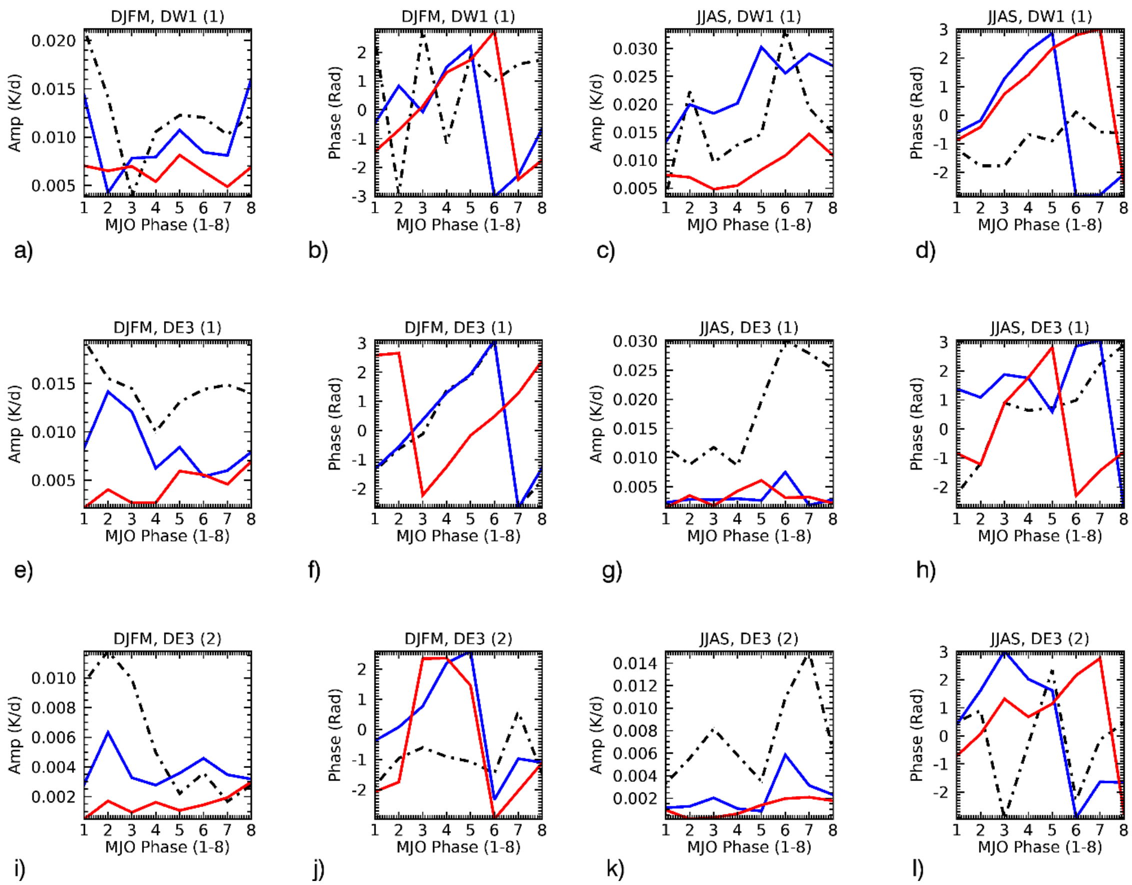

Figure 4.9: Comparative analysis of the characteristics of the MJO-response in SABER (black-dotted) with the response in the radiative heating (red) and latent heating (blue). The unit of radiative and latent heating forcing is K/day, while SABER tides (95 km) are measured as temperatures. The MJO-response in SABER tides is multiplied by 0.05 and the response in latent heating is multiplied by 3 for plotting purposes.

The black dotted lines in Figure 4.9 are same as the black dotted lines in Figure 4.5, while the negative phase values of MJO-response (Figure 4.9b, 4.9d, 4.9f, 4.9h, 4.9j, & 4.9l) have not been shifted to positive values by adding 2π with respect to the corresponding phases in Figure 4.8. This is for plotting purposes only and in order to do the comparative analysis with the phases of MJO-response in radiative and latent heating.

Interestingly, for DW1(1) and DE3(2), the modulation of the phases of the MJO-response with MJO-phases in radiative heating (red lines in Figure 4.9, heating altitudes 100-500 hPa integrated) is generally consistent with the phases of the MJO-response in latent heating (blue lines in Figure 4.9) but the scenario is different for the DE3(1). Yang et al. (2018) discussed that increased moisture due to latent heating forcing in troposphere results in an enhanced radiative heating at the MJO-phases (i.e., location of MJO-convection). In other words, Yang et al. (2018) expected that the latent and radiative MJO-forcing to tides are related. Understanding the apparent phase inconsistencies of MJO-response among radiative and latent forcing for DE3(1) while being consistent for DE3(2) requires additional insights and is beyond the scope of this thesis. In summer (JJAS), the characteristics of amplitude modulation with MJO-phases/locations in both the radiative (red lines in Figure 4.9) and latent (blue) tidal tropospheric heating are consistent with the amplitude modulation in SABER (black). In winter (DJFM), the amplitude modulation of the MJO-response is more consistent with the latent MJO-forcing, while the modulation in radiative heating is somewhat consistent with the MLT tidal MJO response. The phases of MJO-response in either season in Figure 4.9, however, are generally not consistent between the tidal forcing and SABER MLT tides (black dotted curve). This is, however, expected as wind filtering and additional effects are also important in transmitting the MJO signal into the tides, as discussed more closely in the following section. Nonetheless, the latent and radiative MJO-forcing together explain important characteristics of amplitudes (magnitude) of MJO-response as a function of MJO-phases in the MLT-region. The amplitudes of MJO-forcing in the latent and radiative tidal heating terms are comparable in the winter and summer seasons, which does not explain the seasonal difference in amplitudes of the MJO-response (function of MJO-phases) in SABER and SD-WACCMX tides.

4.3.2 Delineating Tropo/Stratosphere Wind Filtering Effects

In order to extract the wind filtering effect in the tropo/stratosphere, the MJO-responses in zonal (U) and meridional (V) winds from MERRA2 are analyzed. This analysis uses the years from 2008 to 2010, which are characterized by several large MJO-activities in the tropical-convection, the so-called "year of tropical convection" (Waliser et al., 2012). Previously, the MJO-response of tropo/stratospheric zonal winds to different MJO-phases has been discussed by Alexander et al. (2018) using another methodology, which used the difference between MERRA2 zonal wind composites in calculated each MJO-phase for active MJO days (with amp>1 condition) and the MERRA2 wind 2003–2011 climatology (monthly mean zonal wind) weighted by the frequency of occurrence in that month in each MJO phase but without selecting the active MJO events. Essentially, Alexander et al. (2018) calculated the MJO-anomalies using the climatology per MJO-phase and by comparing with and without active MJO events.

In the following analysis, the anomalies are computed first and then the MJO-phase information is used for each active MJO-events to get the variability characteristics as a function of MJO-phases. Here, the Hovmoeller analysis is used to extract the eastward propagating MJO-response in zonal and meridional wind anomalies from the troposphere to the stratosphere (1000-0.5 hPa). The climatology was calculated using 18 years (2002-2019, same number of years used as Figure 4.5) of MERRA2 winds to get the wind anomalies of 2008-2010. Figure 4.10 shows the longitudinal variability of the MJO-response during 2008-2010 in zonal (left) and meridional (right) wind anomalies for the winter season (i.e., DJFM) in each of the MJO-phases. One can see the eastward propagating longitudinally dependent MJO-response evident in the troposphere (i.e., > 120 hPa) for both zonal and meridional winds, while longitudinally independent global MJO-response in the zonal wind anomalies can be seen in the stratosphere (30-0.5 hPa). The MJO-response in stratospheric zonal wind anomalies changes its sign depending on the MJO-phase. Note that the wind anomalies in zonal winds are large (±5 m/s) compared to those in meridional winds (± 3 m/s). An analysis for summer (JJAS) months shows a bigger MJO-response in zonal winds up to ±8 m/s, while the response in meridional winds is of similar magnitude (±4 m/s) (Figure A3 shown in Appendix section). This highlights the seasonal variation in the MJO-response in the winds which may have contributed towards the observed seasonal variation in the MLT tidal MJO-response. Most importantly, for winter months the zonal wind anomaly variation with MJO-phases is consistent with the findings by Alexander et al. (2018) except that the magnitude of the variations in their study are an overestimate of up to ±5 m/s when compared to the present findings. This could be due to the difference in analysis methods.

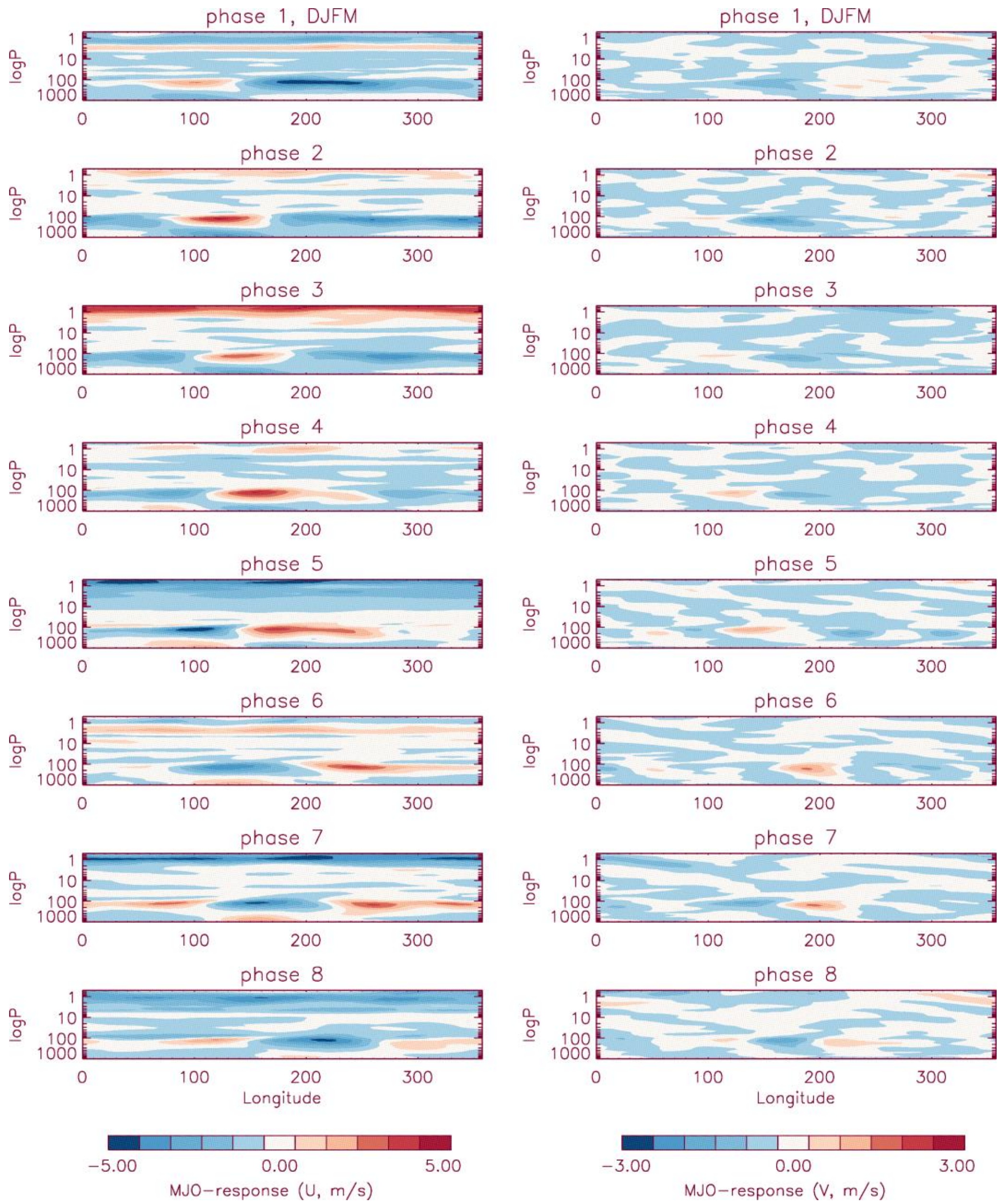

Figure 4.10: Longitudinal structures of the MJO-response in MERRA2 zonal and meridional winds at the stratosphere and troposphere altitudes are shown at each of the MJO-phases. The months used are December-March for years 2008-2010 and the latitudes are averaged between 0-20º S.

One can use the information in Figure 4.10 to further extract the tropo/stratospheric wind filtering effect from the MJO-response in the MLT region tides**.** After the removal of the MJO signals in the horizontal winds (U and V) of MERRA2 data, another SD-WACCMX run with the same configuration as the previously mentioned run (section 4.2.3) but using MERRA2 winds without the MJO is performed from 2008 to 2010. The same 2D fitting process is carried out to extract the temperature tides from this modified model run. For the comparative study of the tidal anomalies, the Hovmoeller analysis uses the same climatology as used in the analysis with the first (unmodified) SD-WACCMX run. The amplitude and phase of the MJO-response in each of the tidal components were obtained with the modified model run using the same methodology discussed above, but the years used for the statistical measure of the MJO-response are 2008-2010. Here, the active-MJO days chosen with the less strict condition (i.e. amp>1 as discussed in section 4.3.1; this is to provide enough data points for the statistical measure of MJO-response).

The amplitudes and phases of the MJO-responses in the modified SD-WACCMX MLT-tides are shown in Figure 4.11 in cyan-color lines along with the MJO-response in the green lines of the unmodified (wind filtering effect not removed) SD-WACCMX MLT-tides. Note that the analysis for the first model run is done using the years 2008-2010 for Figure 4.11, so the green line plots in Figure 4.11 are not same as the green line plots in Figure 4.8 which represent the statistical MJO-response for the years 2004-2017. This is mainly due to interannual variability in the MJO-responses in MLT-tides (not discussed here).

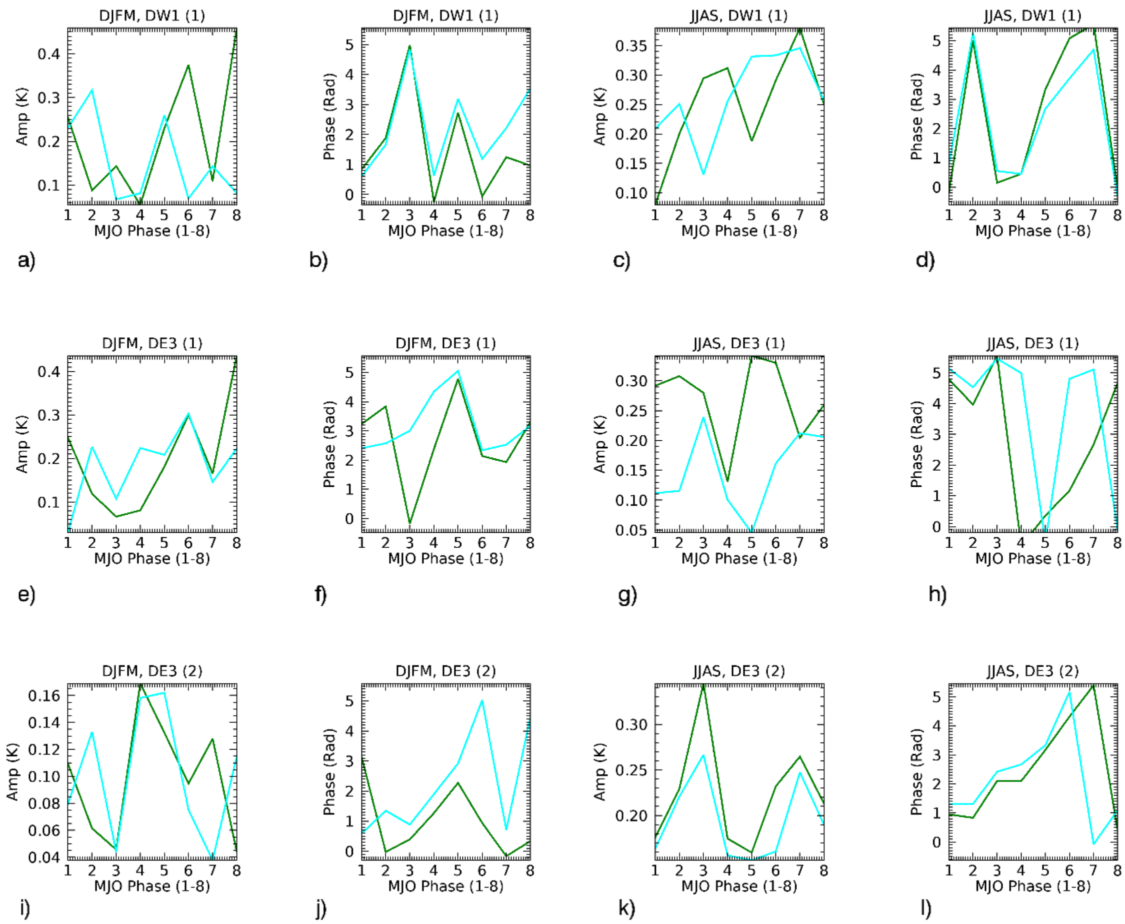

Figure 4.11: Same as Figure 4.8 but the comparison shown is between the two SD-WACCMX model runs using 2008-2010 data. The green lines are for the first model run with MJO while the cyan lines are for the second model run without MJO in winds.

The phases in both seasons for all the tidal components are consistent with the unmodified model runs which indicates that the tropo/stratospheric winds do not considerably change the phase of MJO-response. This means that the inconsistency of the phase of MJO-response between forcing and MLT tides (see previous section 4.3.1) must have been due to wind filtering effect above the stratosphere. The amplitudes of the MJO-responses, however, have small differences from the unmodified model runs. The only exception is that the MJO-response in DE3 decrease significantly in HME1 (Figure 4.11g) and moderately in HME2 (Figure 4.11k) without the wind filtering effect in summer. This could be due to the larger MJO-response in the stratospheric zonal winds during summer months (i.e. larger wind-filtering effect to tides) contributing to the MLT-tidal response, as discussed above using MERRA2 winds. Overall, the small difference in the amplitudes of the MJO response indicates that the wind-filtering effect in the tropo/stratosphere is not the dominant mechanism by which the MJO-response is mapped into the MLT-tides. Therefore, tropospheric radiative and latent tidal forcing in MERRA2 make the most significant contributions to the process by which the MJO response is imprinted on the tides in the MLT.

4.3.3 MJO-Response Carried by the Tidal Momentum Budget in the MLT Region

To understand the underlying physical mechanisms responsible for transmitting the MJO-response in the MLT tides, one can investigate the tidal momentum budget from SD-WACCMX above the stratosphere up to the MLT region in response to the MJO. Note that MERRA2 with the MJO included is used for nudging in SD-WACCMX simulations of tides below ~60 km. For each MJO-phase and season group, one can diagnose the MJO-signal in classical, advection (due to zonal mean winds), and GW-drag (to tides) terms in the zonal and meridional tidal momentum equations:

$$\frac{\partial u'}{\partial t} = fv' - \frac{1}{a\cos\varphi}\frac{\partial \phi'}{\partial \lambda} - \left(\frac{\bar{u}}{a\cos\varphi}\frac{\partial u'}{\partial \lambda} + \frac{v'}{a}\frac{\partial \bar{u}}{\partial \phi}\right) + \frac{\bar{u}v'}{a}\tan\varphi + F_{GWx} + X \qquad [E4.1]$$

$$\frac{\partial v'}{\partial t} = -fu' - \frac{1}{a}\frac{\partial \phi'}{\partial \varphi} - \left(\frac{\bar{u}}{a\cos\varphi}\frac{\partial v'}{\partial \lambda} + \frac{v'}{a}\frac{\partial v'}{\partial \varphi}\right) - \frac{\bar{u}u'}{a}\tan\varphi + F_{GWy} + Y \qquad [E4.2]$$

The first two terms on the right-hand side of the equations E4.1 & E4.2 are the classical tidal terms due to Coriolis force and pressure gradient force. The other terms are nonclassical and describe advection, curvature and GW forcing. X and Y represent the remaining nonconservative mechanical forcing. Following Lu et al. (2012), one can now use the SD-WACCMX data to quantify the relative strengths of the MJO signal in each term of equations E4.1 and E4.2 for the tidal components DW1 and DE3. The tendency term, Coriolis term, pressure gradient term, advection term, curvature term and GW-drag forcing term are first calculated using a centered difference scheme based on the diagnostic outputs of winds, geopotential height and GW-drag forcing. Then each term is decomposed into tidal components by applying the same 2D fitting method as it was used for temperature. By conducting the study as a function of MJO phase and season, it is then determined how individual terms in the tidal momentum budget respond to the MJO in different phases and seasons, and how they contribute to the overall MJO in the MLT-tides.

The MJO-response diagnostics (i.e., Hovmoeller analysis) has been performed on both the zonal and meridional momentum budget corresponding to each of the tidal components. As discussed in Chapter 1 from classical tidal theory, for DW1 zonal and meridional winds, the first dominant mode is the antisymmetric (Hough) mode, while the pair of first and second dominant modes for DE3 zonal winds are the symmetric and antisymmetric modes, and for DE3 meridional winds these are the antisymmetric and symmetric modes, respectively. This corresponds to the MJO-response diagnostics in the tidal DW1(1), DE3(1), and DE3(2) modes in temperature. Here, the MJO-response diagnostics of the individual terms in the momentum budget does not use the HME fitting as there are no HMEs for the tidal momentum equation individual terms. At present, symmetric and antisymmetric modes in each individual term are computed by averaging the MJO-response anomalies (after Hovmoeller analysis) between ±25° latitude as even and odd functions (5°S-25°S for odd modes while 15°N-15°S for even modes). Figure 4.12 exemplifies the amplitude (phases not shown) of the MJO-response in the individual terms in the DW1 zonal wind momentum budget in the MLT region (80-100 km) as a function of MLT altitudes and MJO-phases.

Figure 4.12 shows that classical momentum forcing such as Coriolis and pressure gradient together (Figure 4.12e & 4.12f) represent most features of the MJO response in the zonal momentum budget (Figure 4.12a & 4.12b). Advection and GWD together in (Figure 4.12k & 4.12l) explain most features of the nonclassical momentum forcing (Figure 4.12i & 4.12j) at the MLT altitudes. Note that the advection forcing is larger than the GWD forcing. The seasonal variation from DJFM (winter) to JJAS (summer) of the MJO-response as a function of MJO-phases of each of the individual term follows that of the wind tendencies (Figure 4.12a & 4.12b) such as the enhanced response in MJO-phase 1-4 in DJFM while in phase 5-7 in JJAS. All the individual terms are larger in JJAS than in DJFM which is possibly the reason why there is a bigger tidal MJO-response in JJAS, shown in Figure 4.8. This is interesting as the MJO is more active in winter (DJFM) season and the response in the tides is larger in summer (JJAS). A similar analysis was done for DE3 HME modes (Figure A4-A8 in the Appendix section) which also showed that the advection and GWD are the most important nonclassical forcing term and the advection forcing is larger than the GWD forcing

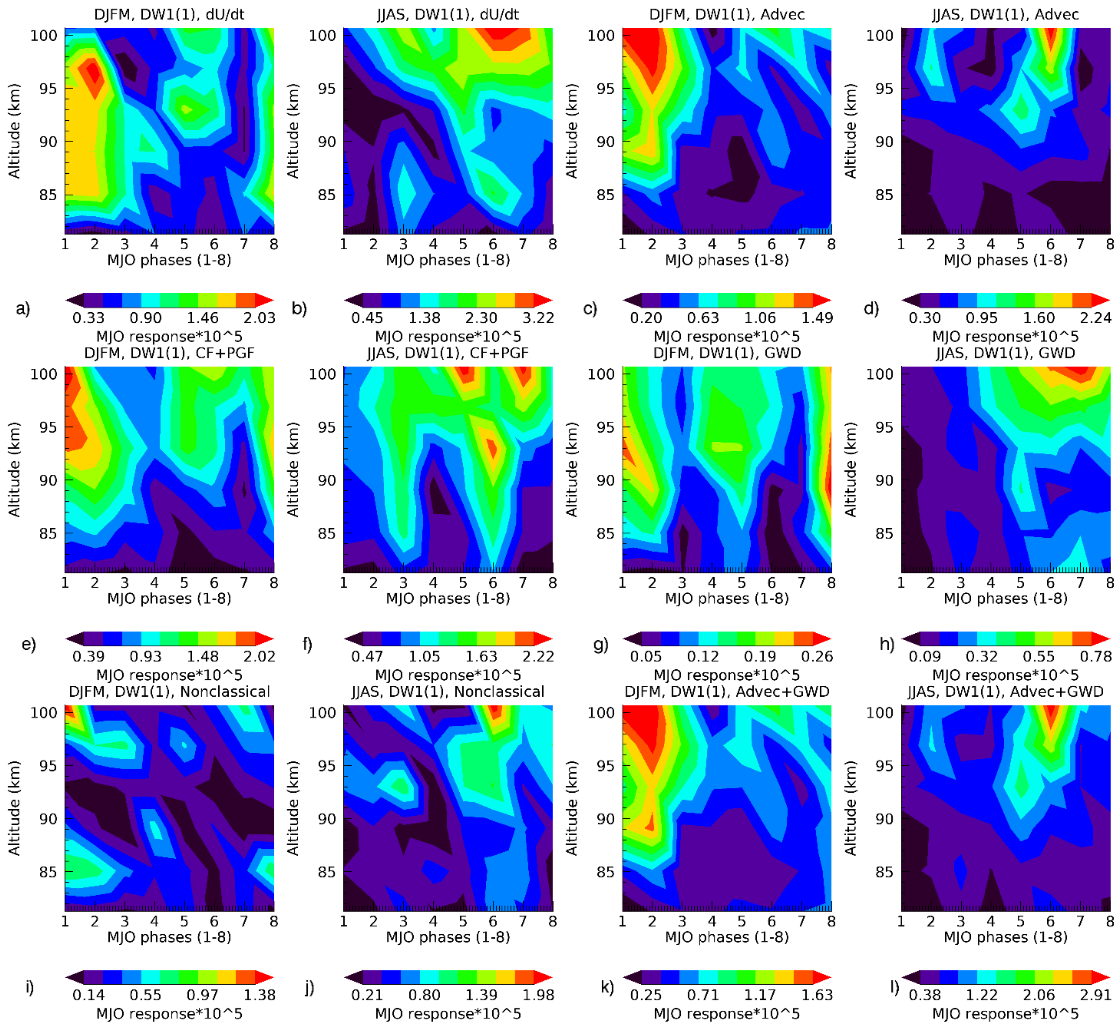

Figure 4.12: Amplitude of the MJO-response in the zonal wind momentum forcing for DW1(1) tidal component in both winter (DJFM) and summer (JJAS) seasons, where the MJO-response is in units of 10^{-5} m/s/s for each of the contour plot and the ranges of response (i.e., colorbars) for each term are different. Nonclassical terms i) & j) represent the difference in a) & b) zonal wind tendencies (dU/dt) and e) & f) classical terms (Coriolis force + pressure gradient force), respectively. The individual nonclassical terms are the advection c) & d) and GWDs g) & h). Advection and GWD together at MLT altitudes are shown in k) and l).

Next, the role of nonclassical forcings such as advection and GWD needs to be discussed in the zonal and meridional wind momentum budget for all the three tidal components. Figures 4.13 and 4.14 show the comparative analysis between advection (dotted black lines) and GWD (red lines) momentum MJO-forcing (or MJO-response) in all three tidal components at 97 km (same altitude used in the Figure 4.8 for SABER) in zonal and meridional tidal winds, respectively. Basically, the amplitude and phase diagnostics of the MJO-response is performed in advection and GWD forcing which are plotted together in Figure 4.13 for zonal advection and zonal GWD and in Figure 4.14 for meridional advection and meridional GWD. The zonal advection MJO-forcing amplitudes in DE3(1) and DE3(2) are comparable in both seasons while the meridional advection MJO-forcing in DE3(2) decreases in winter along with GWD. Both the advection and GWD MJO-forcing amplitudes are more significant for summer than winter, which possibly explains the smaller MJO-response in SD-WACCMX DE3(2) tidal component in winter than summer (Figure 4.8i & 4.8k). This is surprising since the DE3(2) climatology along with the MJO-activity maximizes in the winter months. However, the MJO-response in SABER DE3(2) is comparable in both seasons which may indicate that the MJO-response in the momentum forcing of DE3(2) during winter months in the SD-WACCMX simulations is underestimated.

As in Figure 4.12, the amplitudes of MJO-forcing in Figures 4.13 and 4.14 show that between advection and GWD, advection is the dominant nonclassical momentum forcing term contributing to the MJO-response in all three tidal components and the role of advection is generally larger in summer than in winter. Also, the overall double peak structure of the MJO-response amplitudes as a function of MJO-phases and its seasonal modulation with respect to MJO-phases 1-4 and 5-7 resembles the modulation of the similar double peak structure in the MJO-response amplitudes in the advection terms as well as the classical terms.

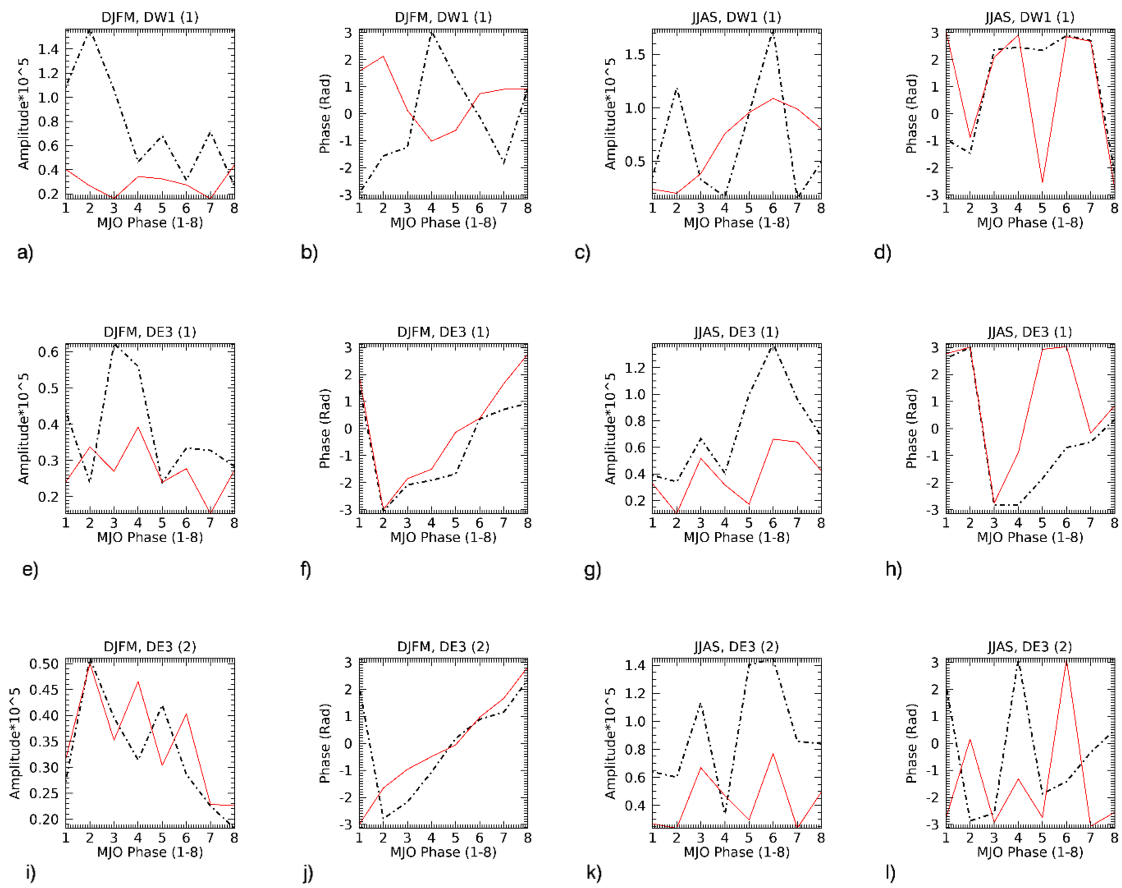

Figure 4.13: The amplitude and phase relationship between advection (dotted black lines) and GWD (red) momentum forcing to a)-d) DW1(1), e)-h) DE3(1), and i)-l) DE3(2) tidal zonal winds are shown in both winter (DJFM) and summer (JJAS) months at 97 km in the MLT region. The amplitude of MJO-response in GWD has been multiplied by 2 for plotting purpose and the unit of amplitude is m/s^2.

The amplitude of MJO-forcing in GWD largely follows the same winter to summer seasonal behavior in advection as a function of MJO-phases. In addition, the double peak structure in the amplitude of the tidal MJO-response as a function of MJO-phases can be seen originated in the MJO-response in radiative/latent forcing, especially in summer

(Figure 4.9), but the seasonal modulation of this peak structure becomes more evident in the MLT region (Figure 4.8).

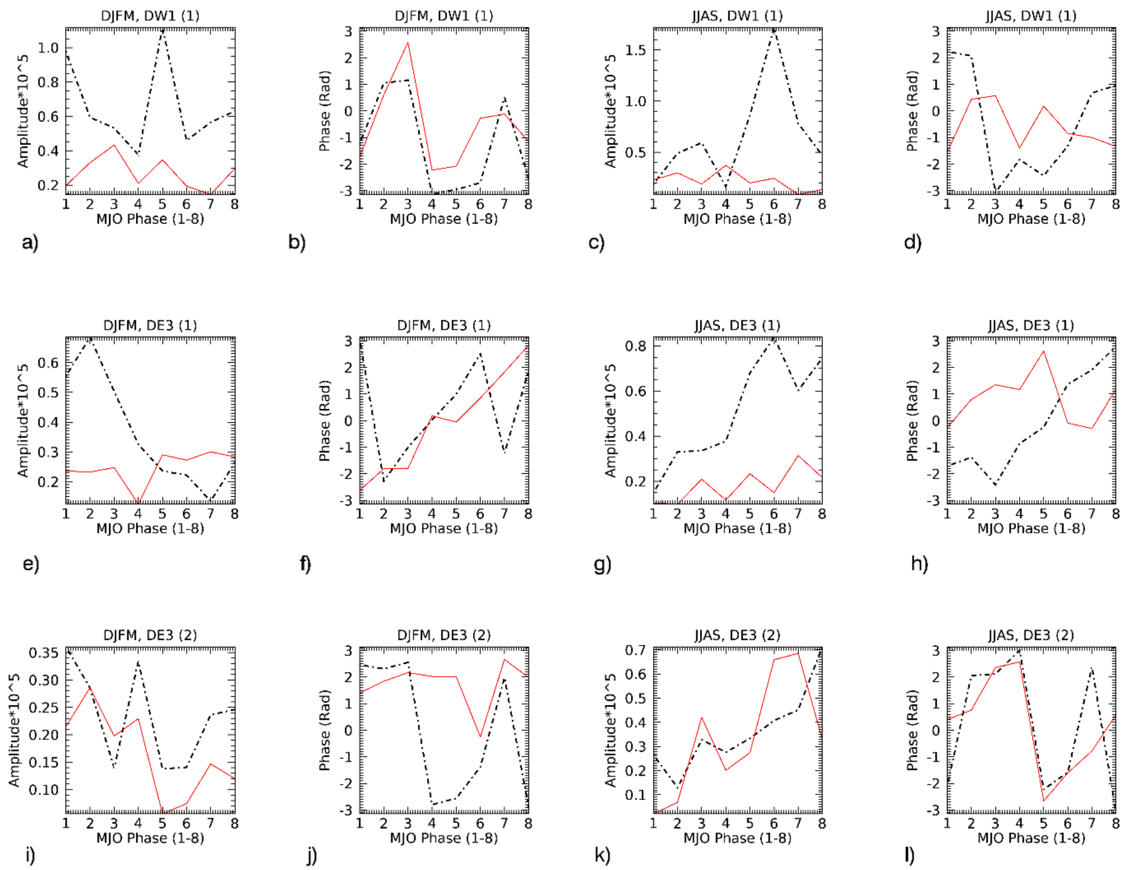

Figure 4.14: Same as Figure 4.13, but for the advection and GWD in the meridional wind momentum budget.

The phase analysis of MJO-response (MJO-forcing) does not show an in-phase relation between advection and GWD forcing in summer. This means that tidal advection and GWD MJO-forcing can work against each other. However, advection is prominently larger than GWD. Briefly, the advection and GWD generally are in-phase for DE3 in winter except the meridional wind advection and GWD for DE3(2) are out-of-phase in winter and in phase in summer. DW1 zonal wind advection and GWD are also in-phase in summer while out-of-phase in winter. Meridional advection in DW1, however, is in-phase with GWD in winter and out-of-phase in summer. The in-phase or out-phase relation between advection and GWD MJO-forcing in zonal and meridional momentum budget is responsible for the difference of phases between forcing and observed MLT tidal MJO-response, as shown in Figure 4.8. Overall, the zonal momentum budget is twice as big as the meridional momentum budget for DE3 tidal components while they are comparable for DW1 tides, and advection and GWD together with Coriolis and pressure gradient force play significant roles in transporting the MJO-response to the tides in the MLT-region.

In summary, SABER and SD-WACCMX diurnal temperature tides in MLT region show a statistically similar response linked to the tropospheric Madden-Julian Oscillation. The important findings are that the tropospheric tidal forcing in radiative and latent heating contributes more significantly in mapping the MJO-response into the tides than the tropo/stratospheric wind-filtering effect. Moreover, Coriolis, pressure gradient, advection and gravity wave drag forcing are the underlying physical mechanisms that imprint the tidal MJO-response above the stratosphere onto the MLT region.

CHAPTER FIVE

CONCLUDING REMARKS

The statistics of the short-term tidal variability derived from "tidal deconvolution" are analyzed using 18 years of diurnal temperature tides observed by the SABER instrument onboard the TIMED satellite. The SABER tidal diagnostics shows tidal variability for the DE3 and DW1 components on interannual, seasonal, and shorter timescales. Such variability is also found to be present in the dominant Hough modes of both tidal components. On interannual timescales, vertically propagating atmospheric tides can be impacted by changes in propagation conditions such as the Quasi-Biennial Oscillation (QBO) and forcing conditions such as the El Niño–Southern Oscillation (ENSO) and the solar cycle. On seasonal timescales, tidal variability mainly consists of forcing variations and the interactions with the mean wind, which may result in higher Hough mode contribution depending on the season in tidal components. Apart from seasonal variations, the results presented in this thesis show that tidal variability on shorter timescales is also impacted by various propagation and forcing conditions. Understanding the causes of short-term variability is important for accurate space weather prediction as the diurnal tidal variability on shorter timescales contributes ~50% to the total variability. Studying the underlying physical mechanisms is not trivial as it can vary for different timescales such as intraseasonal, few weeks, and day-to-day. Tides may vary on intraseasonal timescales as a response to the tropical Madden-Julian oscillation (MJO), while nonlinear wave-wave interactions between tides and planetary waves (PWs) are responsible for tidal variability on timescales from day-to-day to a few weeks. Tidal variability on PW timescales depends on whether tides interact efficiently with PWs, e.g., 5-day, 10-day, 16-day, and 23-day PWs. This thesis looked into how propagation and forcing conditions modulate the day-to-day tidal variability in tides caused by tides-PW interactions, followed by the first observation-based investigation how tidal variability on intraseasonal timescale responds to MJO whereabouts in the tropics and what underlying mechanisms are responsible for such a response.

5.1 Tidal Variability on <30-day/PW Timescale

Tides on various PW timescales can be retrieved by using bandpass filtering on the observed daily tidal timeseries. In this thesis, a new information-theoretic approach based on Bayesian statistics and time-dependent probability density functions followed by multiple linear regression analysis is introduced to study the QBO, ENSO, and solar cycle contributions in the interannual changes in short-term tidal variability on PW timescales observed by SABER. Pattern recognition using information-theoretic KLD diagnostics provides a means to extract statistically significant periodic or recurring variability in the tidal timeseries, which can be further investigated for underlying physical mechanisms using regression analysis. Once the variability features are recognized and studied for all PW timescales as well, they can be used to identify the propagation or forcing conditions in which the short-term tidal variability is largest. More interestingly, one can utilize this extensive methodology to statistically investigate the variabilities in any tidal components on various PW timescales for multiple temporal scales (e.g., intraseasonal, seasonal, intra-annual, and interannual) depending on the temporal resolution of the time series. As tidal variability on 16-day and 23-day timescale ~<5% is much smaller than on a 5-day and 10-

day timescale ~>10%, the analysis is only shown for variability on a 5-day (or quasi-5-day wave, Q5DW) and a 10-day (Q10DW) timescale. The regression analysis helps to explain the causes of interannual changes in the DE3 day-to-day variability on a Q10DW timescale, while it fails to explain the causes of the variability on DW1 on a Q10DW timescale as a function of QBO, ENSO, and solar cycle. Moreover, the results for tidal variability on a Q5DW timescale cannot be explained by regression analysis, as the best regression fit for variability on a Q5DW timescale can only explain up to 20-30% variability characteristics. Therefore, the potential of this methodology has been demonstrated using the DE3 tidal component with its first symmetric (equatorial, HME1) and antisymmetric (nonequatorial, HME2) modes timeseries (2002-2019) on a Q10DW timescale, and the scientific findings are summarized here:

1. Both HME1 (equatorial) and HME2 (nonequatorial) of DE3 show significant interannual changes in tidal variabilities on a Q10DW timescale as a function of QBO, ENSO, and solar cycle.
2. DE3 HME1 variability on a Q10DW timescale is enhanced in the easterly phase of the QBO, caused by HME1-Q10DW interaction in Southern Hemisphere winter, while no response in HME2 variability on a Q10DW timescale is found.
3. DE3 HME1 variability is enhanced during the cold or La Niña phase of ENSO, which is likely due to the enhanced tropospheric tidal forcing during La Niña conditions, while DE3 HME2 variability does not show any response to ENSO.
4. The solar cycle signal in the short-term DE3 HME2 variability, which is likely induced by SSWs (sudden stratospheric warmings) resulting in polar vortex

warming in solar maximum conditions in the westerly QBO, is along the solar cycle-QBO teleconnection effects first explained by Labitzke and van Loon (1988). The lack of a solar cycle response in the DE3 HME1 variability can be explained by a more stable polar vortex in the SH where HME1-Q10DW interactions occur.

An alternative method besides regression fitting needs to be employed in the future to explain the interannual characteristics of day-to-day tidal variability on other PW timescales derived from meanKLD diagnostics. In addition, an analysis of sample lengths shorter than 365-day samples of tidal variability on PW timescales needs to be looked into further, which will provide the characteristics of short-term tidal variability on timescales such as seasonal and intraseasonal, i.e. those shorter than interannual. Moreover, the importance of short-term tidal variability in other tidal components on PW timescales needs to be analyzed in the MLT region and above in the IT region. In the long run, this knowledge will help us to understand how various tidal components and PWs interact in the MLT region and impact the mean state of the IT region. This is especially interesting since future NASA missions such as DYNAMIC and GDC observations will be designed to observe and understand various aspects of global space weather as their sampling will be more frequent than that of the TIMED satellite.

5.2 Tidal Variability on 30-90-Day/Intraseasonal Timescale

SABER observations allow us for the first time to quantify the MLT tidal response to the intraseasonal tropical MJO events and to test model predictions. This is because tropospheric convection associated with the MJO has been known to modulate the intensity of upward-propagating waves. Firstly, this study finds that the intraseasonal variability in both migrating DW1 and nonmigrating DE3 diurnal tides (~10–25% of seasonal mean) have a clear dependence on the location of the MJO, that is, the MJO phase, possibly due to changes in mean wind (and additional MJO-derived gravity waves (GW) forcing) and convective forcing. Interestingly, the MJO effects in both equatorial/nonequatorial modes (HME1&2) of DE3 can be quite different and are possibly related to mode coupling in the lower mesosphere. The nonmigrating DE3(1) tidal response (~25%) to the MJO may be about twice as strong as the migrating DW1(1) tidal response in summer (~8%) and winter (~10%). Moreover, the seasonal variation of the MJO response in nonmigrating tides DE3(1&2) is more prominent than in the migrating tides DW1(1). This is important for space weather research and lower atmosphere coupling on intraseasonal timescales as the MJO is a regularly recurring pattern. This is why this thesis further looked into the MJO-related response within intraseasonal tidal variability to investigate underlying physical mechanisms. The findings for the physical mechanisms that transmit the MJO-response into the MLT diurnal tides can be summarized as follows:

1. The statistical characteristics of the diurnal tidal MJO-response as a function of MJO phases were extracted from Hovmoeller analysis of SABER observations and SD-WACCMX simulations using forcing in the lower atmosphere from MERRA2. Observed and modeled amplitude and phase modulations of the MJO-response as a function of the 8 MJO-phases/locations agree reasonably well with each other.

2. The double peak structure in amplitude of the tidal MJO-response shows seasonal variation from winter to summer as a function of MJO-phases (1-4 & 5-7). In summer, the symmetric components (equatorial mode) of DW1(1) and DE3(1)

show a comparable MJO-response while the antisymmetric component (non-equatorial mode) of DE3(2) shows a smaller MJO-response than the equatorial modes. In winter, when the MJO is more active, the DE3(2) shows a comparable response to DE3(1) and DW1(1). The phase of the MJO response for DE3(2) also varies from winter to summer as a function of MJO-phases and in summer, it is the same as the phase of the MJO-response for DW1.

3. The phase of the MJO-response in radiative and latent heating is generally not consistent with that of the observed MLT tides, while the amplitude modulation of the tidal MJO-response as a function of MJO-phases shows similarities with either latent or radiative forcing or both (in summer) for all tidal components (with double peak structures). The amplitude modulation of the MJO-response in radiative and latent tidal heating is comparable in NH winter and NH summer even if MJO is most active during NH winter season. Additionally, the phases of the MJO-response in latent and radiative tidal heating are generally consistent except for DE3(1). Hence, a connection exists between the MJO-responses in radiative and latent tidal heating and their combined effects explain several characteristics of the MJO-response in MLT tides as a function of MJO-phases.
4. The MJO-response diagnostics in tropo/stratospheric winds from MERRA2 shows a larger response in the zonal winds than in the meridional winds. The tropospheric MJO-signal in zonal wind anomalies shows eastward-propagating enhanced MJO-anomalies with respect to longitudes. Interestingly, the MJO-response in the zonal wind anomalies of the stratosphere shows a longitudinally independent global

signal, which changes eastward to westward depending on MJO-phases/locations. The modified SD-WACCMX run with wind filtering effect removed in the troposphere and stratosphere shows little impact overall on the characteristics of the MJO-response in the unmodified model run. Consequently, tropospheric tidal forcing is more important up to the stratosphere in shaping the modulation of the tidal MJO-response as a function of MJO-phases.

5. The underlying mechanisms responsible for transmitting the MJO-response from the stratosphere to the MLT region are the nonclassical forcing mechanisms including advection due to background winds and gravity wave drag (GWD) as well as the classical mechanisms Coriolis and pressure gradient force. The seasonal modulation in the amplitudes of the tidal MJO response is the same as the seasonal oscillation of the MJO-response in zonal and meridional MLT winds (momentum budget). The zonal wind momentum forcing is twice as big as the meridional wind momentum forcing. Advection forcing is the most dominant nonclassical forcing among advection and GWD and is larger in the summer season than in the winter, which also resembles the overall MJO-response in the MLT tides. The advection and GWD can work together or against each other, depending on their phase relationship with respect to the MJO-phases in a given season.

5.3 Outlook

Altogether, the PW and MJO driven tidal variations and findings are important as tides can couple the response on PWs and MJO timescales in the MLT region to the IT region through E-dynamo processes. For example, NASA's Living with a Star program explicitly calls out “ionospheric variability with known meteorological events (e.g., SSWs, the MJO, tropical cyclones, gravity wave hotspots)”; and “longitudinal dependence of ionospheric variability due to combined effects of planetary waves and tides” as Focused Science Topic (FST) #1 top priorities in understanding space weather. The results presented in this thesis are also important for the recently launched ICON mission as well as the future NASA GDC and DYNAMIC satellite constellation missions that are currently being implemented, with anticipated 2027 launch date. GDC and DYNAMIC will accomplish breakthroughs in fundamental understanding of the processes that govern the dynamics of the Earth's upper atmospheric envelope by measuring the neutral and plasma from a satellite constellation perspective, to finally resolve space/time ambiguities that are inherent in single satellite observations, an exciting opportunity for the time to come.

APPENDIX

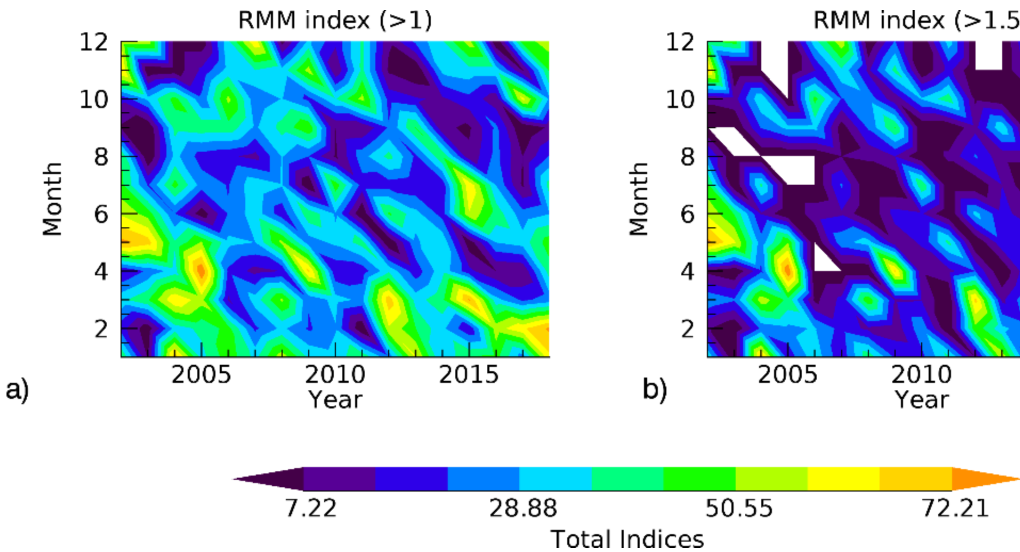

Figure A1: Monthly (y-axis) distribution of total(sum) RMM indices (amp) for the MJO active condition during 2002-2018 (x-axis), where a) RMM indices>1 and b) RMM indices>1.5 for 5 consecutive days is used for active-MJO condition.

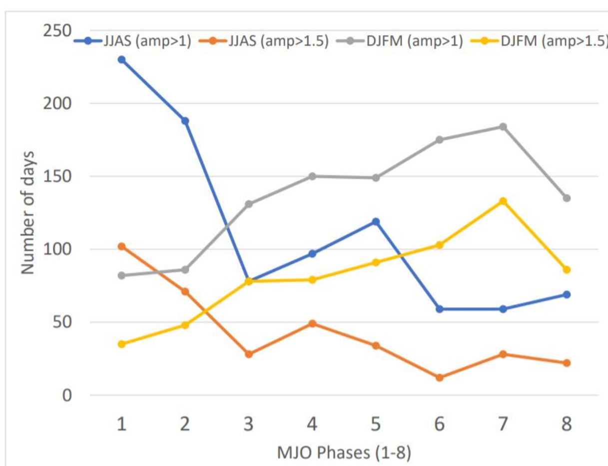

Figure A2: Number of active-MJO days for winter (DJFM) and summer (JJAS) seasons in each MJO-phase/bin and for different active-MJO conditions (amp>1 or amp>1.5).

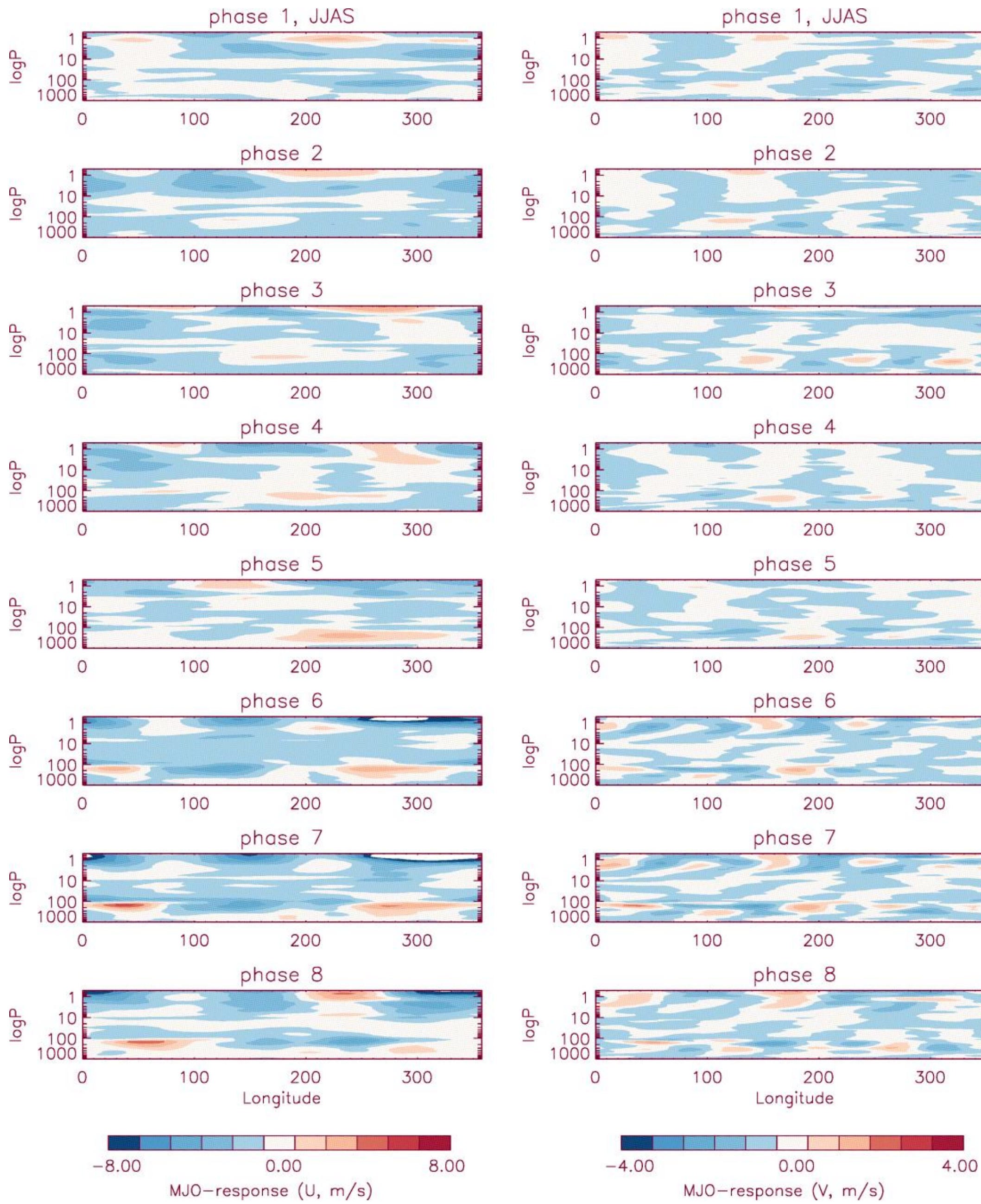

Figure A3: Same as Figure 4.10, but for June-September months.

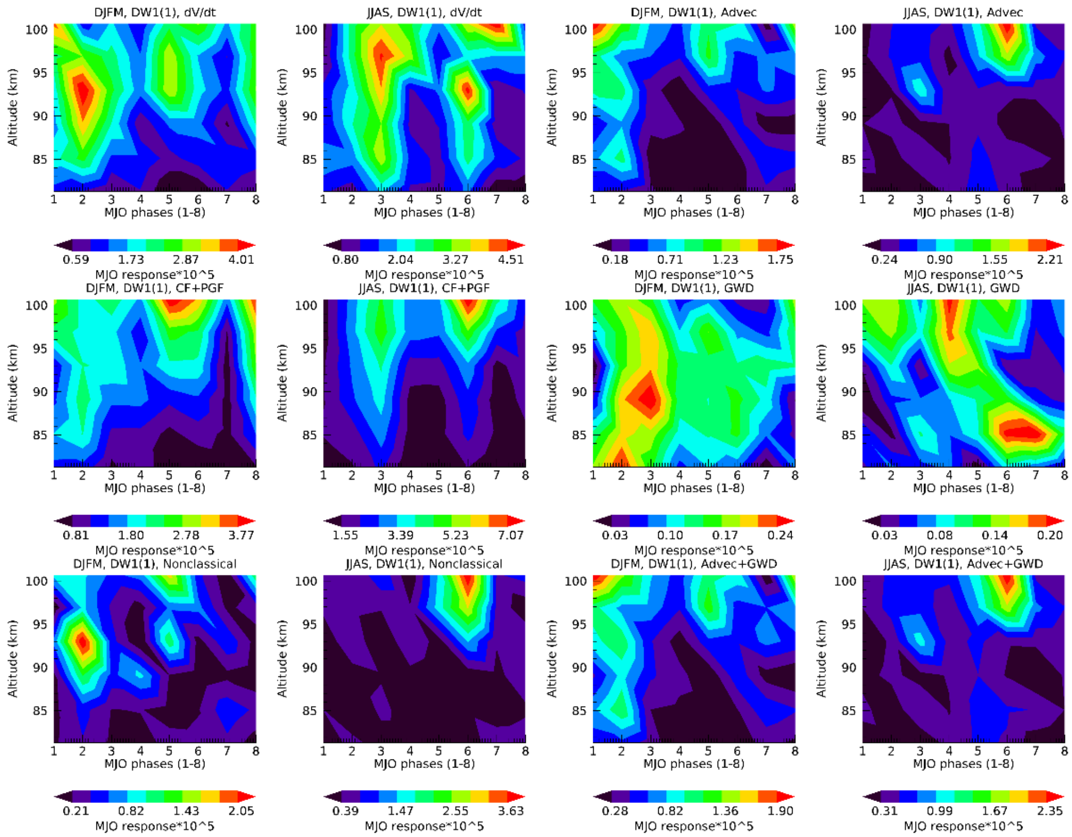

Figure A4: Same as Figure 4.12, but for DW1(1) meridional wind momentum budget.

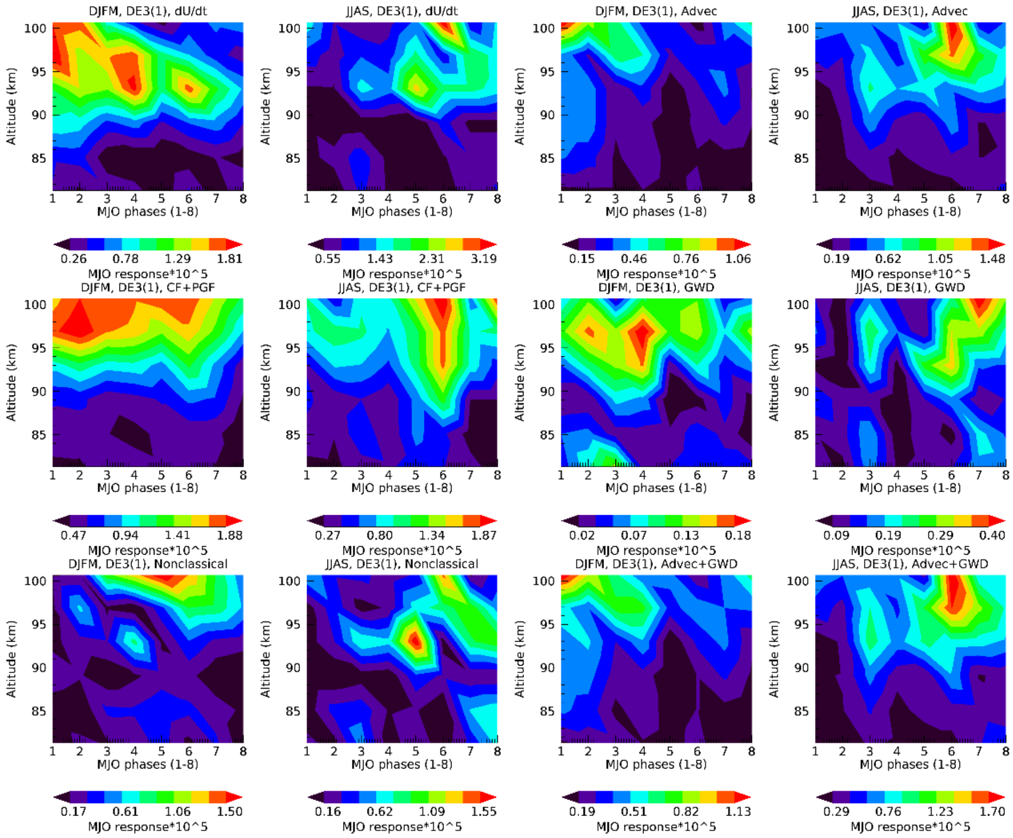

Figure A5: Same as Figure 4.12, but for DE3(1) zonal wind momentum budget

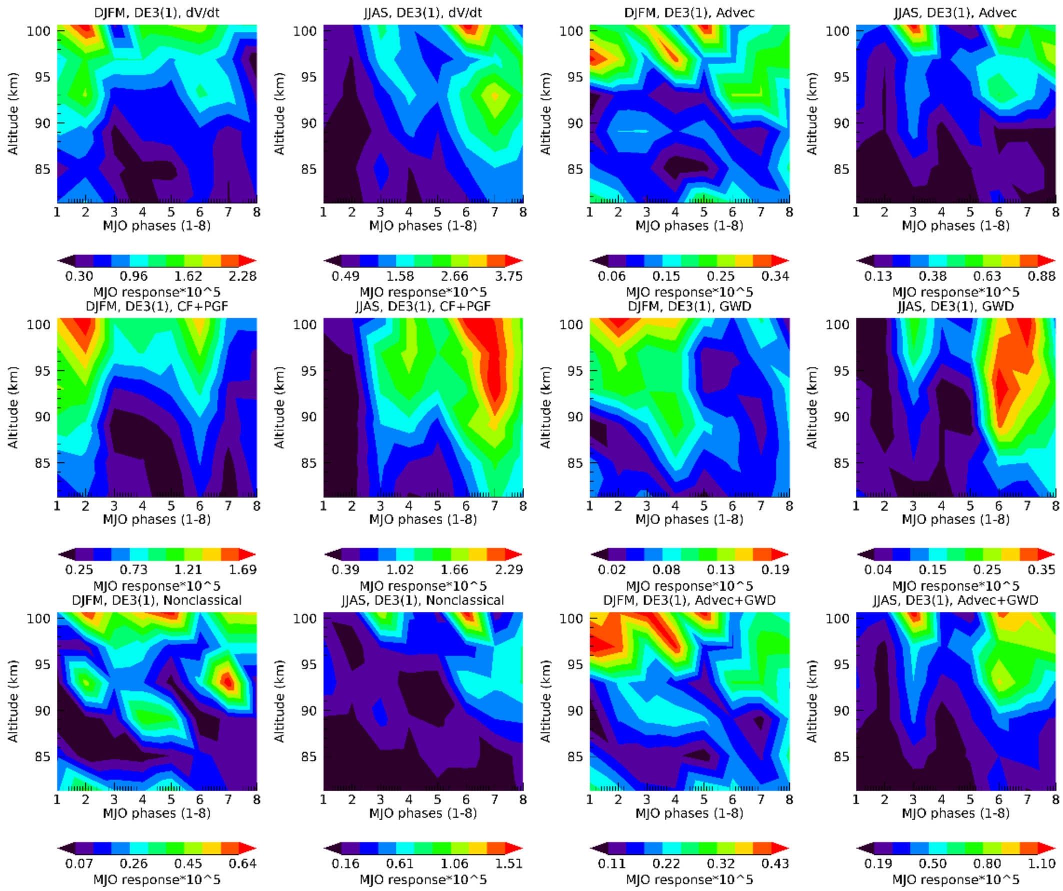

Figure A6: Same as Figure 4.12, but for DE3(1) meridional wind momentum budget

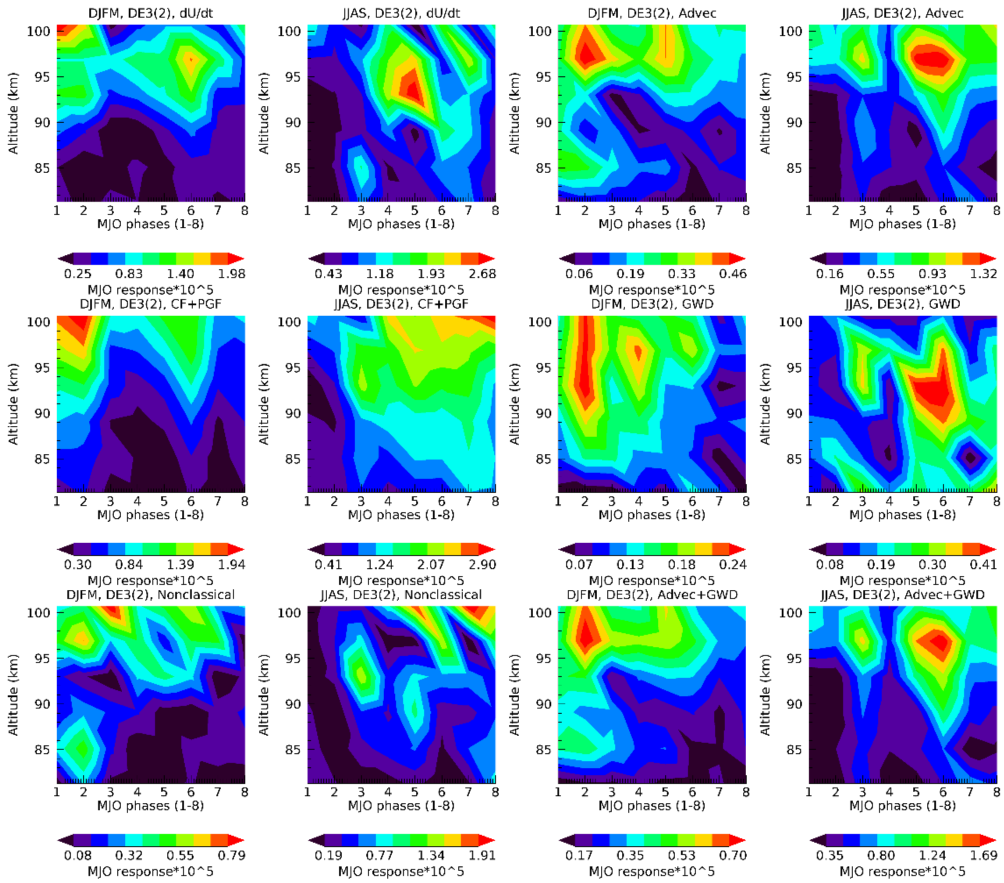

Figure A7: Same as Figure 4.12, but for DE3(2) zonal wind momentum budget

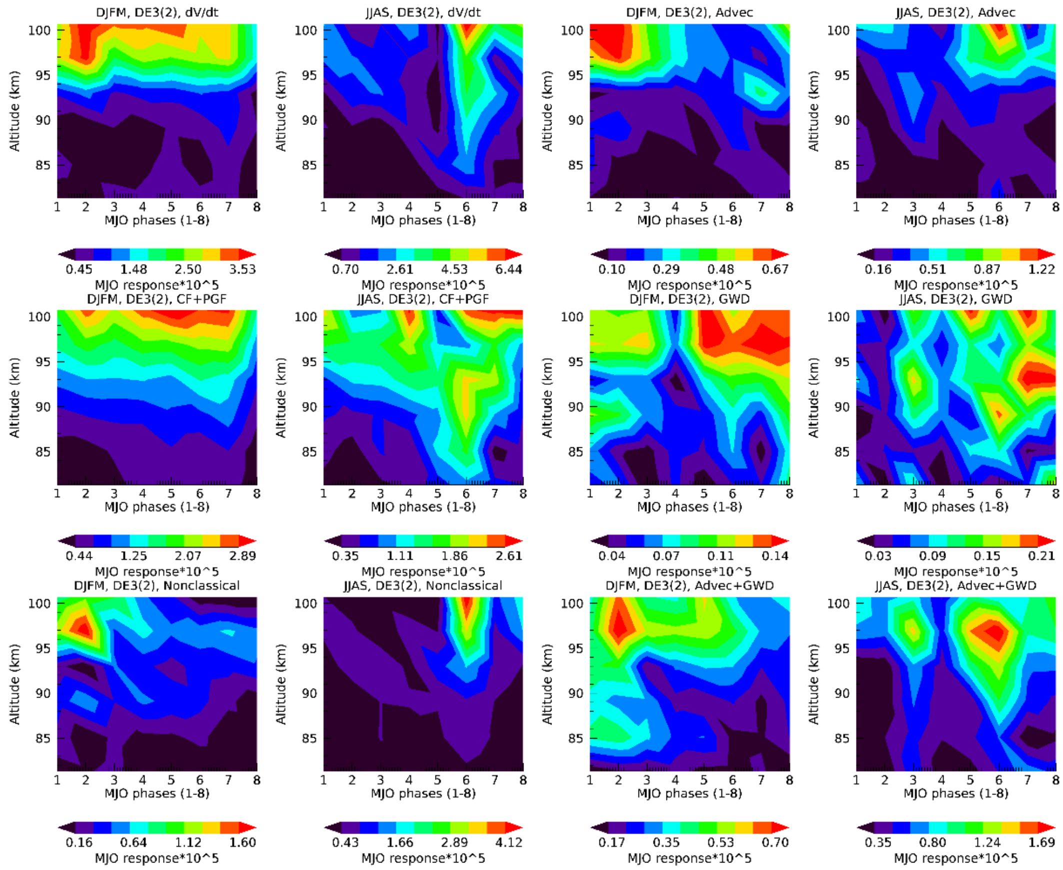

Figure A8: Same as Figure 4.12, but for DE3(2) meridional wind momentum budget

REFERENCES

- Agner, R., & Liu, A. Z. (2015). Local time variation of gravity wave momentum fluxes and their relationship with the tides derived from LIDAR measurements. *Journal of Atmospheric and Solar-Terrestrial Physics, 135*, 136–142. https://doi.org/10.1016/j.jastp.2015.10.018.

- Akmaev, R. A., & Fomichev, V. I. (1998). Cooling of the mesosphere and lower thermosphere due to doubling of CO. *Annales Geophysicae, 16*(11), 1501. https://doi.org/10.1007/s005850050715.

- Akmaev, R. A., (2008). On the energetics of maximum-entropy temperature profiles. *Q. J. R. Meteorol. Soc., 134*, pp. 187-197, 10.1002/qj.209.

- Alexander, M. J., Grimsdell, A. W., Stephan, C. C., & Hoffmann, L. (2018). MJO-related intraseasonal variation in the stratosphere: gravity waves and zonal winds. *Journal of Geophysical Research: Atmospheres, 123*(2), 775–788. https://doi.org/10.1002/2017JD027620.

- Andrews, D. G., Leovy, C. B., & Holton, J. R. (1987). Middle atmosphere dynamics (Vol. 40). New York, NY, USA.: Academic press.

- Angelats I Coll, M., & Forbes, J. M. (2002). Nonlinear interactions in the upper atmosphere: The s = 1 and s = 3 nonmigrating semidiurnal tides. Journal of *Geophysical Research: Space Physics, 107*(A8), 1–15. https://doi.org/10.1029/2001JA900179

- Beard, G. A., Mitchell, N.J., Williams, P. J. S., & Kunitake, M. (1999). Non-linear interactions between tides and planetary were resulting in periodic tidal variability. *J. Atmos. Sol.-Terr. Phys., 61*, pp. 363-376

- Bernard, R., (1981). Variability of the semi-diurnal tide in the upper mesosphere. *J. Atmos. Terr. Phys., 43*, pp. 663-674

- Bremer, J., Schminder, R., Greisiger, K. M., Hoffmann, P., Kurschner, D., & Singer, W., (1997). Solar cycle dependence and long-term trends in the wind field of the mesosphere lower thermosphere. *J. Atmos. Sol. Terr. Phys., 59*, 497–509, doi:10.1016/S1364-6826(96)00032-6.

- Burrage, M. D., Hagan, M. E., Skinner, W. R., Wu, D. L., & Hays, P. B., (1995). Long-term variability in the solar diurnal tide observed by HRDI and simulated by the GSWM. *Geophys. Res. Lett., 22*(19), 2641–2644.

- Camp, C. D., & Tung, K. K. (2007). The influence of the solar cycle and QBO on the late-winter stratospheric polar vortex. *Journal of the Atmospheric Sciences, 64*(4), 1267–1283. https://doi.org/10.1175/JAS3883.1

- Chapman, S. & Lindzen, R. S. (1970). Atmospheric Tides. D. Reidel, Dor-drecht, Netherlands.

- Chang, L. C., Palo, S. E., & Liu, H. L. (2009). Short-term variation of the s = 1 nonmigrating semidiurnal tide during the 2002 stratospheric sudden warming. *J. Geophys. Res., 114*, D03109, doi:10.1029/2008JD010886

- Chang, L. C., Palo, S. E., & Liu, H. L. (2011). Short-term variability in the migrating diurnal tide caused by interactions with the quasi 2-day wave. *Journal of Geophysical Research Atmospheres, 116*(12), 1–18. https://doi.org/10.1029/2010JD014996.

- Cover, T. M. & Thomas, J. A. (2006). Elements of Information Theory. 2nd ed (New York: Wiley-Interscience).

- Dhadly, M. S., Emmert, J. T., Drob, D. P., McCormack, J. P., & Niciejewski, R. J. (2018). Short-Term and Interannual Variations of Migrating Diurnal and Semidiurnal Tides in the Mesosphere and Lower Thermosphere. *Journal of Geophysical Research: Space Physics, 123*(8), 7106–7123. https://doi.org/10.1029/2018JA025748

- Duchon, C. E. (1979). Lanczos filtering in one and two dimensions. *Journal of Applied Meteorology, 18*(8), 1016–1022. https://doi.org/10.1175/1520-0450(1979)018<1016:LFIOAT>2.0.CO;2.

- Eckermann, S. D., Rajopadhyaya, D. K., & Vincent, R. A. (1997). Intraseasonal wind variability in the equatorial mesosphere and lower thermosphere: Long-term observations from the central Pacific. *Journal of Atmospheric and Solar-Terrestrial Physics, 59*(6 SPEC. ISS.), 603–627. https://doi.org/10.1016/s1364-6826(96)00143-5

- Ekanayake, E. M. P., Aso, T., & Miyahara, S. (1997). Background wind effect on propagation of nonmigrating diurnal tides in the middle atmosphere. *Journal of Atmospheric and Solar-Terrestrial Physics, 59*(4), 401–429. https://doi.org/10.1016/S1364-6826(96)00012-0

- Forbes, J. M. (1995). Tidal and planetary waves, in the upper mesosphere and lower thermosphere: a review of experiment and theory. *Geophys. Monogr. Ser.*, vol. 87, edited by R. M. Johnson and T. L. Killeen, pp. 67 – 87, AGU, Washington, D. C.

- Forbes, J. M., Bruinsma, S. L., Zhang, X., & Oberheide, J. (2009). Surface exosphere coupling due to thermal tides. *Geophys. Res. Lett., 36*, L15812, doi:10.1029/2009GL038748.

- Forbes, J. M., & Garrett, H. B. (1979). Theoretical studies of atmospheric tides. *Rev. Geophys., 17,* 1951-1981.

- Forbes, J. M. & Hagan, M. E. (1988). Diurnal propagating tides in the presence of mean winds and dissipation: a numerical investigation. *Planet. Space Sci., 36*, 579.

- Forbes, J. M. & Hagan, M. E. (1979). Tides in the joint presence of friction and rotation: an f plane approximation. *J. geophys. Res. 84,* 803.

- Forbes, J. M., & Lindzen, R. S. (1976). Atmospheric solar tides and their electrodynamic effects - II. The equatorial electrojet. *Journal of Atmospheric and Terrestrial Physics, 38*, 911– 920. https://doi.org/10.1016/0021-9169(76)90074-X

- Forbes, J. M., & Lindzen, R. S. (1977). Atmospheric solar tides and their electrodynamic effects - III. The polarization electric field. *Journal of Atmospheric and Terrestrial Physics, 39*, 1369– 1377. https://doi.org/10.1016/0021-9169(77)90090-3

- Forbes, J. M., Palo, S. E., & Zhang, X., (2000). Variability of the ionosphere. *J. Atmos. Sol. -Terr. Phys., 62*, 685, doi:10.1016/S1364-6826(00)00029-8

- Forbes, J. M., & Vincent, R. C. (1989). Effects of mean winds and dissipation on the diurnal propagating tide: An analytic approach. *Planet. Space Sci., 37*(2), 197–209. https://doi.org/10.1016/0032-0633(89)90007-X

- Forbes, J. M., & Wu, D. (2006). Solar tides as revealed by measurements of mesosphere temperature by the MLS experiment on UARS. *Journal of the Atmospheric Sciences, 63*(7), 1776–1797. https://doi.org/10.1175/JAS3724.1

- Forbes, J. M., & Zhang, X. (2015). Quasi-10-day wave in the atmosphere. *J. geophys. Res, 120*(21), 11,079-11,089. https://doi.org/10.1002/2015JD023327

- Forbes, J. M., Zhang, X., Palo, S., Russell, J., Mertens, C. J., & Mlynczak, M. (2008). Tidal variability in the ionospheric dynamo region. *J. Geophys. Res., 113*, 02,310, doi:10.1029/2007JA012737.

- Forbes, J. M., Zhang, X., Talaat, E. R., & Ward, W. (2003). Nonmigrating diurnal tides in the thermosphere. *J. geophys. Res*: *Space Physics, 108*(A1), 1–10. https://doi.org/10.1029/2002JA009262

- Fraser, G. J., Vincent, R. A, Manson, A. H., Meek, C. K., & Clark, R. R. (1989). Inter-annual variability of tides in the mesosphere and lower thermosphere. *J. Atmos. Terr. Phys., 51*, 555–567, doi:10.1016/0021-9169 (89)90054-8.

- Fritts, D. C. & Isler, J. R. (1994). Mean motions and tidal and two-day structure and variability in the mesosphere and lower thermosphere over Hawaii. *J. Atmos. Sci., 51*(14), 2145–2164.

- Fritts, D. C. & Vincent. R. A. (1987). Mesospheric momentum flux studies at Adelaide, Australia: observations and a gravity wave/tidal interaction model. *J. atmos. Sci. 44*, 60.

- Gan, Q., Oberheide, J., Yue, J., & Wang, W. (2017). Short-term variability in the ionosphere due to the nonlinear interaction between the 6-day wave and migrating tides. *Journal of Geophysical Research: Space Physics, 122*(8), 8831–8846. https://doi.org/10.1002/2017JA023947.

- Garcia, R. R. (2000). The role of equatorial waves in the semiannual oscillation of the middle atmosphere. In Atmospheric science across the stratopause, *Geophysical Monograph Series (Vol. 123, pp. 161–176).* Washington, DC: American Geophysical Union. https://doi.org/ 10.1029/GM123p0161

- García-Herrera, R., Calvo, N., Garcia, R. R., & Giorgetta, M. A. (2006). Propagation of ENSO temperature signals into the middle atmosphere: A comparison of two general circulation models and ERA-40 reanalysis data. *Journal of Geophysical Research Atmospheres, 111*(6), 1–14. https://doi.org/10.1029/2005JD006061

- Gasperini, F., Hagan, M. E., & Zhao, Y. (2017). Evidence of Tropospheric 90 Day Oscillations in the Thermosphere. *Geophysical Research Letters, 44*(20), 10,125-10,133. https://doi.org/10.1002/2017GL075445

- Gasperini, Federico, Liu, H., & Mcinerney, J. (2020). Preliminary Evidence of Madden-Julian Oscillation Effects on Ultra-Fast Tropical Waves in the Thermosphere. 1–47. https://doi.org/10.1029/2019JA027649.

- Gelaro, R., McCarty, W., Suárez, M. J., Todling, R., Molod, A., Takacs, L., Randles, C. A., Darmenov, A., Bosilovich, M. G., Reichle, R., Wargan, K., Coy, L., Cullather, R., Draper, C., Akella, S., Buchard, V., Conaty, A., da Silva, A. M., Gu, W., … Zhao, B. (2017). The modern-era retrospective analysis for research and applications, version 2 (MERRA-2). *Journal of Climate, 30*(14), 5419–5454. https://doi.org/10.1175/JCLI-D-16-0758.1

- Gurubaran, S., Rajaram, R., Nakamura, T., & Tsuda, T. (2005). Interannual variability of diurnal tide in the tropical mesopause region: A signature of the El Nino-Southern Oscillation (ENSO). *Geophysical Research Letters, 32*(13), 1–4. https://doi.org/10.1029/2005GL022928

- Gurubaran, S., Rajaram, R., Nakamura, T. *et al.* (2009). Radar observations of the diurnal tide in the tropical mesosphere-lower thermosphere region: Longitudinal variabilities. *Earth Planet Sp, 61*, 513–524. https://doi.org/10.1186/BF03353168

- Hagan, M. E., Chang, J. L., & Avery, S. K. (1997). Global-scale wave model estimates of nonmigrating tidal effects. *Journal of Geophysical Research Atmospheres, 102*(14), 16439–16452.

- Hagan, M. E., & Forbes, J. M. (2002). Migrating and nonmigrating diurnal tides in the middle and upper atmosphere excited by tropospheric latent heat release. *Journal of Geophysical Research Atmospheres, 107*(24), 1–15. https://doi.org/10.1029/2001JD001236

- Hagan, M. E., & Roble, R. G. (2001). Modeling diurnal tidal variability with the National Center for Atmospheric Research thermosphere-ionosphere-mesosphere-electrodynamics general circulation model. *Journal of Geophysical Research: Space Physics, 106*(A11), 24869–24882. https://doi.org/10.1029/2001ja000057

- Hausler, K., Luhr, H., Hagan, M. E., Maute, A., & R. G. Roble (2010). Comparison of CHAMP and TIME-GCM nonmigrating tidal signals in the thermospheric zonal wind. *J. Geophys. Res., 115*, D00I08, doi:10.1029/2009JD012394.

- Hlaváčková-Schindler, K., Paluš, M., Vejmelka, M., & Bhattacharya, J. (2007). Causality detection based on information-theoretic approaches in time series analysis. *Physics Reports, 441*(1), 1–46. https://doi.org/10.1016/j.physrep.2006.12.004

- Hough, S. S. (1898). On the application of harmonic analysis o the dynamical theory of tides. II: On the general integration of Laplace's dynamical equations. *Philosophical Transactions of the Royal Society of London. Series A, 191*(0), 139–185. https://doi.org/10.1098/ rsta.1898.0005

- Immel, T. J., Sagawa, E., England, S. L., Henderson, S. B., Hagan, M. E., Mende, S. B., Frey, H. U., Swenson, C. M., & Paxton, L. J. (2006). Control of equatorial ionospheric morphology by atmospheric tides. *Geophysical Research Letters, 33*(15), 2–5. https://doi.org/10.1029/2006GL026161.

- Immel, T. J., Mende, S. B., Hagan, M. E., Kintner, P. M., & England, S. L. (2009). Evidence of tropospheric effects on the ionosphere. *Eos, 90*(9), 69–70. https://doi.org/10.1029/2009EO090001.

- Isoda, F., Tsuda, T., Nakamura, T., Vincent, R. A., Reid, I. M., Achamd, E., Sadewo, A., & Nuryanto, A. (2004). Intraseasonal oscillations of the zonal wind near the mesopause observed with medium-frequency and meteor radars in the tropics. *Journal of Geophysical Research: Atmospheres, 109*(21), 35–40. https://doi.org/10.1029/2003JD003378

- Jones, M., Forbes, J. M., & Hagan, M. E. (2016). Solar cycle variability in mean thermospheric composition and temperature induced by atmospheric tides. *Journal of Geophysical Research: Space Physics, 121*(6), 5837–5855. https://doi.org/10.1002/2016JA022701

- Jones, M., Forbes, J. M., Hagan, M. E., & Maute, A. (2014). Impacts of vertically propagating tides on the mean state of the ionosphere-thermosphere system. *Journal of Geophysical Research: Space Physics, 119*(3), 2197–2213. https://doi.org/10.1002/2013JA019744.

- Jones, M., Forbes, J. M., & Sassi, F. (2019). The Effects of Vertically Propagating Tides on the Mean Dynamical Structure of the Lower Thermosphere. *Journal of Geophysical Research: Space Physics, 124*(8), 7202–7219. https://doi.org/10.1029/2019JA026934.

- Kato, S., Tsuda, T., & Wantanabe, F. (1982), Thermal excitation of non-migrating tides, *J. Atmos. Terr. Phys., 44*, 131 – 146.

- Khattatov, B. V. (1996). Dynamics of the mesosphere and lower thermosphere as seen by MF radars and by the high-resolution Doppler imager/UARS. *Journal of Geophysical Research Atmospheres, 101*(D6), 10393–10404. https://doi.org/10.1029/95JD01704

- Killeen, T. L., Wu, Q., Solomon, S. C., Ortland, D. A., Skinner, W. R., Niciejewski, R. J., & Gell, D. A. (2006). TIMED Doppler Interferometer: Overview and recent results. *Journal of Geophysical Research: Space Physics, 111*(10), 1–19. https://doi.org/10.1029/2005JA011484

- Knuth, K. H. (2006). Optimal data-based binning for histograms, *2*(1). Retrieved from http://arxiv.org/abs/physics/0605197

- Knuth, K. H., et al. (2005). Revealing relationships among relevant climate variables with information theory. *Earth-Sun System Technology Conference*, NASA, Adelphi, Md.

- Kumar, K., G., Singer, W., Oberheide, J., Grieger, N., Batista, P. P., Riggin, D. M., et al. (2014). Diurnal tides at low latitudes: Radar, satellite, and model results. *Journal of Atmospheric and Solar-Terrestrial Physics, 118*, 96–105. https://doi.org/10.1016/j.jastp.2013.07.005.

- Kumar, K. K., Antonita, T. M., Ramkumar, G., Deepa, V., Gurubaran, S., & Rajaram, R. (2007). On the tropospheric origin of Mesosphere Lower Thermosphere region intraseasonal wind variability. *Journal of Geophysical Research Atmospheres, 112*(7), 1–8. https://doi.org/10.1029/2006JD007962.

- Kumari, K., & Oberheide, J. (2020). QBO, ENSO, and solar cycle effects in short-term nonmigrating tidal variability on planetary wave timescales from SABER—An information-theoretic approach. *Journal of Geophysical Research: Atmospheres, 125*(6), 1–23. https://doi.org/10.1029/2019JD031910

- Kumari, K., Oberheide, J., & Lu, X. (2020). The Tidal Response in the Mesosphere/Lower Thermosphere to the Madden-Julian Oscillation Observed by SABER. *Geophysical Research Letters, 47*(16). https://doi.org/10.1029/2020GL089172

- Kumari, K., Wu, H., Long, A., Lu, X., & Oberheide, J. (2021). Mechanism studies of Madden-Julian-Oscillation coupling into the Mesosphere/Lower Thermosphere tides using SABER, MERRA2 and SD-WACCMX. *J. Geophys. Res. Atmos.,* 2021JD034595, submitted.

- Labitzke, K. (1982). On the Interannual Variability of the Middle Stratosphere during the Northern Winters. *Journal of the Meteorological Society of Japan. Ser. II, 60*(1), 124–139. https://doi.org/10.2151/jmsj1965.60.1_124

- Labitzke, K., & Loon, H. Van. (1988). Associations between the 11-year solar cycle, the QBO and the atmosphere. Part I: the troposphere and stratosphere in the northern hemisphere in winter. *Journal of Atmospheric and Terrestrial Physics.* https://doi.org/10.1016/0021-9169(88)90068-2

- Laplace, P. S. (1799). Mechanique Celeste, Paris.

- Larson, J. W. (2010). Can we define climate using information theory? *IOP Conference Series: Earth and Environmental Science, 11*, 012028. https://doi.org/10.1088/1755-1315/11/1/012028

- Larson, J. W. (2012). Visualizing climate variability with time-dependent probability density functions, detecting it using information theory. *Procedia Computer Science, 9*(1), 917–926. https://doi.org/10.1016/j.procs.2012.04.098

- Leonard, J. M., Forbes, J. M., & Born, G. H. (2012). Impact of tidal density variability on orbital and reentry predictions. *Space Weather, 10*(12), 1–12. https://doi.org/10.1029/2012SW000842

- Li, J., & Lu, X. (2020). SABER observations of gravity wave responses to the Madden-Julian Oscillation from the stratosphere to the lower thermosphere in tropics and extratropics. *Geophysical Research Letters, 47*(23). https://doi.org/10.1029/2020gl091014

- Lieberman, R. S., (1991). Nonmigrating diurnal tides in the equatorial middle atmosphere. *J. Atmos. Sci.,48*, 1112–1123.

- Lieberman, R. S. (1998). Intraseasonal variability of high-resolution Doppler imager winds in the equatorial mesosphere and lower thermosphere. *Journal of Geophysical Research, 103*(D10), 11,221–11,228. https://doi.org/10.1029/98JD00532.

- Lieberman, R. S., Oberheide, J., Hagan, M. E., Remsberg, E. E., & Gordley, L. L. (2004). Variability of diurnal tides and planetary waves during November 1978-May 1979. *Journal of Atmospheric and Solar-Terrestrial Physics, 66*(6–9), 517–528. https://doi.org/10.1016/j.jastp.2004.01.006.

- Lieberman, R. S., Oberheide, J., & Talaat, E. R. (2013). Nonmigrating diurnal tides observed in global thermospheric winds. *Journal of Geophysical Research: Space Physics, 118*(11), 7384–7397. https://doi.org/10.1002/2013JA018975

- Lieberman, R. S., Riggin, D. M., Ortland, D. A., Oberheide, J., & Siskind, D. E. (2015). Global observations and modeling of nonmigrating diurnal tides generated by tide-planetary wave interactions. *Journal of Geophysical Research, 120*(22), 11,419-11,437. https://doi.org/10.1002/2015JD023739

- Lieberman, R. S., Riggin, D. M., Ortland, D. A., Nesbitt, S. W., & Vincent, R. A. (2007). Variability of mesospheric diurnal tides and tropospheric diurnal heating during 1997-1998. *Journal of Geophysical Research Atmospheres, 112*(20), 1–17. https://doi.org/10.1029/2007JD008578

- Lindzen, R. S. (1971). Internal gravity waves in atmospheres with realistic dissipation and temperature., *Geophys. Fluid Dyn., 2*, 89-121, 1971.

- Lindzen, R.S. & Hong. S. S. (1974). Effects of mean winds and horizontal temperature gradients on solar and lunar semidiurnal tides in the atmosphere. *J. Atmos. Sci. 31*. 1421.

- Lindzen, R. S., Hong, S. S., & Forbes, J. M. (1977). Semidiurnal hough mode extensions in the thermosphere and their application. *Memo. Rep. 3442*, Nav. Res. Lab., Washington, D.C.

- Liu, A. Z., Lu, X., & Franke, S. J. (2013). Diurnal variation of gravity wave momentum flux and its forcing on the diurnal tide. *Journal of Geophysical Research Atmospheres, 118*(4), 1668–1678. https://doi.org/10.1029/2012JD018653

- Liu, G., Janches, D., & Lieberman, R. S. (2018). Intraseasonal variations of nonmigrating tides observed near the mesopause. *Journal of Geophysical Research: Space Physics, 123*, 9921– 9931. https://doi.org/10.1029/2018JA025709

- Liu, H. L., Foster, B. T., Hagan, M. E., McInerney, J. M., Maute, A., Qian, L., Richmond, A. D., Roble, R. G., Solomon, S. C., Garcia, R. R., Kinnison, D., Marsh, D. R., Smith, A. K., Richter, J., Sassi, F., & Oberheide, J. (2010). Thermosphere extension of the Whole Atmosphere Community Climate Model. *Journal of Geophysical Research: Space Physics, 115*(12), 1–21. https://doi.org/10.1029/2010JA015586.

- Liu, H. L., & Hagan, M. E. (1998). Local heating/cooling of the mesosphere due to gravity wave and tidal coupling. *Geophysical Research Letters, 25*(15), 2941–2944. https://doi.org/10.1029/98GL02153.

- Liu, H. L., Li, T., She, C. Y., Oberheide, J., Wu, Q., Hagan, M. E., Xu, J., Roble, R. G., Mlynczak, M. G., & Russell, I. M. (2007). Comparative study of short-term diurnal tidal variability. *Journal of Geophysical Research Atmospheres, 112*(18), 1–16. https://doi.org/10.1029/2007JD008542

- Lu, X., Liu, H. L., Liu, A. Z., Yue, J., McInerney, J. M., & Li, Z. (2012). Momentum budget of the migrating diurnal tide in the Whole Atmosphere Community Climate Model at vernal equinox. *Journal of Geophysical Research Atmospheres, 117*(7), 1–14. https://doi.org/10.1029/2011JD017089

- Lübken, F. J., Austin, J., Langematz, U., & Oberheide, J. (2010). Introduction to special section on climate and weather of the sun earth system. *Journal of Geophysical Research Atmospheres, 115*(13), 1–6. https://doi.org/10.1029/2009JD013784

- Luhr, H., Rother, M., Hausler, K., Alken, P., & Maus S. (2008). The influence of nonmigrating tides on the longitudinal variation of the equatorial electrojet. *J. Geophys. Res., 113*, A08313, doi:10.1029/ 2008JA013064

- Madden, R. A. (2007). Large-scale, free rossby waves in the atmosphere: An update. *Tellus A: Dynamic Meteorology and Oceanography, 59*(5), 571– 590.

- Madden, R. A. & Julian, P. R. (1972). Description of global-scale circulation cells in the tropics with a 40–50-day period. *Journal of the Atmospheric Sciences, 29*, 1109–1123. https://doi.org/10.1175/1520-0469(1972)029<1109:DOGSCC>2.0.CO;2

- Madden, R. A., & Julian, P. R. (1994). Observations of the 40–50-day tropical oscillation- A review. *Monthly Weather Review, 122*, 814–837. https://doi.org/10.1175/1520-0493(1994)122<0814:OOTDTO>2.0.CO;2

- Manson, A. H., Meek, C. E., Fleming, E., Chandra, S., Vincent, R. A., Phillips, A., Avery, S. K., Fraser, G. J., Smith, M. J., Fellous, J. L., & Massebeuf, M. (1991), Comparisons between satellite-derived gradient winds and radar-derived winds from the CIRA-86. *J. Atmos. Sciences, 48*, 3, 1991.

- Manson, A. H., Meek, C. E., Gregory, J. B., & Chakraparty, D. K. (1982). Fluctuations in the tidal (24, 12 h) characteristics and oscillations (8h-5h) in the mesosphere and lower thermosphere, *Plan. Space Sci., 30*, 1283.

- Margulis, M. (1893). Luftbewegungen in einer rotierended spharoidschale (Vol. 102, pp. 11–56). Wiss. Wien: Sber. Akad. (in German)

- Marsh, D. R., Mills, M. J., Kinnison, D. E., Lamarque, J. F., Calvo, N., & Polvani, L. M. (2013). Climate change from 1850 to 2005 simulated in CESM1(WACCM). *Journal of Climate, 26*(19), 7372–7391. https://doi.org/10.1175/JCLI-D-12-00558.1

- Mayr, H. G., Mengel, J. G., Talaat, E. R., Porter, H. S., & Chan, K. L. (2003). Planetary-scale inertio gravity waves in the mesosphere. *Geophysical Research Letters, 30*(23), 23–26. https://doi.org/10.1029/2003GL018376

- Mayr, H. G., & Mengel, J. G. (2005). Interannual variations of the diurnal tide in the mesosphere generated by the quasi-biennial oscillation. *J. Geophys. Res., 110*, D10111, doi:10.1029/2004JD005055

- McLandress, C. (2002). The seasonal variation of the propagating diurnal tide in the mesosphere and lower thermosphere. Part II: The role of tidal heating and zonal mean winds. *Journal of the Atmospheric Sciences, 59*(5), 907–922. https://doi.org/10.1175/1520-0469(2002) 0592.0.CO;2

- Miyahara, S., Miyoshi, Y., & Yamashita, K. (1999). Variations of migrating and non-migrating tides simulated by the Middle Atmosphere Circulation Model at Kyushu University. *Advances in Space Research, 24*(11), 1549–1558. https://doi.org/10.1016/S0273-1177(99)00879-0

- Mukhtarov, P., Pancheva, D., & Andonov, B. (2009). Global structure and seasonal and interannual variability of the migrating diurnal tide seen in the SABER/TIMED temperatures between 20 and 120 km. *Journal of Geophysical Research: Space Physics, 114*(A2).

- Naito, Y., & Hirota, I. (1997). Interannual variability of the northern wi nter stratospheric circulation rel ated to the QBO and the solar cycle. *J. Meteorol. Soc. Jpn., 75*, 925–937.

- Nakamura, T., Fritts, D. C., Isler, J. R., Tsuda, T., Vincent, R. A., & Reid, I. M. (1997). Short-period fluctuations of the diurnal tide observed with low-latitude MF and meteor radars during CADRE: Evidence for gravity wave/tidal interactions. *Journal of Geophysical Research: Atmospheres, 102*(D22), 26225–26238. https://doi.org/10.1029/96jd03145

- National Research Council (2013). Solar and Space Physics: A Science for a Technological Society. *Washington, DC: The National Academies Press*. https://doi.org/10.17226/13060

- Nischal, N., Oberheide, J., Mlynczak, M. G., Hunt, L. A., & Maute, A. (2017). Nonmigrating tidal impact on the CO2 15 μm infrared cooling of the lower thermosphere during solar minimum conditions. *Journal of Geophysical Research: Space Physics, 122*(6), 6761–6775. https://doi.org/10.1002/2017JA024273

- Nischal, N., Oberheide, J., Mlynczak, M. G., Marsh, D. R., & Gan, Q. (2019). Solar cycle variability of nonmigrating tides in the 5.3 and 15 μm infrared cooling of the thermosphere (100–150 km) from SABER. *Journal of Geophysical Research: Space Physics, 124*(3), 2338–2356. https://doi.org/10.1029/2018JA026356

- Norton, W. A., & Thuburn, J. (1999), Sensitivity of mesospheric mean flow, planetary waves, and tides to strength of gravity wave drag, *J. Geophys. Res., 104* (D24), 30897– 30911, https://doi.org/10.1029/1999JD900961

- Oberheide, J. (2007). On large-scale wave coupling across the stratopause *Professorial Dissertation (Habilitationsschrift),* Deutsche Nationalbibliothek, urn:nbn:de:hbz:468-20070724.

- Oberheide, J., & Forbes, J. M. (2008). Tidal propagation of deep tropical cloud signatures into the thermosphere from TIMED observations. *Geophysical Research Letters, 35*(4), 1–5. https://doi.org/10.1029/2007GL032397

- Oberheide, J., Forbes, J. M., Häusler, K., Wu, Q., & Bruinsma, S. L. (2009). Tropospheric tides from 80 to 400 km: Propagation, interannual variability, and solar cycle effects. *Journal of Geophysical Research Atmospheres, 114*(23), 1–18. https://doi.org/10.1029/2009JD012388

- Oberheide, J., Forbes, J. M., Zhang, X., & Bruinsma, S. L. (2011). Climatology of upward propagating diurnal and semidiurnal tides in the thermosphere. *Journal of Geophysical Research: Space Physics, 116*(11). https://doi.org/10.1029/2011JA016784

- Oberheide, J., Hagan, M. E., Roble, R. G., & Offermann, D. (2002). Sources of nonmigrating tides in the tropical middle atmosphere. *Journal of Geophysical Research Atmospheres, 107*(21), 1–14. https://doi.org/10.1029/2002JD002220

- Oberheide, J., Hagan, M. E., & Roble, R. G. (2003). Tidal signatures and aliasing in temperature data from slowly precessing satellites. *Journal of Geophysical Research: Space Physics, 108*(A2), 1–11. https://doi.org/10.1029/2002JA009585

- Oberheide, J., Hagan, M. E., Ward, W. E., Riese, M., & Offermann D. (2000). Modeling the diurnal tide for the CRISTA 1 time period. *J. Geophys. Res., 105*, 24,917-24,929. doi:10.1029/2000JA000047

- Oberheide, J., Shiokawa, K., Gurubaran, S., Ward, W. E., Fujiwara, H., Kosch, M. J., et al. (2015). The geospace response to variable inputs from the lower atmosphere: a review of the progress made by Task Group 4 of CAWSES-II. *Progress in Earth and Planetary Science (Vol. 2).* https://doi.org/10.1186/s40645-014-0031-4

- Ortland, D. A. (2005), A study of the global structure of the migrating diurnal tide using generalized hough modes, *J. Atmos. Sci., 62*, 2684–2702

- Ortland, D. A., & Alexander, M. J. (2006). Gravity wave influence on the global structure of the diurnal tide in the mesosphere and lower thermosphere. *Journal of Geophysical Research: Space Physics, 111*(10). https://doi.org/10.1029/2005JA011467

- Palo, S. E., Roble, R. G., & Hagan, M. E. (1998), TIME-GCM results for the quasi-two-day wave, *Geophys. Res. Lett., 25*, 3783–3786, doi:10.1029/1998GL900032

- Pancheva, D., Merzlyakov, E., Mitchell, N. J., Portnyagin, Y., Manson, A. H., Jacobi, C., et al. (2002). Global-scale tidal variability during the PSMOS campaign of June-August 1999: Interaction with planetary waves. *Journal of Atmospheric and Solar-Terrestrial Physics (Vol. 64).* https://doi.org/10.1016/S1364-6826(02)00199-2

- Pancheva, Dora V., & Mitchell, N. J. (2004). Planetary waves and variability of the semidiurnal tide in the mesosphere and lower thermosphere over Esrange (68°N, 21°E) during winter. *Journal of Geophysical Research: Space Physics, 109*(A8). https://doi.org/10.1029/2004JA010433

- Pancheva, D., Mukhtarov, P., Andonov, B., Mitchell, N. J., & Forbes, J. M. (2009). Planetary waves observed by TIMED/SABER in coupling the stratosphere-mesosphere-lower thermosphere during the winter of 2003/2004: Part 2 – Altitude and latitude planetary wave structure, *J. Atmos. Sol-Terr. Phy., 71*, 75–87, https://doi.org/10.1016/j.jastp.2008.09.027, 2009

- Pedatella, N. M., Forbes, J. M., & Oberheide. J. (2008). Intra-annual variability of the low-latitude ionosphere due to nonmigrating tides. *Geophys. Res. Lett., 35*, L18104, doi:10.1029/2008GL035332

- Pedatella, N. M., Liu, H. L., & Hagan, M. E. (2012). Day-to-day migrating and nonmigrating tidal variability due to the six-day planetary wave. *Journal of Geophysical Research: Space Physics, 117*(6), 1–12. https://doi.org/10.1029/2012JA017581

- Pedatella, N. M., Oberheide, J., Sutton, E. K., Liu, H., Anderson, J. L., & Raeder, K. (2016). Short-term nonmigrating tide variability in the mesosphere, thermosphere, and ionosphere. *Journal of Geophysical Research: Space Physics*, 3621–3633. https://doi.org/10.1002/2016JA022528.Received

- Powell, S. W. (2017). Successive MJO propagation in MERRA-2 reanalysis. *Geophysical Research Letters, 44*(10), 5178–5186. https://doi.org/10.1002/2017GL073399

- Rezac, L., Jian, Y., Yue, J., Russell III, J. M., Kutepov, A., Garcia, R., Walker, K., & P. B. (2015). Validation of the global distribution of CO2 volume mixing ratio I the mesosphere ad lower thermosphere from SABER. *Journal of Geophysical Research: Atmospheres., 120*, 12067–12081. https://doi.org/10.1002/2015JD023955

- Richmond, A. D. (1975). Energy relations of atmospheric tides and their significance to approximate methods of solution for tides with dissipative forces. *Journal of The Atmospheric Sciences, 32*, 980-987. doi:10.1175/1520-0469(1975)032<0980:EROATA>2.0.CO;2

- Richmond, A. D., Matsushita, S., & Tarpley, J. D. (1976). On the production mechanism of electric currents and fields in the ionosphere. *J.Geophys. Res., 81*, 547-555.

- Riggin, D. M., & Lieberman, R. S. (2013). Variability of the diurnal tide in the equatorial MLT. *Journal of Atmospheric and Solar-Terrestrial Physics, 102*, 198–206. https://doi.org/10.1016/j.jastp.2013.05.011

- Riggin, D. M., Meyer, C. K., Fritts, D. C., Jarvis, M. J., Murayama, Y., Singer, W., et al. (2003). MF radar observations of seasonal variability of semidiurnal motions in the mesosphere at high northern and southern latitudes. *Journal of Atmospheric and Solar-Terrestrial Physics, 65*(4), 483–493. https://doi.org/10.1016/S1364-6826(02)00340-1

- Russell III, J. M., Mlynczak, M. G., Gordley, L. L., Tansock, Jr., J. J., & Esplin, R. W. (1999). Overview of the SABER experiment and preliminary calibration results. Optical Spectroscopic Techniques and Instrumentation for Atmospheric and Space Research III, 3756, 277. https://doi.org/10.1117/12.366382

- Salby, M. L. (1982). A ubiquitous wavenumber-5 anomaly in the Southern Hemisphere during FGGE. *Mon. Wea. Rev., 110*,1712-1720.

- Sassi, F., & Liu, H. L. (2014). Westward traveling planetary wave events in the lower thermosphere during solar minimum conditions simulated by SD-WACCM-X. *Journal of Atmospheric and Solar-Terrestrial Physics, 119*, 11–26. https://doi.org/10.1016/j.jastp.2014.06.009

- Sassi, F., McCormack, J. P., & McDonald, S. E. (2019). Whole atmosphere coupling on intraseasonal and interseasonal time scales: A potential source of increased predictive capability. *Radio Science, 54*(11), 913–933. https://doi.org/10.1029/2019RS006847

- She, C. Y., Li, T., Collins, R. L., Yuan, T., Williams, B. P., Kawahara, T. D., et al. (2004). Tidal perturbations and variability in the mesopause region over Fort Collins, CO (41N, 105W): Continuous multi-day temperature and wind lidar observations. *Geophysical Research Letters, 31*(24), 1–5. https://doi.org/10.1029/2004GL021165

- Sun, Y. Y., Liu, H., Miyoshi, Y., Liu, L., & Chang, L. C. (2018). El Niño–Southern Oscillation effect on quasi-biennial oscillations of temperature diurnal tides in the mesosphere and lower thermosphere. *Earth, Planets and Space, 70*(1). https://doi.org/10.1186/s40623-018-0832-6

- Talaat, E. R., & Lieberman, R. (1999). Non-migrating diurnal tides in mesospheric and lower thermospheric winds and temperatures. *J. Atmos. Sci., 56*, 4073.

- Teitelbaum, H., & Vial, F. (1991). On tidal variability induced by nonlinear interaction with planetary waves. *J. Geophys. Res., 96*, 14,169–14,178.

- Tian, B., Ao., C. O., Waliser, D. E., Fetzer, E. J., Mannucci, A. J., & Teixeira, J. (2012). Intraseasonal temperature variability in the upper troposphere and lower stratosphere from the GPS radio occultation measurements. *Journal of Geophysical Research Atmospheres, 117*(15), 1–19. https://doi.org/10.1029/2012JD017715

- Torrence, C., & Compo, G. (1998). A practical guide to wavelet analysis. *Bulletin of the American Meteorological Society, 79*(1), 61-78. Retrieved from https://journals.ametsoc.org/doi/pdf/10.1175/1520-0477%281998%29079%3C0061%3AAPGTWA%3E2.0.CO%3B2

- Trukowski, A., Forbes, J. M., Zhang, X., & Palo. S. E. (2014), New perspectives on thermosphere tides: 1. Lower-thermosphere spectra and seasonal-latitudinal structures, *Earth Planets Space, 66*(136), doi:10.1186/s40623-014-0136-4

- Tsuda, T., & Kato, S. (1989). Diurnal non-migrating tides excited by a differential heating due to land-sea distribution, *J. Meteorol. Soc. Jpn., 67*, 43 – 54.

- Vergados, P., Liu, G., Mannucci, A. J., & Janches, D. (2018). Equatorial intraseasonal temperature oscillations in the lower thermosphere from SABER. *Geophysical Research Letters, 45*(20), 10,893-10,902. https://doi.org/10.1029/2018GL079467

- Vincent, R. A., Tsuda, T., & Kato, S. (1988). A comparative study of mesospheric solar tides observed at Adelaide and Kyoto. *J. Geophys. Res., 93*, 699-708.

- Vitharana, A., Zhu, X., Du, J., Oberheide, J., & Ward, W. E. (2019). Statistical modeling of tidal weather in the mesosphere and lower thermosphere. *Journal of Geophysical Research: Atmospheres, 124*(16), 9011–9027. https://doi.org/10.1029/2019jd030573

- Waliser, D. E., Moncrieff, M. W., Burridge, D., Fink, A. H., Gochis, D., Goswami, B. N., et al. (2012). The "year" of tropical convection (May 2008-April 2010): Climate variability and weather highlights. *Bulletin of the American Meteorological Society, 93*(8), 1189–1218. https://doi.org/10.1175/2011BAMS3095.1

- Walterscheid, R. L. (1980). Inertio-gravity wave induced acceleration of mean flow having an imposed periodic component: implications for tidal observations in the meteor region. *J. geophys. Res. 86*, 9698.

- Ward, W. E., Oberheide, J., Riese, M., Preusse, P., & Offermann, D. (1999). Tidal signatures in temperature data from the CRISTA I mission. *J. Geophys. Res., 104*, 16,391–16,403.

- Warner, K., & Oberheide, J. (2014). Nonmigrating tidal heating and MLT tidal wind variability due to the El Niño–Southern Oscillation. *Journal of Geophysical Research, 119*(3), 1249–1265. https://doi.org/10.1002/2013JD020407

- Wheeler, M. C., & Hendon, H. H. (2004). An all-season real-time multivariate MJO index: Development of an index for monitoring and prediction. *Monthly Weather Review, 132*(8), 1917–1932. https://doi.org/10.1175/1520-0493(2004)132<1917:AARMMI>2.0.CO;2

- Wheeler, M. C., & Kiladis, G. N. (1999). Convectively coupled equatorial waves: analysis of clouds and temperature in the wavenumber-frequency domain. *Journal of the Atmospheric Sciences, 56*(3), 374–399. https://doi.org/10.1175/1520-0469(1999)056<0374:CCEWAO>2.0.CO;2

- Williams, C. R., & Avery, S. K. (1996). Non-migrating diurnal tides forced by deep convective clouds. *J. Geophys. Res., 101*, 4079 – 4091.

- Wu, D. L., McLandress, C., Read, W. G., Waters, J. W., & Froidevaux, L. (1998). Equatorial diurnal variations observed in UARS Microwave Limb Sounder temperature during 1991–1994 and simulated by the Canadian Middle Atmosphere Model. *J. Geophys. Res., 103*, 8909–8917.

- Wu, Q., Ortland, D. A., Killeen, T. L., Roble, R. G., Hagan, M. E., Liu, H. L., et al. (2008a). Global distribution and interannual variations of mesospheric and lower thermospheric neutral wind diurnal tide: 1. Migrating tide. *Journal of Geophysical Research: Space Physics, 113*, 1–18. https://doi.org/10.1029/2007JA012542

- Wu, Q., Ortland, D. A., Killeen, T. L., Roble, R. G., Hagan, M. E., Liu, H. L., et al. (2008b). Global distribution and interannual variations of mesospheric and lower thermospheric neutral wind diurnal tide: 2. Nonmigrating tide. *Journal of Geophysical Research: Space Physics, 113*, 1–26. https://doi.org/10.1029/2007JA012543

- Xu, Z., Yin, B. S., Hou, Y. J., & Xu, Y. S. (2013). Variability of internal tides and near-inertial waves on the continental slope of the northwestern South China Sea. *J. Geophys. Res. Oceans, 118*, 197– 211, doi:10.1029/2012JC008212

- Yamazaki, Y., & Matthias, V. (2019). Large-amplitude Quasi-10-day waves in the middle atmosphere during final warmings. *Journal of Geophysical Research: Atmospheres*, 1–19. https://doi.org/10.1029/2019jd030634

- Yang, C., Smith, A. K., Li, T., & Dou, X. (2018). The Effect of the Madden-Julian Oscillation on the mesospheric migrating diurnal tide: A study using SD-WACCM. *Geophysical Research Letters, 45*(10), 5105–5114. https://doi.org/10.1029/2018GL077956

- Zhang, C. (2005). Madden-Julian Oscillation. *Reviews of Geophysics*. 1–36. https://doi.org/10.1029/2004RG000158

- Zhang, X., Forbes, J. M., & Hagan, M. E. (2012). Seasonal-latitudinal variation of the eastward-propagating diurnal tide with zonal wavenumber 3 in the MLT: Influences of heating and background wind distribution. *Journal of Atmospheric and Solar-Terrestrial Physics*, 78–79, 37–43. https://doi.org/10.1016/j.jastp.2011.03.005